A QM/QM Hybrid Method for MP2/Plane-Wave-DFT Studies of Extended Systems

Dissertation

zur Erlangung des akademischen Grades

doctor rerum naturalium
(Dr. rer. nat.)

im Fach Chemie

eingereicht an der

Mathematisch-Naturwissenschaftlichen Fakultät I
der Humboldt-Universität zu Berlin

von

Herrn Dipl.-Chem. Christian Tuma
geboren am 04.11.1974 in Berlin

Präsident der Humboldt-Universität zu Berlin
Prof. Dr. Christoph Markschies

Dekan der Mathematisch-Naturwissenschaftlichen Fakultät I
Prof. Dr. Christian Limberg

Gutachter:
1. Prof. Dr. Joachim Sauer
2. Prof. Dr. Matthias Scheffler
3. Prof. Piero Ugliengo

Tag der mündlichen Prüfung: 14. Dezember 2006

Abstract

Due to their comparatively high efficiency standard methods in density functional theory (DFT) belong to the most popular computational approaches in quantum mechanics (QM). In certain applications, however, widely used density functionals do not yield reliable results. This applies, for example, to the calculation of activation barriers or dispersive interactions. Problems of this type can be overcome in principle by using electron correlation methods, but in many cases too high computational costs rule out their application. The simplest QM method for electron correlation, second-order Møller–Plesset perturbation theory (MP2), describes dispersion well.

In this work a hybrid method solely based upon QM approaches is presented, combining advantages of both DFT and electron correlation methods. DFT calculations are performed for the full system and an embedded cluster model representing the active site. To this end an atomic pseudopotential plane wave approach, computationally well suited for periodic systems, is chosen. DFT implementations of this type are rarely used in computational chemistry, and for this reason test calculations are performed to ensure sufficient accuracy in subsequent applications. The cluster model is also calculated with MP2. Thus corrections for DFT energy and energy gradient results are obtained and applied to the full system. Stationary points on the potential energy surface defined this way are localised employing standard structure optimisation techniques.

The reliability of the results obtained with this hybrid method is further improved by extrapolation to the limiting case of a complete basis set and an infinitely large cluster model. Employing plane waves in the DFT part the limit of a virtually complete basis set can be accomplished easily in a systematic manner. For MP2 commonly used extrapolation schemes are applied, requiring additional effort to account for the basis set superposition error. MP2 corrections to DFT reaction energies, which, in first approximation, can be attributed to the neglected long-range part of dispersion, are determined for a systematic series of cluster models of increasing size. These corrections are used for fitting a parametrised damped C_6 pair potential. For all models, including the full system under

periodic boundary conditions, the fitted potential is employed to obtain corrections to DFT reaction energies, that is, to estimate MP2 reaction energies. Small model systems are used in coupled-cluster reaction energy calculations to verify the reliability of MP2.

Application of the hybrid method is demonstrated in the field of heterogeneous catalysis. Case studies are the investigation of proton jump reactions in the zeolite chabazite and protonation reactions of isobutene in the zeolite ferrierite. The MP2/DFT results obtained confirm that activation barriers are clearly underestimated with purely gradient corrected density functionals. Rate constants are corrected by up to two orders of magnitude. It is shown further that for adsorption and chemisorption of hydrocarbons in zeolites reaction energies can hardly be predicted with DFT. MP2 corrections obtained are in a range from –29 to –70 kJ/mol and, even more important, are not the same for different products. Of all structures investigated the surface alkoxides benefit most from an improved consideration of dispersion. The *tert*-butyl carbenium ion, hydrogen-bonded to the zeolite framework, is much less stable than predicted with DFT. The calculated MP2 heat of adsorption of isobutene in ferrierite (–74±10 kJ/mol) corresponds to experimental results for similar systems and underlines the reliability of the hybrid MP2/DFT approach presented in this work.

Keywords:
density functional theory, hybrid methods, dispersion interaction, zeolite catalysts

Zusammenfassung

Standardmethoden der Dichtefunktionaltheorie (DFT) gehören aufgrund ihrer vergleichsweise hohen Effizienz zu den beliebtesten quantenmechanischen (QM) Rechenverfahren. Es gibt jedoch Anwendungsfälle, in denen gegenwärtig häufig eingesetzte Funktionale keine verlässlichen Ergebnisse liefern. Dazu gehören beispielsweise Berechnungen von Dispersionswechselwirkungen und oft auch von Aktivierungsbarrieren. Probleme dieser Art lassen sich durch den Einsatz von Elektronenkorrelationsmethoden prinzipiell lösen, was in der Praxis jedoch häufig an einem zu hohen Rechenaufwand scheitert. Der einfachste Ansatz zur expliziten Berücksichtigung der Elektronenkorrelation, und damit auch der Dispersionswechselwirkung, ist Møller–Plesset Störungstheorie zweiter Ordnung (MP2).

In der vorliegenden Arbeit wird eine auf ausschließlich quantenmechanischen Verfahren basierende Hybridmethode vorgestellt, die die Vorzüge von DFT und Elektronenkorrelationsmethoden miteinander kombiniert. Dabei erfolgen zunächst DFT-Berechnungen sowohl für das Gesamtsystem als auch für ein darin eingebettetes Clustermodell, welches das aktive Zentrum darstellt. Hier kommt eine Implementierung mit atomaren Pseudopotentialen und Basisfunktionen aus ebenen Wellen zum Einsatz, was insbesondere für periodische Systeme von rechtentechnisch großem Vorteil ist. Da DFT-Programme dieser Art in der Quantenchemie wenig populär sind, wurden Testrechnungen durchgeführt, um die nötige Genauigkeit in späteren Anwendungen zu garantieren. Das Clustermodell wird außerdem mit MP2 beschrieben, wodurch Korrekturen gegenüber den DFT-Ergebnissen für die Energie und den Energiegradienten ableitbar sind, die auf das Gesamtsystem angewendet werden. Zur Lokalisierung stationärer Punkte auf der so definierten Potentialfläche kommen Standardverfahren der Strukturoptimierung zum Einsatz.

Die Zuverlässigkeit der mit dieser Hybridmethode erzielten Ergebnisse wird zusätzlich durch Extrapolation auf den Grenzfall eines vollständigen Basissatzes und eines unendlich großen Clustermodells erhöht. Im DFT-Teil kann durch die Verwendung ebener Wellen das Limit einer praktisch vollständigen Basis systematisch und schnell erreicht werden.

Für MP2 werden bekannte Extrapolationsverfahren eingesetzt, die jedoch zusätzlichen Aufwand durch Korrekturen für den hier auftretenden Basissatzüberlagerungsfehler erfordern. MP2-Korrekturen für DFT-Reaktionsenergien, die in erster Näherung auf den mit DFT vernachlässigten, langreichweitigen Dispersionsanteil zurückzuführen sind, werden für eine systematische Reihe von unterschiedlich großen Clustermodellen ermittelt. Daran wird ein parametrisiertes, gedämpftes C_6-Paarpotential angepasst, das schließlich auch für das Gesamtsystem (periodische Randbedingungen) die Abschätzung einer MP2-Korrektur der DFT-Reaktionsenergie, und damit eines reinen MP2-Ergebnisses, erlaubt. An kleinen Modellen wird ein hochgenaues coupled-cluster Rechenverfahren eingesetzt, um gegebenenfalls Korrekturen der Ergebnisse über MP2-Qualität hinaus zu erzielen.

Erste Anwendungen dieser Hybridmethode erfolgen auf dem Gebiet der heterogenen Katalyse. Dazu werden exemplarisch Protonensprungreaktionen im Zeolith Chabasit und Protonierungsreaktionen von Isobuten im Zeolith Ferrierit untersucht. Die gewonnenen MP2/DFT-Ergebnisse bestätigen, dass Aktivierungsbarrieren mit einfachen Dichtefunktionalen deutlich unterschätzt werden. Geschwindigkeitskonstanten sind nach Korrektur um ein bis zwei Größenordnungen kleiner. Weiterhin kann gezeigt werden, dass Reaktionsenergien für die Adsorption und Chemisorption von Kohlenwasserstoffen in Zeolithen mit DFT qualitativ schlecht vorausgesagt werden. MP2-Korrekturen sind für die verschiedenen Reaktionsprodukte unterschiedlich groß und liegen in einem Bereich von −29 bis −70 kJ/mol. Oberflächenalkoxide profitieren energetisch am meisten durch die verbesserte Berücksichtigung der Dispersionswechselwirkung, während das *tert*-Butylcarbeniumion, das über eine Wasserstoffbrücke mit dem Zeolithgerüst verbunden ist, eine deutlich geringere relative Stabilität aufweist, als nach den DFT-Ergebnissen vermutet werden kann. Die berechnete MP2-Adsorptionswärme des Isobutens im Zeolith Ferrierit (−74±10 kJ/mol) entspricht experimentellen Ergebnissen an ähnlichen Systemen und unterstreicht die Zuverlässigkeit des in dieser Arbeit vorgestellten MP2/DFT-Hybridansatzes.

Schlagwörter:
Dichtefunktionaltheorie, Hybridmethoden, Dispersionswechselwirkung, Zeolithkatalysatoren

Meinen Eltern

Contents

Chapter 1

INTRODUCTION

1.1 MOTIVATION

In computer simulations of materials and molecular systems the use of Kohn–Sham density functional theory (DFT) [1–7] has met with great success. Today DFT is the computationally most efficient quantum mechanical (QM) approach applicable to a wide range of chemical systems. Advanced algorithms and various approximation schemes [8–10] allow for low-order scaling DFT implementations suitable to study extended molecular and periodic systems relevant in, *e. g.*, different fields of catalysis research. This applies to the pseudopotential plane wave DFT approach used throughout the present work. Special care, however, must be taken when DFT is employed for certain types of problems. These include weak interactions and activation barriers (see, *e. g.*, refs. [7, 11–22] and literature cited therein) which will be addressed in the context of this work.

The exact density functional for exchange and correlation is unknown. A large number of different proposals exists, and in light of the problems unsolved so far much effort is spent to find approximations to the true functional better than those available today [23]. One strategy for improvement is to satisfy purely physical conditions valid for the true functional and to reduce the number of parameters as much as possible [24]. Based on the local density approximation (LDA) such non-empirical improvements incorporate the first derivative of the electron density (generalised gradient approximation, GGA) or higher derivatives (meta-GGA), or the admixture of exact exchange (hybrid functionals). A different (*i. e.*,

empirical) way is to start from a parametrised expression for the true functional and to fit its parameters to reproduce reference data of selected training systems (see, *e. g.*, ref. [25]).

Experience shows that hybrid functionals usually yield reliable results in many chemistry related applications of DFT. Pure GGA type functionals, however, are known to show typical deficiencies like, *e. g.*, underestimation of reaction barriers. Unfortunately, the calculation of exact exchange (Fock exchange) is computationally very expensive with a plane wave basis set. For this reason plane wave DFT applications usually employ a GGA type density functional and, hence, potentially face the difficulties mentioned above.

Another problem present with any of the available standard density functionals is the complete neglect of the long-range part of dispersion interaction. This is an active field of research, and different types of solution have been put forward. Certain types of non-empirical density functionals yield some dispersion at least for short interatomic distances [21], and attempts to parametrise the different exchange and correlation terms in hybrid meta-GGA functionals show further improvements in the range of overlapping densities [26]. For a reliable description of dispersion interaction one can split the exchange–correlation functional and treat the long-range part in a more advanced fashion. Long-range exchange is either calculated exactly or approximated by a GGA that yields qualitatively correct exchange. The long-range part for correlation, however, is much more difficult to obtain. Functionals depending on the densities of two sub-systems have been suggested [27, 28] as well as treatments based on second-order perturbation theory [29]. Random-phase approximation and related time-dependent DFT methods account for the correlation energy by the adiabatic connection fluctuation–dissipation theorem but do not seem to be suitable for large systems due to the steep scaling of the operation count with increasing size of the system [30–32]. A fully empirical and computationally cheap solution is adding a damped dispersion term to standard density functionals calculated from parametrised atom–atom C_6 contributions [33–37]. Schemes for the direct calculation of C_6 coefficients using time-dependent DFT [38] or conventional DFT [39, 40] have also been proposed.

Dispersion is a dynamic effect caused by the correlated movement of electrons. Wavefunction theory (WFT) approaches beyond the Hartree–

Fock (HF) method [41–45], by definition, do account for electron correlation. The single-particle single-determinant HF description of many-particle interactions can be extended by perturbation theory or by coupled-cluster approaches to cover dynamical correlation while, in parallel, multi-reference descriptions can be introduced for non-dynamical correlation (see, *e. g.*, refs. [46–50] and literature cited therein). These so-called "*post* HF" approaches represent methodological hierarchies of increasing accuracy for the explicit treatment of electron correlation. Unfortunately, the computational effort associated with these methods increases rapidly with growing size of the system. In practical calculations highest accuracy can only be achieved for systems containing a few atoms. The simplest method for the explicit treatment of electron correlation is second-order Møller–Plesset perturbation theory (MP2) [51, 52] which will be used extensively in this work. The application of DFT is computationally much cheaper, but—as opposed to *post* HF schemes—systematic improvements of the DFT Hamiltonian, in particular of the exchange–correlation functional, do not exist.

The motivation behind the present work is the idea of a hybrid approach combining the computational efficiency of DFT and the reliable description of electron correlation by *post* HF methods. A hybrid QM/QM embedding implementation is presented for *ab initio* studies of extended systems including periodic boundary conditions. Plane wave DFT is applied to the full (periodic) system and to embedded cluster models representing the reaction site while the latter are also calculated using MP2. This way the problems encountered with standard DFT (see above) can be effectively eliminated in many cases, and structures and reaction energies for extended systems of currently unsurpassed quality are obtained.

The present work is organised as follows. This chapter introduces the QM-Pot mechanical embedding scheme and details of the hybrid MP2/DFT approach. Chapter 2 addresses computational issues related to pseudopotential plane wave DFT as well as Gaussian basis set MP2 calculations. Its main purpose is to show that the pseudopotential plane wave DFT approach developed in the physics community can also be successfully applied in chemistry. This, however, requires a careful choice of the computational parameters which, in turn, is not necessarily straightforward and might need extensive preparatory tests. Selected

examples from current topics in the broad field of zeolite catalysis are taken to demonstrate the functionality and the use of the hybrid MP2/DFT scheme. Water adsorption and proton jump reactions in Brønsted acid chabazite are studied in Chapter 3. A more complex and challenging case is the investigation of adsorption and chemisorption reactions of isobutene in Brønsted acid ferrierite carried out in Chapter 4.

1.2 THE QM-POT EMBEDDING SCHEME

Systems of interest in, *e. g.*, solid-state physics or biochemistry are usually too large for a full QM treatment. For this reason embedding methods have been developed. They have a long tradition in computational chemistry, and it is beyond the scope of the present work to give a full account on their history and recent developments. Instead, the reader is referred to published work [7, 53–64].

Common to all embedding schemes is the partitioning of the entire system under study, that is, the definition of a region 'I' containing the active site which is calculated at high level (QM).[1] The remaining part of the system, 'O', is described at low level. When the interaction between both parts is considered, a simple equation can be written describing the energy of the complete system (see left panel in Fig. 1.1),

$$E(S) = E(I)_{\text{high}} + E(O)_{\text{low}} + E(I \leftrightarrow O) \quad . \tag{1.1}$$

A consistent definition of the interaction term,

$$E(I \leftrightarrow O) = E(S)_{\text{low}} - E(I)_{\text{low}} - E(O)_{\text{low}} \quad , \tag{1.2}$$

turns the additive scheme in eqn. (1.1) into a subtractive scheme,

$$E(S) = E(I)_{\text{high}} + E(S)_{\text{low}} - E(I)_{\text{low}} \quad . \tag{1.3}$$

The latter can be the more convenient case because the calculation of one of the artificially created subsystems ('O') is avoided here. Regarding the interaction between the inner and the outer part, the term *mechanical embedding* is used when force fields or, more general, potential functions

[1] Extension to treat multi-centred systems is feasible [65].

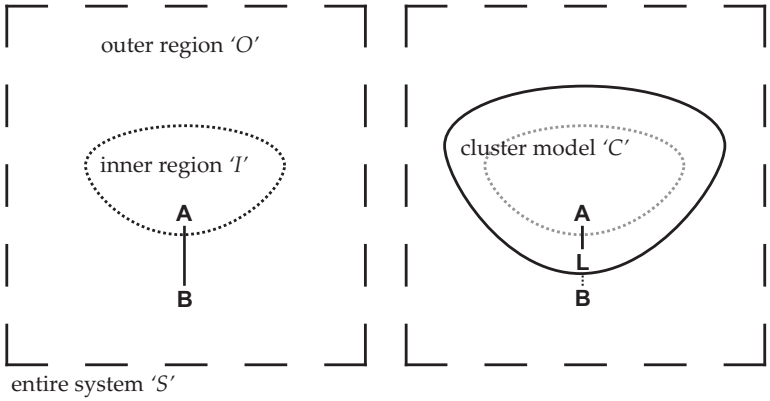

Figure 1.1: *Split of the entire system 'S' (e.g., the unit cell of a periodic structure) and construction of a cluster model 'C' to saturate dangling bonds of the inner part 'I'*

are employed as the low-level method in eqn. (1.2). In *electronic embedding* schemes the Hamiltonian for the QM treatment of the inner region is augmented by terms accounting for the influence of the outer region (see, in addition, refs. [66–71] for examples).

The inner part, however, needs further consideration. Since only in certain cases the high-level region can be defined without breaking chemical bonds between atoms A and B of the inner and outer part, respectively, the problem of terminating the inner part emerges inevitably. A straightforward way is to add link atoms (usually hydrogen) to saturate dangling bonds [72–78]. Since hydrogen atoms do not necessarily show the same properties as the atoms they replace, one can also define a boundary region containing specially parametrised connection atoms [79] or use pseudopotentials [80–82] to mimic the influence of atoms in the outer region. A further approach is to constrain orbitals localised in the terminating region [83–85].

In the present work the link atom method is employed. It is the easiest way to deal with the termination problem, but additional and unphysical degrees of freedom are introduced requiring special care (see below). After saturation of all inner region dangling bonds by hydrogen atoms a cluster model 'C' is obtained representing the system's active site (see

right panel in Fig. 1.1). Now the energy of the embedded system also depends on the link atoms 'L'. Equation (1.3) can be rewritten:

$$E(S,L) = E(C)_{\text{high}} + E(S)_{\text{low}} - E(C)_{\text{low}} \quad . \tag{1.4}$$

The difference between the energy expressions defined in eqns. (1.3) and (1.4),

$$E(S,L) - E(S) = E(C)_{\text{high}} - E(I)_{\text{high}} - [E(C)_{\text{low}} - E(I)_{\text{low}}] \quad , \tag{1.5}$$

vanishes when both the low- and high-level methods contribute the same energy difference upon addition of link atoms to the inner part.

The first derivative of the energy with respect to nuclear coordinates is a key quantity in structure optimisations. Using Cartesian coordinates $S_{i,\alpha}$ for atom i of the entire system and $L_{j,\beta}$ for link atom j present in the cluster model ($\alpha, \beta \in \{x, y, z\}$), the total differential of $E(S,L)$,

$$\mathrm{d}E(S,L) = \sum_{i,\alpha}^{S} \frac{\partial E(S,L)}{\partial S_{i,\alpha}} \mathrm{d}S_{i,\alpha} + \sum_{j,\beta}^{L} \frac{\partial E(S,L)}{\partial L_{j,\beta}} \mathrm{d}L_{j,\beta} \quad , \tag{1.6}$$

expresses under consideration of constrained link atom positions,

$$L_{j,\beta} = f(S) \quad , \tag{1.7}$$

as a function of only the system's atoms coordinates:

$$\mathrm{d}E(S) = \sum_{i,\alpha}^{S} \left(\frac{\partial E(S,L)}{\partial S_{i,\alpha}} + \sum_{j,\beta}^{L} \frac{\partial E(S,L)}{\partial L_{j,\beta}} \frac{\partial L_{j,\beta}}{\partial S_{i,\alpha}} \right) \mathrm{d}S_{i,\alpha} \tag{1.8}$$

In the QM-Pot approach [61, 75, 86] a link atom L_c is always positioned along a cut bond c between atoms A_c and B_c of the inner and outer part, respectively. In addition, the distance between A_c and L_c is kept constant at its initial value.

$$\begin{aligned} L_c &= A_c + g_c(B_c - A_c) \\ g_c &= \frac{|L_{c_0} - A_{c_0}|}{|B_c - A_c|} \end{aligned} \tag{1.9}$$

Consequently, when atoms A_c or B_c change their position the corresponding link atom is moved following these constraints. This is a key feature of

the QM-Pot strategy distinguishing it from other mechanical embedding approaches like, *e. g.*, the ONIOM approach by Morokuma *et al.* [87] where g_c is kept fixed. From the conditions in eqn. (1.9) follows that the right hand side of the parenthesised term in eqn. (1.8) vanishes when atoms S_i and L_j belong to different broken bonds, or, when S_i is not involved in any cut bond at all. In these cases the partial first derivative of the QM-Pot energy with respect to the position of a cluster model atom I_i present in the inner part ($I_i \notin \{A_c\}$) can be written according to eqn. (1.4),

$$\frac{\partial E(S,L)}{\partial I_{i,\alpha}} = \frac{\partial E(C)_{\text{high}}}{\partial I_{i,\alpha}} + \frac{\partial E(S)_{\text{low}}}{\partial I_{i,\alpha}} - \frac{\partial E(C)_{\text{low}}}{\partial I_{i,\alpha}} \quad , \tag{1.10}$$

or, for an atom O_i in the outer region (*i. e.*, not present in the cluster model C, and $O_i \notin \{B_c\}$),

$$\frac{\partial E(S,L)}{\partial O_{i,\alpha}} = \frac{\partial E(S)_{\text{low}}}{\partial O_{i,\alpha}} \quad . \tag{1.11}$$

Otherwise ($S_i \in \{A_c, B_c\}$), partial first derivatives of eqn. (1.9) come into play.

$$\frac{\partial L_{c,\beta}}{\partial A_{c,\alpha}} = (1-g_c)\delta_{\alpha\beta} + g_c \frac{(B_{c,\alpha} - A_{c,\alpha})(B_{c,\beta} - A_{c,\beta})}{|B_c - A_c|^2} \tag{1.12}$$

$$\frac{\partial L_{c,\beta}}{\partial B_{c,\alpha}} = g_c\delta_{\alpha\beta} - g_c \frac{(B_{c,\alpha} - A_{c,\alpha})(B_{c,\beta} - A_{c,\beta})}{|B_c - A_c|^2} \tag{1.13}$$

Now the remaining partial first derivatives of the QM-Pot energy can be calculated,

$$\frac{\partial E(S,L)}{\partial A_{c,\alpha}} = \frac{\partial E(C)_{\text{high}}}{\partial A_{c,\alpha}} + \frac{\partial E(S)_{\text{low}}}{\partial A_{c,\alpha}} - \frac{\partial E(C)_{\text{low}}}{\partial A_{c,\alpha}} + \sum_{\beta}^{3} \left[\left(\frac{\partial E(C)_{\text{high}}}{\partial L_{c,\beta}} - \frac{\partial E(C)_{\text{low}}}{\partial L_{c,\beta}} \right) \left((1-g_c)\delta_{\alpha\beta} + g_c \frac{(B_{c,\alpha} - A_{c,\alpha})(B_{c,\beta} - A_{c,\beta})}{|B_c - A_c|^2} \right) \right] \tag{1.14}$$

and

$$\frac{\partial E(S,L)}{\partial B_{c,\alpha}} = \frac{\partial E(S)_{\text{low}}}{\partial B_{c,\alpha}} + \sum_{\beta}^{3} \left[\left(\frac{\partial E(C)_{\text{high}}}{\partial L_{c,\beta}} - \frac{\partial E(C)_{\text{low}}}{\partial L_{c,\beta}} \right) \left(g_c \delta_{\alpha\beta} - g_c \frac{(B_{c,\alpha} - A_{c,\alpha})(B_{c,\beta} - A_{c,\beta})}{|B_c - A_c|^2} \right) \right] \quad . \quad (1.15)$$

In a similar way expressions for partial second derivatives of the QM-Pot energy are obtained. Given that both the applied high- and low-level methods on their own yield potential energy surfaces in accord with the fundamental principles of momentum and angular momentum conservation, the QM-Pot energy surface defined by eqn. (1.4)—subject to constraints defined in eqn. (1.9)—is invariant to translations and rotations of the system's coordinates [88, 89].

In the present work the QMPOT code [86] is used for all embedding calculations. QMPOT comprises different optimisation algorithms as well as interface functions to several computational chemistry program packages. The latter are operated by QMPOT *via* its interface functions for energy and energy derivative calculations according to the embedding scheme described in this section. With an option for periodic boundary conditions, QMPOT allows for any hybrid QM/MM or QM/QM embedding combination. Details of the QM/QM embedding approach applied in the present work are given in the next section.

1.3 Issues of the Hybrid MP2/DFT Approach

As mentioned before, in this work pseudopotential plane wave DFT constitutes the low-level method. Compared to molecular mechanics, which is traditionally employed at the low level, DFT is more expensive and cannot describe dispersion properly. However, some important advantages arise. Empiricism is largely avoided, and bond breaking as well as bond making processes can be simulated. Mutual polarisation and charge transfer between the inner part (active site) and the environment is already accounted for when the full system is calculated with DFT.

Rather technical advantages of plane waves are the absence of the basis set superposition error (BSSE) [90] and the option to increase the

basis set quality in a systematic and fully balanced way. More details follow in the next chapter.

Computational difficulties, however, arise in the MP2 high-level treatment of the active site. Here Gaussian basis sets are used, and the counterpoise procedure [91, 92] needs to be applied to correct MP2 interaction energies for the BSSE. The frozen core and resolution of the identity approximations are essential to reduce the computational costs of large cluster model MP2 calculations (see next chapter).

Optimised link atom bond distances for the termination of the cluster models are shown in Tab. B.1 (Appendix, page 135).

Chapter 2

VALIDATION OF COMPUTATIONAL PARAMETERS

2.1 PLANE WAVE DFT CALCULATIONS

Plane wave basis sets, on the one hand, are commonly used in periodic boundary DFT studies of condensed systems (*e. g.*, solids, surfaces, or liquids). In quantum chemical calculations of molecular systems, on the other hand, orbitals are usually expanded into a much smaller set of atom-centred Gaussian basis functions. This rather traditional separation is due to individual benefits and drawbacks connected to the use of these basis set types (a more detailed description is given in the next subsection). An interesting point, however, is under which conditions both approaches yield the same results. Since in the present work local basis sets are not employed for systems under periodic boundary conditions, the question whether Gaussian basis set results obtained for finite systems can be reproduced using plane waves is investigated. Although this can be expected *a priori* it is not trivial to show since plane wave DFT calculations contain a number of computational parameters. They need to be carefully adjusted to avoid arbitrary results. The most apparent objective is to gain convergence of calculated quantities with respect to the size of the plane wave basis. Among the various approximations inherent to a plane wave DFT calculation at least the error arising from an incomplete basis set can be eliminated this way. In situations where comparison to reference data cannot be made this is an important means to gain confidence into calculated numbers. Nevertheless, this point is neglected in many plane wave DFT studies on molecular systems. Only in a few contributions the effort

is taken to investigate the dependency of, *e.g.*, energies and structural parameters with respect to the plane wave basis set size [93–97]. Last but not least, when comparisons to Gaussian basis function results are made these basis sets must also be sufficiently large. Otherwise reasons for discrepancies between plane wave and Gaussian basis set results can be assigned to either type of basis set. Systematic investigations of this kind are rare in the literature, and they differ in many aspects. At best a qualitative summary can be given here, for details the reader is referred to the following studies. For example, Hutter *et al.* [98] confirm satisfying accuracy for plane wave basis set DFT binding energies and structures of small water clusters for different density functionals including latest implementations for the calculation of exact exchange. The plane wave basis set, however, was not sufficiently large in this study. Andrews *et al.* [94] show that with increasing size of the plane wave basis set structures of small molecules converge to Gaussian basis set reference values. Binding energies and structures of DNA base pairs are compared in the work by Fellers *et al.* [99]. Results are not fully converged with respect to the size of either type of basis set, leaving some uncertainty in the degree of quantitative correspondence. Structures of DNA base molecules are investigated in more detail by Pulay *et al.* [100]. While reference values for bond lengths and bond angles are reproduced, torsional angles are not predicted correctly using plane waves. In the comprehensive studies by Janfelt and Jensen, atomisation energies [101] as well as bond lengths [102] are statistically analysed for a set of more than 90 molecules composed of first- and second-row elements. Accurate reference data are obtained by applying hierarchies of polarisation-consistent Gaussian basis sets and subsequent extrapolation to the complete basis set limit. Significant errors in the atomisation energies for first-row molecules are observed, deviations decrease due to partial error cancellation when diatomics X_2 instead of atoms X are considered as decomposition products. Errors of only a few kJ/mol are observed for second-row molecules with both approaches. Bond distances are reproduced with average errors of 0.6 pm for first-row and of 0.3 pm for second-row molecules. Addressing the same subject Kresse *et al.* [103] use a smaller test set containing 55 molecules. They find excellent agreement to reference data even for molecules composed of first-row elements when a more advanced plane wave scheme is employed.

In the following sections it is shown how the result of a plane wave DFT calculation can be influenced by different computational parameters. Concerning their choice conclusions are drawn from comparison to corresponding DFT Gaussian basis set reference data or simply from convergence studies. For this purpose small test cases representing the systems studied in this work are chosen. All plane wave DFT calculations in this work are performed using the CPMD code [104–108].

2.1.1 Plane Wave Basis Sets

A plane wave basis set is specified by several parameters. In general, only those plane waves

$$\phi_G^{\mathrm{PW}}(r) = \frac{1}{\sqrt{\Omega}} \exp(iGr) \qquad (\Omega \text{ – simulation cell volume}) \tag{2.1}$$

with wave vectors G of the correct periodicity are considered, that is, G being an integer vector in the primitive reciprocal lattice. This infinitely large but countable set of basis functions is truncated by specifying an upper limit (cut-off) for the plane wave kinetic energy, E_{cut},

$$\left\langle \phi_G^{\mathrm{PW}} \left| -\frac{1}{2}\nabla^2 \right| \phi_G^{\mathrm{PW}} \right\rangle = \frac{1}{2}G^2 \leq E_{\mathrm{cut}} \quad . \tag{2.2}$$

The number of plane waves in the basis set, N^{PW}, depends on the simulation cell volume and on the kinetic energy cut-off,

$$N^{\mathrm{PW}} \approx \frac{1}{2\pi^2}\Omega E_{\mathrm{cut}}^{3/2} \quad . \tag{2.3}$$

Electronic wavefunctions show rapid oscillations in regions close to atomic nuclei. A large number of plane waves is required to model this behaviour, rendering corresponding calculations prohibitively expensive. Several approaches exist to avoid this problem. Within all-electron methods the plane wave basis is augmented by different sets of analytic and computationally more efficient expressions to describe the nearby region around each nucleus using linear transformations (see, *e. g.*, refs. [109–112] and references therein). Truly mixed basis sets can be employed to expand

core orbitals into a set of, *e. g.*, Gaussian functions [113]. A widely used approach is based on effective core potentials (see, *e. g.*, refs. [109, 114, 115] and literature referred to) reducing computational costs for two reasons. First, pseudopotentials replace electrons in core orbitals avoiding the very expensive expansion of these orbitals into plane waves, leaving less and relatively smooth orbitals to calculate with a plane wave basis set of manageable size. Second, the screening of the nuclei's electron–ion potential by electrons in core orbitals can be modified such that valence orbitals get smoothed in the core region. Depending on the details of the applied pseudopotential scheme and on the position of affected chemical elements in the periodic table this further lowers the required size of the plane wave basis set. The pseudopotential approach is used in all plane wave DFT calculations in the present work; details are given in Section 2.1.2.

Due to their free-electron character plane waves appear as a natural basis set in calculations on periodic systems. They are equally distributed in space and fully delocalised, giving rise to two important consequences which are the absence of the basis set superposition error and the representation of nuclear gradients by Hellmann–Feynman forces only. When real space grids are associated with a plane wave basis, fast Fourier techniques can be used for an efficient calculation of, *e. g.*, Coulomb and exchange–correlation energies and potentials. Use of this idea is made in DFT implementations where Gaussian basis sets for the orbital expansion are augmented by plane waves to represent the electron density [116–120]. However, there are also drawbacks connected to plane wave basis sets. Even though they are not used to describe atomic core regions, still very large numbers of plane waves need to be included in such basis sets[1] necessitating substantial amounts of main memory. Nevertheless, given the availability of required computational resources the quality of a plane wave basis set can always be systematically improved by increasing the kinetic energy cut-off value. One of the most serious disadvantages is that much of the computational efficiency is lost when exact exchange is computed in a plane wave basis [121, 122]. Therefore only few studies of this type employing hybrid density functionals have been published so far [98, 103, 123].

[1] several orders of magnitude more compared to local functions

Note 1 — The systems investigated in the present work are electronic insulators with unit cells sufficiently large to approximate the integration over the Brillouin zone by using only its central point, the Γ-point. Additional *k*-points are not used and, therefore, are not considered in the equations and discussions on plane wave basis sets.

Note 2 — Coulomb interactions with periodic images need to be eliminated in plane wave basis set calculations of isolated systems. In the present work this is achieved by applying Hockney's method for the solution of the Poisson equation [124, 125] implemented in the CPMD code [105]. It requires an orthorhombic computational box large enough to ensure that the electron density is virtually zero at the border of the box.

H_2O. The plane wave basis set truncation leads to errors in computed total energies. To illustrate this, single-point DFT energy calculations are performed for water in the gas-phase using the PBE (Perdew, Burke, Ernzerhof) exchange–correlation functional [126] and Troullier–Martins pseudopotentials (see next section). The molecule is centred in cubic computational boxes of different size,[2] and the total energy is calculated using different basis set cut-off values. Results are plotted in Fig. 2.1. It shows that the total energy converges both with increasing kinetic energy cut-off and with increasing box size. The energy is virtually constant for boxes longer than 7 – 8 Å. In the first approximation the decay of the energy upon increasing the box size can be explained by the relaxation of the Coulomb electron–electron repulsion artificially imposed by limiting the volume available to the molecule's electrons.[3] For low cut-off values the total energy does not decay monotonically. Instead, random oscillations occur. Their amplitude mainly depends on the cut-off value, only slightly decreasing with increasing size of the box. At 50 Ry, energy fluctuations are about 10 – 15 kJ/mol, 1 – 2 kJ/mol at 70 Ry, and at cut-off values higher than 90 Ry the oscillations can be neglected. The discrete nature of the plane wave basis is the reason for this behaviour. With increasing size of the computational box the number of plane waves increases in integral steps only, leading to fluctuations in the number of plane waves per volume around its mean value. The less plane waves included in the basis set

[2] periodic images are decoupled

[3] It is not guaranteed that Hockney's method for the solution of the Poisson equation works correctly with small boxes.

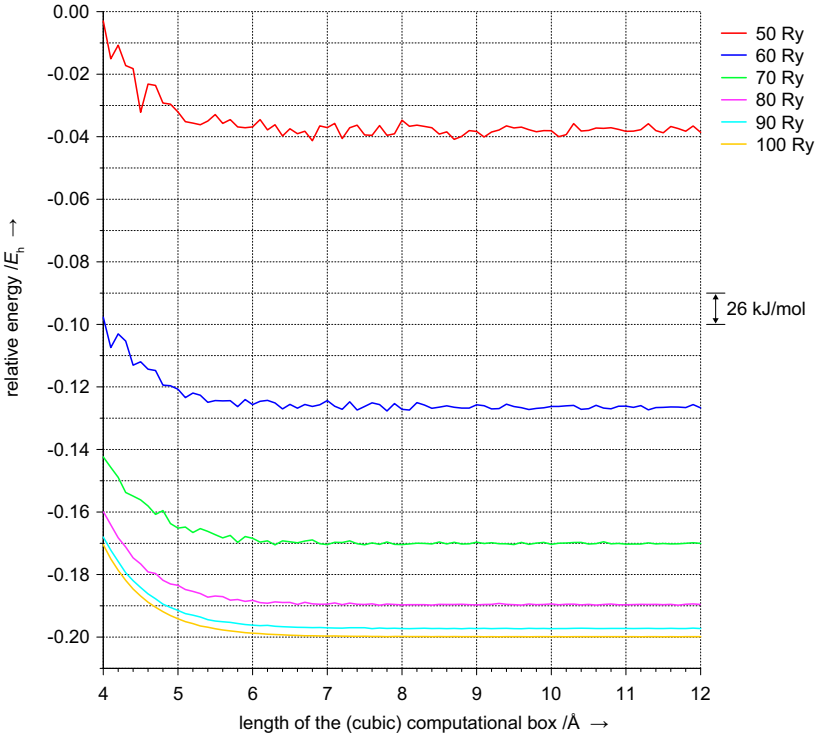

Figure 2.1: *Changes in the total energy of a water molecule centred in a cubic computational box as a function of the plane wave basis set cut-off and the size of the box (PBE functional, Troullier–Martins pseudopotentials)*

(*i. e.*, the smaller the cut-off), the higher the impact of these fluctuations on the total number of plane waves per volume and, therefore, on the total energy. It is emphasized at this point that simply the number of plane waves in the basis set does not constitute a criterion for total energy comparisons. It does make a clear difference in the total energy (even when the system is not affected by a too small volume of the box) whether a given number of plane waves results from a smaller box and higher cut-off or from a larger box and lower cut-off, see eqn. (2.3). Instead, the number of plane waves per volume or, equivalently, the cut-off value needs to be considered for that purpose.

Chabazite. In contrast to plane wave calculations of gas-phase systems the size of the computational box for a periodic system is limited to multiples of its unit cell. The cell size is determined by 6 parameters which belong to the structural degrees of freedom of the periodic system (lengths a, b, c of the vectors spanning the unit cell and angles α, β, γ between them). Their variation corresponds to movements on the system's potential energy surface. From the observations on the water molecule example described before it can be expected that at small cut-off values projections of the potential energy surface at cell parameter coordinates also show random oscillations due to the discrete nature of the plane wave basis. A simple system to demonstrate this effect is the all-silica form of the zeolite chabazite (CHA, see Chapter 3 for details). It has a rhombohedral unit cell ($a = b = c$, $\alpha = \beta = \gamma$) and the total energy can be plotted as a function of the two independent cell parameters, a and α. For a given set (a, α) the structure of all-silica chabazite is fully relaxed employing different plane wave basis set cut-off values.[4] Results are displayed in Fig. 2.2. As anticipated, with a too low cut-off value the potential energy surface shows irregularities. With 70 Ry they are about 0.01 E_h (26 kJ/mol) which is clearly more than the corresponding range for the water molecule (1 – 2 kJ/mol, 70 Ry). This is due to the higher number of atoms present in the unit cell of all-silica chabazite (36 instead of 3 atoms). With 90 Ry energy fluctuations are hardly visible (~ 1 kJ/mol), and 110 Ry let the energy surface appear perfectly smooth. In addition to the conclusions already drawn from the water molecule example one more point can be added here. Depending on the technique applied the optimisation of cell parameters can be hampered by energy fluctuations when using a too low plane wave basis set cut-off.

In practical plane wave calculations, however, a more severe problem is present when trying to optimise cell parameters. Computationally the number of plane waves is kept constant in programs following the Car-Parrinello [127] scheme (like the CPMD code does). From eqn. (2.3) it is evident that in case of a cell parameter optimisation a reduction of the cell volume results in a higher kinetic energy cut-off value, or *vice versa*. This is the reason why in stress tensor calculations contributions from Pulay stress (in analogy to Pulay forces [128]) appear when an insuffi-

[4] PBE functional and Troullier–Martins pseudopotentials; max. component of the Cartesian gradient $1 * 10^{-4}\ E_\mathrm{h}/a_0$

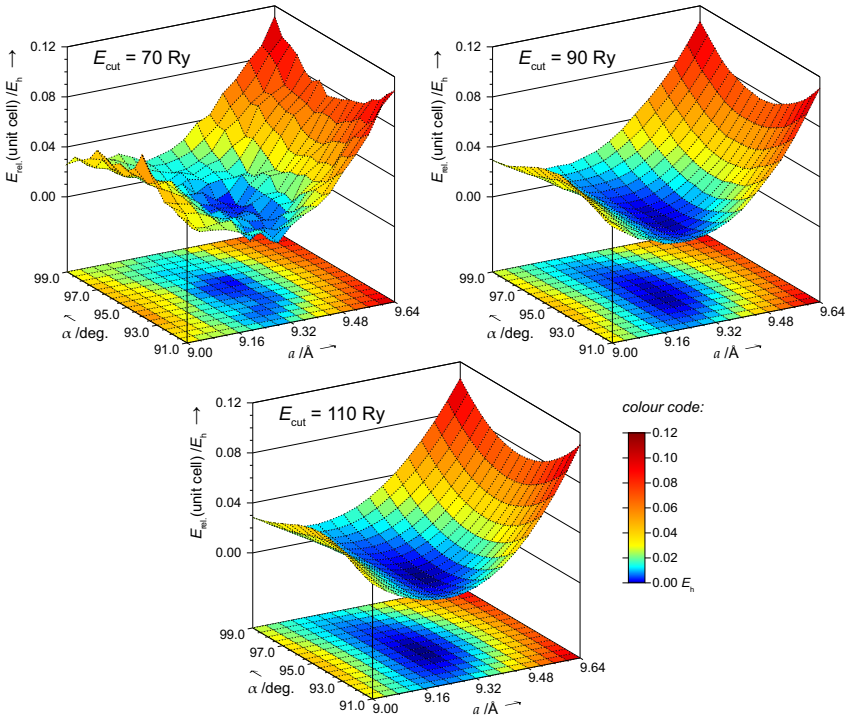

Figure 2.2: *Relative energy per unit cell for all-silica chabazite as a function of the unit cell parameters. Atom positions are fully relaxed using different plane wave basis set cut-off values (PBE functional, Troullier–Martins pseudopotentials)*

cient cut-off value is employed (see refs. [129–132]). In such cases the optimisation of cell parameters based on stress tensor calculations usually leads to underestimated cell volumes. To illustrate this stress tensor calculations are performed for selected structures of all-silica chabazite ($\alpha = 94.0°$) employing different cut-off values (*cf.* Fig. 2.2). For every stress tensor obtained differences in the diagonal elements σ_{ii} are small (less than 1 kbar). Therefore only σ_{11} is plotted as a function of the cell parameter a for different cut-off values, see Fig. 2.3. The σ_{11} values calculated at 70 Ry indicate that the stress tensor will be zero when parameter a is

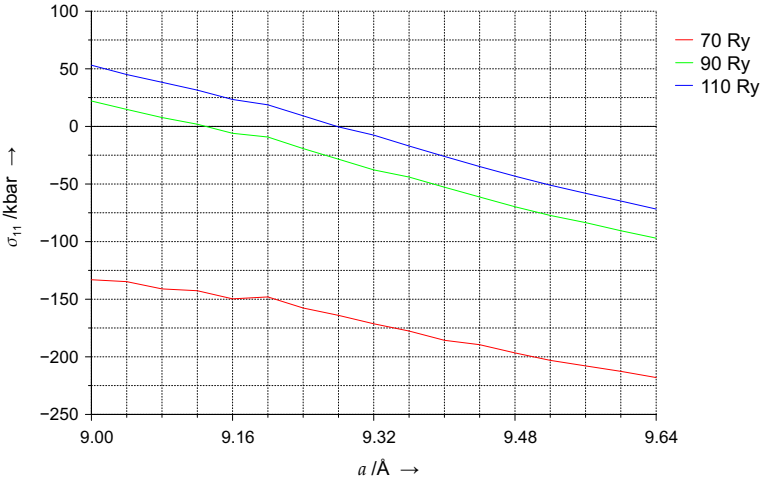

Figure 2.3: *Element σ_{11} of the stress tensor calculated for optimised structures of all-silica chabazite at different cut-off values as a function of the cell parameter a ($\alpha = 94.0°$, PBE functional, Troullier–Martins pseudopotentials)*

much smaller than 9 Å. This is in contrast to the potential energy surfaces obtained from calculations at constant cut-off (*cf.* Fig. 2.2). They show that the length of the relaxed cell parameter a (when $\alpha = 94.0°$) is approximately 9.28 – 9.32 Å. Employing 90 Ry for stress tensor calculations is still insufficient since σ_{11} vanishes at a too small a (~ 9.13 Å). Only the stress tensor calculations employing 110 Ry for the cut-off predict a reasonable value for the cell parameter a (9.28 Å). Different schemes correcting for Pulay contributions in stress tensor calculations exist (see ref. [133] and references therein). In this work additional efforts of that kind are not made since computational resources are available for a straightforward and consistent calculation of stress tensors employing a sufficiently high cut-off value. According to eqn. (2.3), however, the relaxation of the cell parameters is still coupled to changes in the effective cut-off value within a $N^{\mathrm{PW}} = const$ scheme. To avoid this effect, *i. e.*, to mimic a constant cut-off in variable cell calculations while keeping a constant number of plane waves in the basis set, a penalty function approach was introduced by Bernasconi *et al.* [134]. It suppresses those plane waves of which the corresponding kinetic energy (with respect to the current cell volume)

exceeds an effective cut-off value, $E_{\text{cut}}^{\text{eff}}$,

$$\widetilde{G}^2 = G^2 + A\left(1 + \text{erf}\left(\frac{\frac{1}{2}G^2 - E_{\text{cut}}^{\text{eff}}}{\sigma}\right)\right) \quad . \tag{2.4}$$

The parameters A and σ determine the height and width of the step function, respectively. In the limit $A \to 0$ the $N^{\text{PW}} = const$ behaviour is recovered. With $A \to \infty$ and $\sigma \to 0$, a constant (effective) cut-off value, $E_{\text{cut}}^{\text{eff}}$, is simulated. This scheme is implemented in the CPMD code. In this work it is applied for the cell parameter optimisation of ferrierite (Chapter 4).

The examples in this section show that for a given type of pseudopotential extensive test calculations are highly recommended in order to make a reasonable choice for the basis set kinetic energy cut-off value. This point is further illustrated in the next section where results obtained with different types of pseudopotentials are compared.

2.1.2 Atomic Pseudopotentials

The purpose and benefits from using atomic pseudopotentials in plane wave calculations have been mentioned in the last section. In this section details of the pseudopotentials applied in the present work are given and, with respect to their performance, comparison is made between them. For a deeper insight into pseudopotential theory the reader is referred to the literature [109, 114, 135].

Pseudopotentials are required to produce nodeless pseudowavefunctions (φ^{ps}) which match the all-electron wavefunction (φ^{ae}) outside a chosen atomic core radius (r_c). Inside this core region the pseudowavefunctions should be as smooth as possible to allow for a low plane wave basis set cut-off. In addition, pseudopotentials should be transferable, *i. e.*, one and the same pseudopotential is desired to show the same accuracy in different chemical environments. These goals partially impose conflicts upon the choice of r_c. A step towards a solution of this problem was made with the introduction of norm conservation (*cf.* [136, 137]),

$$\int_0^{r_c} \left|\varphi^{\text{ps}}\right|^2 \mathrm{d}r = \int_0^{r_c} \left|\varphi^{\text{ae}}\right|^2 \mathrm{d}r \quad . \tag{2.5}$$

Modern norm-conserving pseudopotentials, first developed and applied by Hamann *et al.* [138], are semi-local. For every angular momentum a different potential is used. Since there is no unique scheme how a norm-conserving pseudopotential is to be constructed, several proposals for their derivation from all-electron atom reference calculations exist. In this work norm-conserving pseudopotentials by Bachelet, Hamann and Schlüter ('BHS') [139] are used for second-row elements (aluminium and silicon). They are not employed for hydrogen and first-row elements due to the fact that electrons in $1s$, $2p$ ($3d$, $4f$) orbitals are exposed to the full core potential, *i. e.*, they are not screened. This imposes a challenge in the construction of norm-conserving pseudopotentials having these orbitals in the valence region, since both an optimum smoothness and high transferability are hard to obtain for these "difficult" elements of the periodic table. Introducing analytic expressions for the core part of the potential, Troullier and Martins ('TM') [140] suggested a new type of norm-conserving pseudopotential with improved plane wave basis set convergence properties while maintaining transferability and, therefore, applicability to problematic chemical elements. When employed in this work, TM pseudopotentials are used consistently for all elements of a given system. In CPMD calculations semi-local norm-conserving pseudopotentials are brought into the fully separable form of Kleinman and Bylander [141] to allow for savings in computational time when applying the Hamiltonian.

A somewhat different approach was taken by Vanderbilt ('Vdb') [142]. In his scheme the norm-conservation constraint is relaxed to allow for a much smaller plane wave basis set cut-off. As a consequence, augmentation charges are required, and a more complex projection scheme partially compensates for the savings in computational time. Due to the relaxed norm-conservation, "ultra"-soft Vdb pseudopotentials can be applied to first-row elements and transition metals. In this work they are used for hydrogen, oxygen, and carbon atoms in combination with norm-conserving BHS pseudopotentials on aluminium and silicon atoms.

Table B.2 (Appendix, page 136) lists the core radii r_c of all pseudopotentials employed in this work. They are generated from atomic all-electron calculations using the same density functional as in subsequent production work.

Table 2.1: *Gaussian basis set reference DFT calculations for the water dimer binding energy. BSSE corrected (uncorrected) values in kJ/mol*

basis set	N [a]	PBE	BP86
cc-pVTZ [b]	116	20.60 (28.66)	17.51 (24.48)
TZVPP [c]	118	21.25 (24.59)	18.00 (20.73)
QZVP [d]	234	21.17 (22.70)	17.82 (19.12)
aug-cc-pVTZ [e]	184	21.09 (21.33)	17.67 (17.91)
aug-TZVPP [c,f]	186	21.20 (21.52)	17.76 (18.18)
aug-QZVP [d,f]	348	21.19 (21.24)	17.73 (17.78)

[a] total number of contracted spherical basis functions for the water dimer; [b] ref. [155]; [c] ref. [156], polarisation functions taken from cc-pVTZ; [d] ref. [157], polarisation functions taken from cc-pVQZ [155]; [e] ref. [158]; [f] diffuse functions taken from corresponding aug-cc-pV*X*Z basis sets [158]

$(H_2O)_2$. The water dimer is the first example in a series of tests for the assessment of the pseudopotentials employed in this work. This system is a prototype for hydrogen bonding and has already been subject of many computational studies (see, *e. g.*, recent publications [93, 98, 143–150] and references therein). For the dissociation into the monomers,

$$(H_2O)_2 \longrightarrow 2\ H_2O \quad , \tag{2.6}$$

the energy is calculated with different density functionals and different types of pseudopotentials. DFT results obtained employing Gaussian basis sets are used as reference values. Corresponding calculations are performed using the TURBOMOLE [151, 152] program package.[5] Binding energies obtained with the PBE (Perdew, Burke, and Ernzerhof [126]) and BP86 (Becke [153], Perdew [154]) exchange–correlation functionals are listed in Tab. 2.1. The results show that increasing the basis set size by adding diffuse functions reduces the BSSE more efficiently than extending the core–valence part by going from a triple-ζ to a quadruple-ζ basis set. Using both these options in the aug-QZVP basis set the BSSE is reduced to less than 0.1 kJ/mol. BSSE corrected binding energies obtained with this basis set serve as reference values for comparison to plane wave basis set

[5] grid "m4", full structure relaxations to reduce the Cartesian gradient norm below $1 * 10^{-4}\ E_h/a_0$

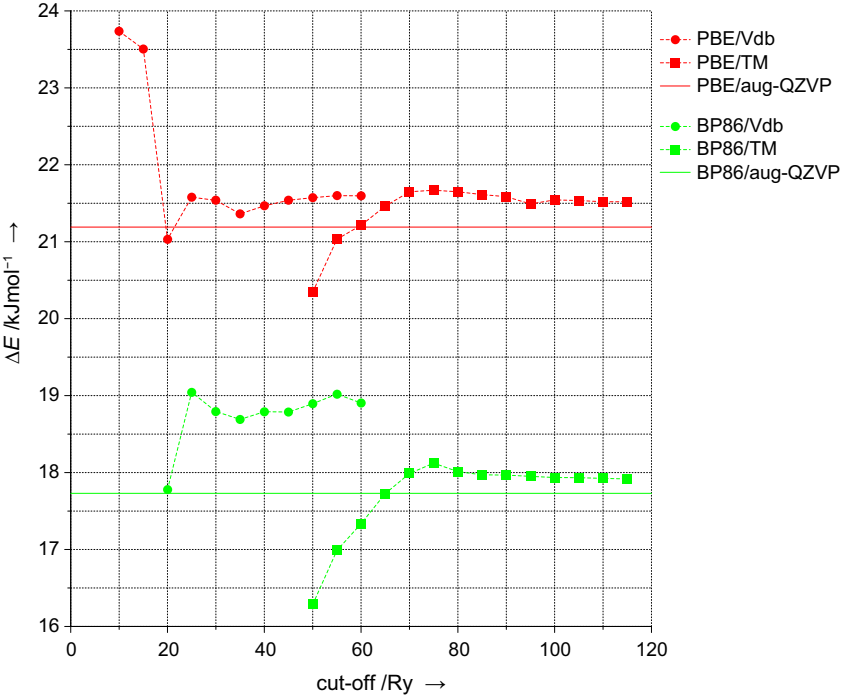

Figure 2.4: *Plane wave DFT water dimer binding energies with different pseudopotentials as a function of the basis set cut-off. Solid lines are BSSE corrected Gaussian basis set reference values*

results. In corresponding CPMD calculations structures of the water dimer and monomer are fully relaxed[6] using different plane wave basis set cut-off values together with either ultrasoft (Vdb) or norm-conserving (TM) pseudopotentials. Results for the water dimer binding energy are plotted in Fig. 2.4. In each case the binding energy converges with increasing cut-off value. Using TM pseudopotentials binding energies are virtually constant at cut-off values higher than 100 Ry. At 70 Ry they are already converged within ~0.2 kJ/mol accuracy. Compared to the examples

[6] max. component of the Cartesian gradient $5 * 10^{-5}\ E_h / a_0$; employing a 10 Å cubic computational box (decoupled periodic images)

already shown in this chapter, 70 Ry might be less than the expected cut-off value for converged results. The dimer binding energy, however, is a relative number calculated from differences in total energies. The latter are obtained with one and the same plane wave basis set for both the dimer and the monomer, and this is the reason why no fluctuations in the binding energy (*e. g.*, several kJ/mol as seen in Fig. 2.1) occur for small cut-off values. Both the converged PBE/TM and BP86/TM results agree to their reference values within less than 0.4 kJ/mol. With Vdb pseudopotentials the situation is slightly different, *i. e.*, the binding energies converge less clearly and deviate from their reference values by up to ~1 kJ/mol (BP86/Vdb). This is certainly no surprise when putting up with the drawbacks of the ultrasoft pseudopotential concept.

Apart from binding energies obtained with different pseudopotentials and plane wave basis sets, geometry parameters of the water dimer can also be compared to corresponding reference values (aug-QZVP basis set). Figure 2.5 shows calculated intermolecular distances $r_{O\cdots O}$ and lengths of the donor O–H bond $r_{O-H(\cdots O)}$. The $r_{O\cdots O}$ reference values (PBE: 290.1 pm, BP86: 290.0 pm) are reproduced with error bars of less than 1 pm for TM pseudopotentials and cut-off values of 75 Ry and higher. With Vdb pseudopotentials and cut-off values of at least 25 Ry deviations do not exceed 2 pm. Reference values for $r_{O-H(\cdots O)}$ (PBE: 97.9 pm, BP86: 98.0 pm) are met best within errors of 0.1 – 0.2 pm employing TM pseudopotentials and relatively high cut-off values of more than 90 Ry. Lower accuracy is observed again for Vdb pseudopotentials, that is, with 25 Ry $r_{O-H(\cdots O)}$ is overestimated by 0.6 pm, and this only slightly improves with increasing kinetic energy cut-off.

Note — Different expressions are used in the CPMD and TURBOMOLE programs for the local density approximation (LDA) part of PBE and BP86 gradient corrected density functional calculations. A computationally efficient Padé form for exchange and correlation [159] is employed in the CPMD code for both PBE and BP86. In the TURBOMOLE package Slater–Dirac exchange [160, 161] is combined with correlation functionals either by Vosko, Wilk, and Nusair for BP86 (ref. [162], proposal "V" therein) or by Perdew and Wang [163] for PBE calculations. As already shown in an earlier work [164] the water dimer binding energy can change by up to 0.5 kJ/mol when different forms of the LDA part are used. Considering this point and, in addition, that the error due to the pseudopotential

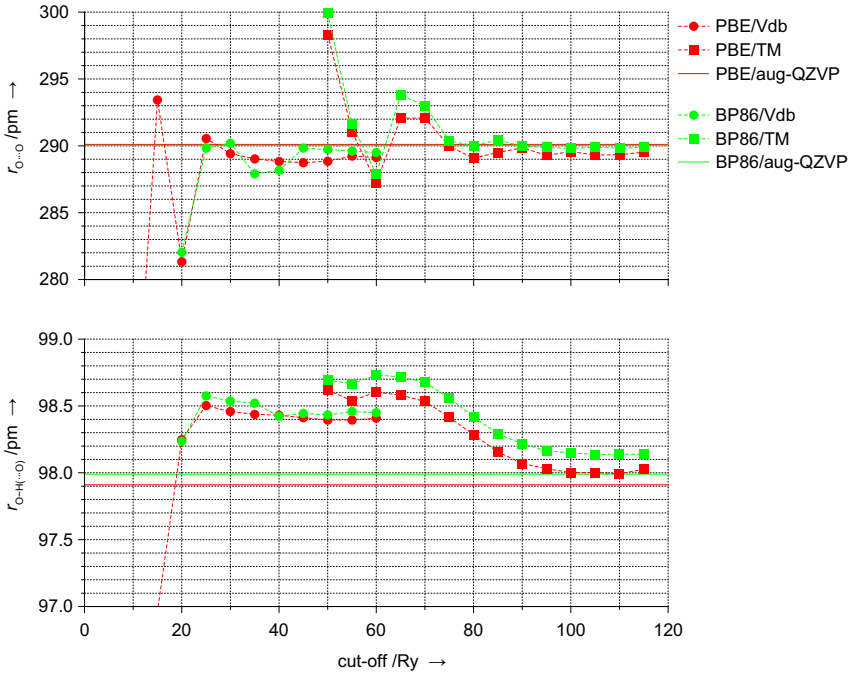

Figure 2.5: *Plane wave DFT atomic distances for the water dimer with different pseudopotentials as a function of the basis set cut-off. Solid lines are Gaussian basis set reference values*

approach does not necessarily need to vanish for high cut-off values, errors of less than 0.4 kJ/mol for the water dimer binding energy and ~ 0.2 % for corresponding atomic distances (TM pseudopotentials) appear acceptable for the purpose of this work.

CH_3OH. To locate stationary points on potential energy surfaces (PES), standard algorithms for structure optimisation are used in general. This requires the calculation of energies and energy gradients. Further insight into the shape of the PES at a given point can be gained by force constant calculations. Besides the generation of vibrational spectra in the harmonic approximation, this type of information is important to esti-

mate zero-point vibrational energy and finite temperature contributions to thermodynamic quantities. Therefore the accuracy of the plane wave pseudopotential approach regarding force constant calculations needs to be assessed as well. The methanol molecule represents a small test system containing most of the different covalent bonds relevant in this work (C – O, C – H, O – H). Again, Gaussian basis set reference DFT (PBE) calculations are made using the TURBOMOLE code, see Tab. B.3 for frequencies of all stretching modes. These data show that with growing size of the basis set not all frequencies are converged within a range of ± 1 cm^{-1}. Considering their changes when going from TZVPP to QZVP and from QZVP to aug-QZVP basis sets and, compared to fully analytical calculations, the additional noise inherent to numerical differentiations the error in the aug-QZVP frequencies serving as reference data is expected to be 5 cm^{-1} at most. A series of different plane wave basis set cut-off values is used for corresponding CPMD force constant calculations[7] employing either norm-conserving (TM) or ultrasoft (Vdb) pseudopotentials. Figure 2.6 shows the results for the stretching mode frequencies. Using Vdb pseudopotentials frequencies are virtually converged at 30 Ry cut-off, constantly underestimating corresponding reference values. Deviations up to 25 cm^{-1} are observed for the ν(C-H) and ν(C-O) modes, *i. e.*, vibrations involving the carbon atom. With TM pseudopotentials all frequencies are converged at 110 Ry. Frequencies are underestimated by up to 20 cm^{-1} for vibrational modes involving oxygen atoms (ν(O-H) and ν(C-O)). For the ν(C-H) frequencies, however, only 90 Ry are required to obtain converged results. They are reproduced within the error bar of 5 cm^{-1} assumed for the numerical accuracy of the Gaussian basis set reference values.

Chabazite. Employing a low basis set cut-off plane wave pseudopotential DFT simulations are most efficient compared to Gaussian basis set approaches when systems of several hundred atoms are calculated under periodic boundary conditions. This, in general, requires the use of soft or even ultrasoft pseudopotentials. For this reason another series of test cal-

[7] employing a 8.5 Å cubic computational box (decoupled periodic images); full structure relaxations (max. component of the Cartesian gradient $1 * 10^{-4}$ E_h/a_0); ± 0.01 a_0 atom displacements for numerical differentiation of forces, translations and rotations projected from the Hessian matrix

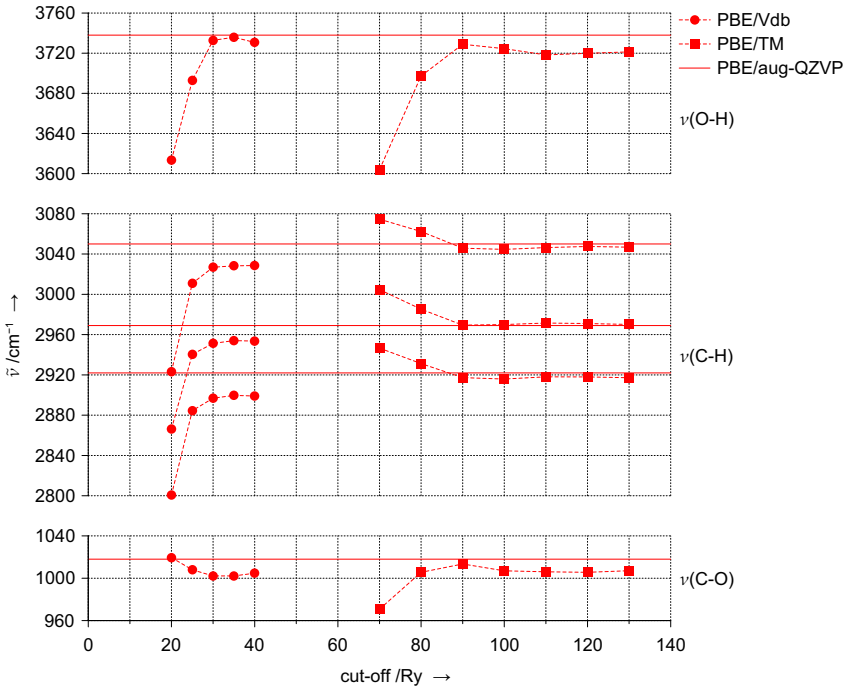

Figure 2.6: *Stretching modes of the methanol molecule from numerical force constant calculations using plane wave DFT (PBE) and different pseudopotentials. Corresponding frequencies are given as a function of the basis set cut-off, solid lines are Gaussian basis set reference values*

culations is performed on a periodic system representing the main class of substances investigated in this work, a zeolite. The Brønsted acid form of chabazite, H-SSZ-13 (stoichiometry $HAlSi_{11}O_{24}$, see Chapter 3) is selected due to its relatively small unit cell. Among the four different oxygen sites O(1) – O(4) of the $Al[O_{1/2}]_4$ tetrahedron hosting the charge compensating proton there are two atoms, O(2) and O(3), where two stable proton sites, 'a' and 'b', are found. For each of these (in total six) proton sites constant pressure ion-pair shell-model potential calculations are performed to obtain relaxed atom positions and cell parameters [86]. Using these structures the total energy of H-SSZ-13 is calculated for different proton

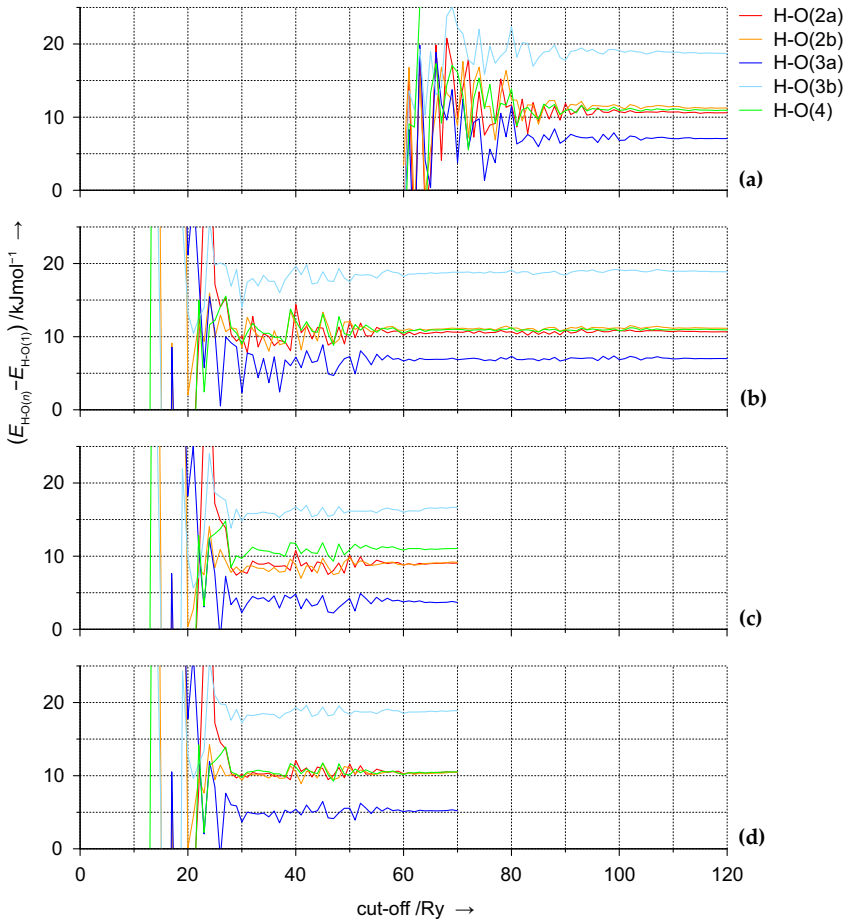

Figure 2.7: *Relative stabilities of different proton sites (compared to H-O(1)) in acidic chabazite as a function of the plane wave basis set cut-off and various (Al,Si) – (H,O) pseudopotential combinations: TM – TM* ***(a)****, TM – Vdb* ***(b)****, Vdb – Vdb* ***(c)****, and BHS – Vdb* ***(d)***

sites with plane wave DFT (PBE) as a function of the basis set cut-off and various pseudopotential combinations, see Fig. 2.7. For reasons already discussed in the last section, in each of the four plots (a) – (d) random

oscillations occur at the lower end of the corresponding cut-off range. With TM pseudopotentials for all atoms converged results are obtained at cut-off values higher than 90 Ry (Fig. 2.7a). Subsequently the relative stabilities obtained here serve as reference values because the reliability of norm-conserving TM pseudopotentials has already been demonstrated in this section. To reduce the cut-off required for converged energies ultrasoft pseudopotentials are introduced for hydrogen and oxygen atoms. Figure 2.7b shows that this results in virtually the same relative energies at a considerably smaller cut-off around 60 Ry. To lower the cut-off further TM pseudopotentials for aluminium and silicon atoms need to be replaced by softer pseudopotentials. Chosing Vdb pseudopotentials for these elements the cut-off can finally be reduced to only 30 Ry. Unfortunately, errors up to 4 kJ/mol are introduced for the relative stabilities of different proton sites (Fig. 2.7c). For second-row elements, however, soft pseudopotentials of the BHS type are available with two advantages over Vdb pseudopotentials: fulfillment of the norm-conservation constraint and reduced computational effort. With BHS pseudopotentials on aluminium and silicon atoms the maximum error in relative energies reduces to 2 kJ/mol, and 30 Ry are still sufficient for converged results (Fig. 2.7d). Therefore Vdb pseudopotentials for aluminium and silicon atoms are not considered further in this work, and no efforts are made to change internal parameters related to their generation. The BHS pseudopotential cut-off radii shown in Tab. B.2 are optimum values. They have been systematically determined in numerous similar series of calculations to reproduce the TM results (Fig. 2.7a) as close as possible.

Force constant calculations[8] are performed on optimised structures[9] with the proton at its favoured site H-O(1). This is done for different pseudopotential combinations. The vibrational frequency of the ν(H-O(1)) mode as a function of the plane wave basis set cut-off is plotted in Fig. 2.8. Similarly to the results obtained for the methanol molecule (see Fig. 2.6) with a too small basis set the ν(H-O(1)) frequency is underestimated by more than one hundred wavenumbers. Employing TM pseudopotentials plane wave basis set cut-off values higher than 110 Ry yield converged frequencies. These are reproduced within 2 cm^{-1} accuracy when Vdb pseudopotentials and cut-off values between 30 and 40 Ry are used.

[8] $\pm 0.01\ a_0$ atom displacements, translational modes projected from the Hessian matrix

[9] max. component of the Cartesian gradient $1 * 10^{-4}\ E_h/a_0$

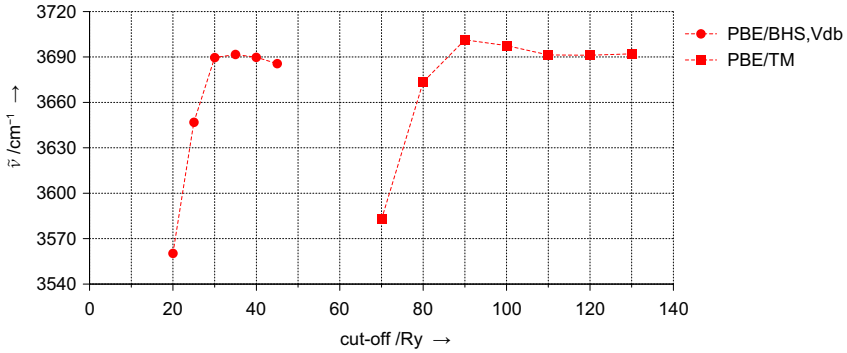

Figure 2.8: *Vibrational frequency of the ν(H-O(1)) stretching mode in zeolite H-SSZ-13 calculated with different pseudopotential combinations as a function of the plane wave basis set cut-off*

2.1.3 Density Functionals

As already mentioned in the introduction (Section 1.1) it is difficult to describe weak interactions using standard DFT methods. For non-bonded interactions dispersion can be the dominant contribution resulting in binding energies of only a few kJ/mol in case of a small system. The intention behind this part of the present work is not to evaluate the performance of all existing proposals and classes of density functionals for weakly interacting systems. Such work has recently been done in a comprehensive study by Zhao and Truhlar [18]. Instead, two questions are addressed. First, whether the plane wave pseudopotential approach affects the DFT description of weak interactions and, second, which of the GGA available in plane wave DFT codes to use. Inspired by the work of Tsuzuki and Lüthi [14] the interaction potential of the methane dimer (symmetry point group D_{3d}) is recalculated[10] using plane wave basis sets and TM pseudopotentials. The BLYP (Becke [153], Lee, Yang, and Parr [165]), BP86 (Becke [153], Perdew [154]), PBE (Perdew, Burke, and Ernzerhof [126]), and PW91 (Perdew and Wang [163, 166, 167]) gradient corrected density functionals as well as the local density approximation (LDA) are chosen.

[10] employing an orthorhombic 8 x 8 x 16 Å^3 computational box (decoupled periodic images); optimised monomer geometries (max. component of the Cartesian gradient $1 * 10^{-5}\ E_h / a_0$)

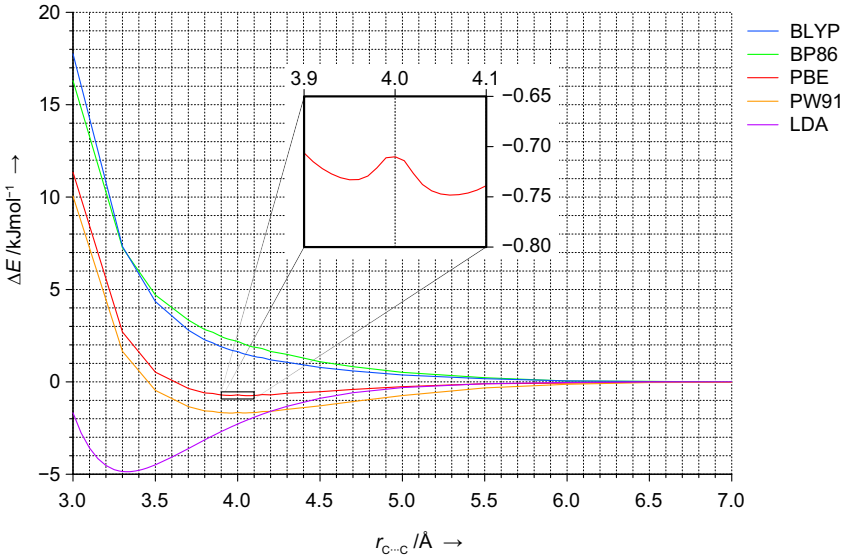

Figure 2.9: *Methane dimer binding energies ΔE as a function of the intermolecular distance $r_{C\cdots C}$ for various density functionals using plane waves (110 Ry kinetic energy cut-off) and TM pseudopotentials*

Depending which functional is used the potential curves obtained (see Fig. 2.9) are of different nature. Functionals involving Becke's exchange gradient correction (*i. e.*, BLYP and BP86) yield repulsive forces between the methane molecules in agreement to the Gaussian basis set results by Tsuzuki and Lüthi for the BLYP and B3LYP functionals. It is a known feature of the Becke exchange functional to introduce too much repulsion in van der Waals systems, see the analyses by Wesołowski *et al.* [12, 168], Zhang *et al.* [169], references therein, and recent comparative studies [18, 144, 170]. Compared to coupled-cluster reference data ($r_{C\cdots C} = 3.6$ Å, $\Delta E = -2.1$ kJ/mol [14, 18]) the LDA, as expected,[11] shows overbinding ($r_{C\cdots C} = 3.3$ Å, $\Delta E = -4.9$ kJ/mol) and is not considered further in this work. The minimum of the plane wave PW91 potential energy curve ($r_{C\cdots C} = 4.0$ Å, $\Delta E = -1.7$ kJ/mol) matches the Gaussian basis set result by Tsuzuki and Lüthi ($r_{C\cdots C} = 4.0$ Å, $\Delta E = -1.6$ kJ/mol) very well. Using the

[11] see, *e. g.*, refs. [18, 21, 144] and references therein

closely related PBE functional a more shallow minimum is found at the same intermolecular distance. Compared to Becke exchange type density functionals the at least qualitatively better description of van der Waals systems by the PW91 and PBE models suggests the use of the latter for the study of weak host–guest interactions in zeolites.

In plane wave DFT codes fast Fourier transforms (FFT) are employed to calculate quantities required in the framework of DFT most efficiently in either real space or reciprocal space. The integral for the gradient corrected exchange–correlation energy is replaced by a sum over functional values on the real space points of the minimum FFT grid.[12] This sum, however, is an approximation to the true value since exchange and correlation functionals show complicated analytic expressions of the electron density of which high-frequency Fourier components require an FFT grid with infinite resolution. To avoid stability problems in the self-consistency cycle, the conventional derivation of the gradient corrected exchange–correlation potential is replaced by a modified definition along the FFT grid points in correspondence with the discrete sum for the exchange–correlation energy [105, 171]. This way an undesired side effect, known as the "ripple effect", is introduced, that is, the total energy of a system depends on the atom positions relative to the FFT grid points. Such modulations of the energy can be observed upon close inspection of, *e. g.*, the methane dimer PBE potential energy curve (see Fig. 2.9). Depending on the system size, these energy modulations are small, usually far less than 1 kJ/mol. They can be reduced by increasing the size of the FFT grid, but this way computations become more expensive. Figure 2.10 illustrates the ripple effect more clearly. A single methane molecule is moved from the central point of an orthorhombic $8 \times 8 \times 16$ Å^3 computational box along a line in z-direction connecting several FFT grid points. Its total energy along this line is calculated[13] employing FFT grids of different size.[14] The energy changes periodically, reproducing exactly the z-direction spacing of the FFT grids.[15] As expected, for the denser FFT grid the magnitude of the energy oscillations is reduced compared to the results from the

[12] The minimum FFT grid is defined as the smallest to unambiguously represent the electron density, determined by the wavefunction expansion into a finite number of plane waves.

[13] PBE functional, TM pseudopotentials, 70 Ry kinetic energy cut-off, single-point energy calculations on the relaxed structure

[14] $90 \times 90 \times 162$ (default) and $108 \times 108 \times 216$ grid points

[15] 16 Å/162 points = 0.099 Å/point and 16 Å/216 points = 0.074 Å/point, respectively

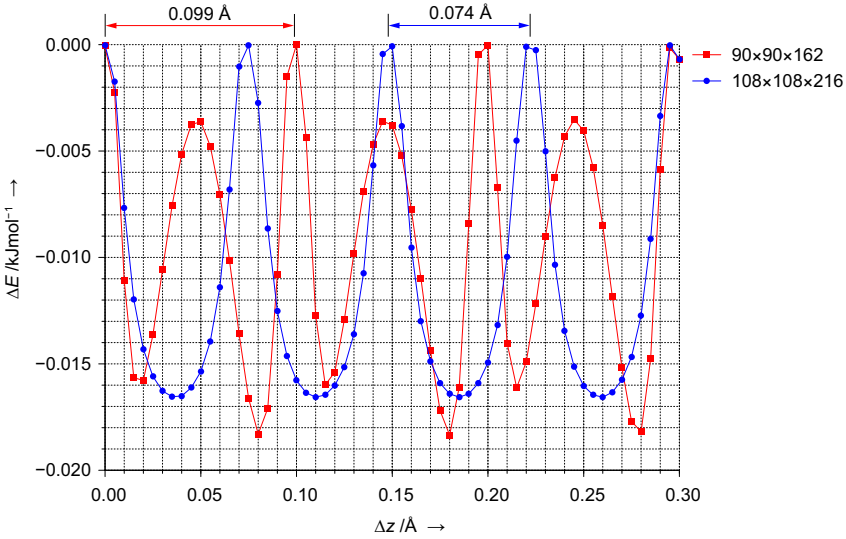

Figure 2.10: *Illustration of the ripple effect – energy fluctuations upon translation of a methane molecule in an orthorhombic 8 x 8 x 16 Å^3 computational box from the central point along z-direction employing two different real space FFT grids (PBE functional, 70 Ry kinetic energy cut-off and TM pseudopotentials)*

smaller grid. In relation to other approximations introduced with the pseudopotential plane wave approach, the ripple effect certainly does not constitute a serious problem in energy calculations on the one hand. On the other hand, since potential energy surfaces are slightly modified, the determination of numerical highly accurate structures or harmonic frequencies might require large and computationally very expensive FFT grids.

2.2 MP2 Calculations

2.2.1 FC and RI Approximations

The formal $\mathcal{O}(\mathcal{N}^5)$ computational scaling behaviour clearly imposes limits to the system size $\mathcal{N}$ for second-order Møller–Plesset perturbation theory (MP2) [51] calculations. A widely used and simple approach to reduce the computational cost in electronic structure calculations is the sole consideration of electrons in valence orbitals. The assumption made is that correlation energy contributions from electrons in core orbitals are nearly constant for reacting systems. Similar ideas also hold for the pseudopotential approach in plane wave basis set calculations. When *post* HF methods are employed electrons in core orbitals can be excluded from the given correlation scheme. To distinguish this case from the all-electron (ae) correlation treatment it is referred to as the "frozen core" (fc) approach. Virtually all MP2 calculations of the present work are performed employing a frozen core. However, as with any approximation used, it is important to know the order of magnitude of the error introduced by it, particularly when comparison to experimental data or to results of more sophisticated calculations is intended. A proper choice of orbitals for the frozen core can be a nontrivial task, that is, when the molecular core is not consistent with possible definitions of corresponding atomic cores or when significant core–valence mixing effects occur (see, *e. g.*, refs. [172, 173]). To assess the error related to the frozen core approach for calculations done in this work a small zeolite cluster model (Fig. 2.11) is chosen for a series of single-point Brønsted acid site water binding energy calculations. The cluster model geometry[16] is obtained by relaxation of all bond lengths including the $O_{water} \cdots O_{acid\ site}$ distance using MP2(ae)[17] and Ahlrichs' T(O)DZP basis set.[18] For this system reference MP2(ae) values are obtained[19] employing different combinations of Dunning's correlation-consistent polarised valence basis sets (cc-pV*X*Z), augmented

[16] originally being the 2T cluster model of a hybrid MP2/DFT optimised structure for water adsorbed in zeolite H-SSZ-13 [164]

[17] calculated with the TURBOMOLE code [151, 174]

[18] TZ basis set on oxygen atoms with an additional polarisation function (exponent 1.2); DZ basis sets for aluminium, silicon, and hydrogen with additional polarisation functions (exponents 0.3, 0.35, and 0.8, respectively) [175]

[19] using the TURBOMOLE [151, 174] and MOLPRO [176] codes

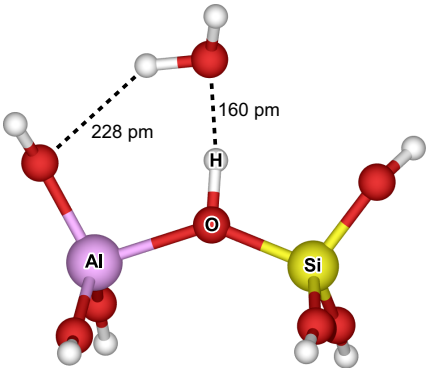

Figure 2.11: *2T cluster model for water adsorption at a zeolite Brønsted acid site*

by additional sets of diffuse basis functions (aug-cc-pVXZ), by tight basis functions (cc-pCVXZ), or by both these extensions [155, 158, 177–179]. For the hydrogen, aluminium, and silicon atoms $X = \mathrm{T}$ and for the oxygen atoms $X = \{\mathrm{T}, \mathrm{Q}\}$ is chosen, see Tab. 2.2. Comparison of the three vertical sections within this table shows that a gradual introduction of tight basis functions for core correlation effects reduces the MP2 based BSSE by amounts up to 4.3 kJ/mol. In relation to that, counterpoise corrected correlation energy contributions, $\Delta E^{\mathrm{cp}}_{\mathrm{MP2}}$, increase by only 0.1 – 0.3 kJ/mol. For a more precise estimate of the additional gain in core–core and core–valence correlation energy from additional tight basis set functions, extrapolation schemes for the complete basis set (CBS) limit are applied. Due to high computational costs only the oxygen basis set cardinal number X is increased from $X = \mathrm{T}$ (triple-ζ) to $X = \mathrm{Q}$ (quadruple-ζ). For this reason a rather rough estimate of the CBS limit (more likely an "oxygen CBS limit"), $\Delta E^{\mathrm{cp},\infty}_{\mathrm{MP2}}$, is obtained using a 2-point extrapolation scheme (see next section for details). Corresponding values are included in the last column of Tab. 2.2. With respect to the introduction of additional core correlation basis functions on all atoms changes are 0.1 kJ/mol in the CBS estimates of the MP2(ae) water binding energy. Obviously, this corresponds to the intrinsic error in the CBS limit obtained when all-electron calculations are made using valence-only polarised basis sets [178].

Table 2.2: *Conventional MP2(ae) single-point calculations for the 2T zeolite cluster model water binding energy using different combinations of Dunning's correlation-consistent basis sets. Uncorrected and counterpoise corrected correlation energy contributions, ΔE_{MP2} and ΔE_{MP2}^{cp}, and (oxygen) CBS limits, $\Delta E_{MP2}^{cp,\infty}$, are given (in kJ/mol)*

H, Al, Si	O	N [a]	ΔE_{MP2}	$\Delta E_{\mathrm{MP2}}^{\mathrm{cp}}$	$\Delta E_{\mathrm{MP2}}^{\mathrm{cp},\infty}$
cc-pVTZ	cc-pVTZ	434	24.78	13.95	18.07
	cc-pVQZ	634	21.88	16.33	
	aug-cc-pVTZ	562	23.43	15.97	18.74
	aug-cc-pVQZ	834	21.77	17.57	
cc-pVTZ	cc-pCVTZ	538	23.04	14.20	18.13
	cc-pCVQZ	866	21.33	16.47	
	aug-cc-pCVTZ	666	20.20	16.19	18.80
	aug-cc-pCVQZ	1066	20.96	17.70	
cc-pCVTZ [b]	cc-pCVTZ	588	22.69	14.26	18.17
	cc-pCVQZ	916	20.87	16.52	
	aug-cc-pCVTZ	716	19.42	16.21	18.84
	aug-cc-pCVQZ	1116	19.60	17.73	

[a] total number of contracted spherical basis functions for the adsorption complex
[b] cc-pVTZ for hydrogen

Analogous calculations with a frozen core are performed[20] employing correlation-consistent polarised valence basis sets without additional tight basis functions for core correlation. The frozen core is chosen to represent electrons in the ten lowest-energy Hartree–Fock orbitals, that is, those molecular orbitals corresponding to the silicon 1*s* (−68 E_{h}), aluminium 1*s* (−58 E_{h}), and oxygen 1*s* (−21 E_{h}) atomic orbitals. Results are listed in Tab. 2.3. Upon direct comparison of the uncorrected and counterpoise corrected correlation energy contributions obtained for basis sets of the same quality (Tabs. 2.2 and 2.3), it can be seen that

$$\mathrm{BSSE}_{\mathrm{MP2(ae)}}^{\text{(aug)-cc-pCVXZ}} < \mathrm{BSSE}_{\mathrm{MP2(fc)}}^{\text{(aug)-cc-pVXZ}} < \mathrm{BSSE}_{\mathrm{MP2(ae)}}^{\text{(aug)-cc-pVXZ}} \quad . \tag{2.7}$$

[20] using the TURBOMOLE [151, 174] and NWCHEM [180] codes

Table 2.3: *Conventional MP2(fc) single-point calculations for the 2T zeolite cluster model water binding energy using different combinations of Dunning's correlation-consistent basis sets. Uncorrected and counterpoise corrected correlation energy contributions, ΔE_{MP2} and ΔE_{MP2}^{cp}, and selected (oxygen) CBS limits, $\Delta E_{MP2}^{cp,\infty}$, are given for comparison with Tab. 2.2 (all numbers in kJ/mol)*

H, Al, Si	O	ΔE_{MP2}	$\Delta E_{\mathrm{MP2}}^{\mathrm{cp}}$	$\Delta E_{\mathrm{MP2}}^{\mathrm{cp},\infty}$
cc-pVDZ	cc-pVDZ	21.53	5.89	
	cc-pVTZ	20.51	12.59	
	cc-pVQZ	20.11	15.46	
	cc-pV5Z	19.65	16.72	
	aug-cc-pVDZ	17.72	11.42	
	aug-cc-pVTZ	19.98	15.34	
	aug-cc-pVQZ	21.25	17.09	
	aug-cc-pV5Z	21.44	17.87	
cc-pVTZ	cc-pVTZ	22.86	13.73	} 17.66
	cc-pVQZ	21.05	16.01	
	cc-pV5Z	19.93	17.16	
	aug-cc-pVTZ	20.10	15.74	} 18.34
	aug-cc-pVQZ	20.68	17.24	
	aug-cc-pV5Z	21.37	17.97	
cc-pVQZ	cc-pVQZ	22.53	16.65	
	cc-pV5Z	21.98	17.53	
	aug-cc-pVQZ	21.21	17.47	
cc-pV5Z	cc-pV5Z	20.13	17.79	

In addition, counterpoise corrected binding energies from frozen core calculations are always smaller than from all-electron calculations. For a quantitative comparison frozen core CBS limits are also estimated, see last column in Tab. 2.3. They are smaller by 0.4 kJ/mol compared to the all-electron CBS limits obtained using identical valence-only polarised basis sets. Adding 0.1 kJ/mol gained from core–core and core–valence correlation effects employing core–valence polarised basis sets the resulting estimate for the error in the 2T zeolite cluster model water binding energy due to the frozen core approximation amounts to 0.5 kJ/mol.

(Numbers in Tab. 2.3 obtained with basis sets not explicitly considered so far will serve as reference values in the next section and, if appropriate, will be discussed later on in the context of basis set choices for production work.)

The expression for the MP2 correlation energy

$$E_{\mathrm{MP2}} = \frac{1}{4} \sum_{abrs} \frac{|\langle ab \| rs \rangle|^2}{\varepsilon_a + \varepsilon_b - \varepsilon_r - \varepsilon_s} \tag{2.8}$$

contains four-index integrals

$$\langle ab \| rs \rangle = (ar|bs) - (as|br) \tag{2.9}$$

over occupied (a, b) and virtual (r, s) Hartree–Fock self-consistent field (SCF) molecular orbitals. Such integrals are obtained from four-centre integrals $(\mu\nu|\kappa\lambda)$ over atomic orbital basis functions by transformation to the molecular orbital basis. This is the bottleneck in conventional MP2 calculations giving rise to the $\mathcal{O}(\mathcal{N}^5) = \mathcal{O}(n_{\mathrm{occ}} N^4)$ scaling of the operation count (n_{occ} active occupied molecular orbitals, N basis functions). Computational costs can be reduced by an approximate representation of four-centre integrals using an expansion of orbital products (densities) into a set of N_{aux} auxiliary basis functions P,

$$\mu(r)\nu(r) = \rho_{\mu\nu}(r) \approx \tilde{\rho}_{\mu\nu}(r) = \sum_{P}^{N_{\mathrm{aux}}} D_{\mu\nu}^{P} P(r) \quad . \tag{2.10}$$

The expansion coefficients are obtained by minimising the Coulomb self-interaction of the residual density $(\rho_{\mu\nu} - \tilde{\rho}_{\mu\nu})$ [181, 182] leading to

$$D_{\mu\nu}^{P} = \sum_{Q}^{N_{\mathrm{aux}}} (\mu\nu|Q) \, [V^{-1}]_{QP} \tag{2.11}$$

with V being the Coulomb-metric matrix,

$$V_{QP} = (Q|P) = \iint Q(r_1) \frac{1}{|r_1 - r_2|} P(r_2) \mathrm{d}r_1 \mathrm{d}r_2 \quad , \tag{2.12}$$

such that

$$(\mu\nu|\kappa\lambda) \approx \sum_{P}^{N_{\mathrm{aux}}} D_{\mu\nu}^{P} \, (P|\kappa\lambda) = \sum_{PQ}^{N_{\mathrm{aux}}} (\mu\nu|Q) \, [V^{-1}]_{QP} \, (P|\kappa\lambda) \tag{2.13}$$

is the result of the density fitting (DF) for four-centre integrals. Equation (2.13) formally looks like a "resolution of the identity" (RI) when the expression $(Q|P)^{-1}$ is substituted for the matrix element $[V^{-1}]_{QP}$. Reducing the operation count from $\mathcal{O}(N^4)$ to $\mathcal{O}(N^2 N_{\text{aux}})$ at this stage, only three- and two-index integrals are required to compute the much more numerous four-index integrals.[21] For this reason RI (DF) techniques have a long history in *ab initio* computational chemistry (see, *e. g.*, refs. [181–189] and references therein). They are implemented for Coulomb integrals in HF-SCF and DFT codes [190–194], for HF-SCF exchange integrals [195–199], as well as in MC-SCF [200], MP2 [198, 201–205], and coupled-cluster [206–208] electronic structure codes. Feyereisen *et al.* [201] were the first who applied the RI approach successfully in MP2 energy calculations employing Dunning's series of correlation-consistent basis sets [155, 158] for orbital product expansions. Today optimised auxiliary bases are available [209–212] for standard basis set (Ahlrichs *et al.*, Dunning *et al.*) RI-MP2 calculations.

Compared to exact MP2 it should be noted that in RI-MP2 calculations the computational bottleneck is shifted since the transformation of three-index quantities scales only as $\mathcal{O}(\mathcal{N}^4)$. To obtain all $(ar|bs)_{\text{RI}}$ required in eqn. (2.8), $\mathcal{O}(n_{\text{occ}}^2 (N - n_{\text{occ}})^2 N_{\text{aux}})$ floating point operations are necessary for the matrix–matrix multiplication of computationally cheap three-index intermediates stored beforehand. Though with a much smaller prefactor this retains the formal $\mathcal{O}(\mathcal{N}^5)$ scaling behaviour. Compared to harddisk based orbital transformations done in conventional MP2 calculations mass storage requirements are significantly reduced within the RI scheme, and almost peak performance during the matrix–matrix multiplication can be achieved. The time determining steps of RI-MP2 calculations can be efficiently parallelised over pairs of occupied orbitals since they are involved in all $\mathcal{O}(\mathcal{N}^5)$ scaling steps. This has been implemented in a recent version of the TURBOMOLE 'ricc2' module (see ref. [213] for details) which is employed in the present work to perform parallel RI-MP2 energy calculations for system sizes as large as $N = 4800$ and $N_{\text{aux}} = 10861$ basis

[21] This requires $N_{\text{aux}} < N^2$. Depending on which types of integrals are fitted and on the size N of the basis set, chosing $1.5N \leq N_{\text{aux}} \leq 4N$ both a sufficient accuracy and high efficiency can be achieved.

functions.[22,23] The computationally most demanding part of RI-MP2 gradient calculations is to solve the Z-vector equation [214].

Another advantage of RI-MP2 over exact MP2 is the scaling behaviour upon an increase of the basis set size N for a given system. Keeping the number of active occupied orbitals n_{occ} fixed the operation count scales like $\mathcal{O}(N^4)$ for MP2 and like $\mathcal{O}(N^3)$ for RI-MP2. For this reason RI-MP2 is most efficient for large N, making the RI approximation well suited for MP2 basis set extrapolation studies (see next section).

The application of MP2, in general, is computationally more expensive than, *e. g.*, standard DFT. Besides the RI approximation, local approaches (Werner *et al.* [198, 215], Head-Gordon *et al.* [216]), Laplace-transform techniques (Almlöf, Häser, Scuseria *et al.* [217]) as well as efficient parallel implementations of RI-MP2 (Hättig *et al.* [213]) and conventional MP2 using advanced integral transformation algorithms (Pulay *et al.* [218]) have been developed to reduce MP2 computational times. However, they still do not allow studies of systems as large as in the field of heterogeneous catalysis. Implementations of periodic boundary conditions are in progress, but applications to systems with only a few atoms in the unit cell or with periodicity in less than three dimensions have been reported [219–221].

2.2.2 Extrapolation to the MP2 CBS Limit

When employing finite (*i. e.*, incomplete) auxiliary basis sets in RI-MP2 calculations, errors in computed correlation energies are inevitable. As long as these errors are negligible compared to the error due to an incomplete one-electron basis set [211] extrapolation schemes can be applied to estimate CBS limits. To assess this point MP2(fc) calculations of the water binding energy in the 2T zeolite cluster model are repeated within the RI approach,[24] employing suitable auxiliary basis sets optimised by Weigend and Hättig [211, 212]. Results obtained for uncorrected and counterpoise corrected binding energies, ΔE and ΔE^{cp}, and respective correlation energy contributions, ΔE_{MP2} and $\Delta E^{\mathrm{cp}}_{\mathrm{MP2}}$, are summarised in

[22] '25T' zeolite cluster model (139 atoms) and aug(O)-TZVPP basis set; see Chapter 4 for details

[23] taking 56 hours wall-clock time on two 32-CPU IBM p690 nodes

[24] using the TURBOMOLE code [151, 203]

Tab. 2.4. Direct comparison can be made to conventional MP2 results (Tab. 2.3). MP2 binding energy differences between conventional and RI results are 0.01 kJ/mol on average, 0.03 kJ/mol at most. Thus, the RI error is about two orders of magnitude smaller than the error from an incomplete basis set and one order of magnitude smaller than the error due to the frozen core approximation. This observation justifies CBS limit extrapolations of RI-MP2 water binding correlation energy contributions. In this work the inverse power formula proposed by Helgaker *et al.* [222],

$$E_{\text{correl.}}(X) = a + bX^{-3} \quad , \tag{2.14}$$

or, equivalently,

$$a = E^{\infty}_{\text{correl.}} = \frac{X_1^3 E_{\text{correl.}}(X_1) - X_2^3 E_{\text{correl.}}(X_2)}{X_1^3 - X_2^3} \quad , \tag{2.15}$$

is employed. Among other extrapolation schemes this one proved most effective (see also refs. [223–225] and references therein for recent discussions on this topic). Due to the linearity in a and b these equations can also be applied to correlation energy differences $\Delta E_{\text{correl.}}$ (*e. g.*, ΔE_{MP2}) instead of total energies $E_{\text{correl.}}$. For weakly bound systems the question arises whether uncorrected or counterpoise corrected energies should be used for extrapolation. This question is answered when considering that the inverse power extrapolation scheme by construction accounts only for the incomplete description of the electronic Coulomb cusp, *i. e.*, for the basis set incompleteness error (BSIE). Consequently, to avoid BSSE-contaminated results energies corrected for the basis set superposition error should be used consistently for CBS limit extrapolations. This is illustrated in the last columns of Tab. 2.4 showing different CBS limits for the RI-MP2 water binding correlation energy contribution, $\Delta E^{\infty}_{\text{MP2}}$ and $\Delta E^{\text{cp},\infty}_{\text{MP2}}$, obtained from extrapolation of uncorrected and BSSE corrected results, respectively.[25] Results for $\Delta E^{\text{cp},\infty}_{\text{MP2}}$ (17.0 – 19.0 kJ/mol) cover an interval more narrow than that for $\Delta E^{\infty}_{\text{MP2}}$ (17.6 – 23.4 kJ/mol). For reasons explained above the latter show worse convergence, and they also tend to

[25] As already shown in an early study by Woon and Dunning [226], "... one is not constrained to use correlation consistent sets of the same cardinal number on all centers in order to accurately estimate the CBS limits." Since this might allow for savings in computational time without loss in accuracy, results from mixed basis sets are also given in Tab. 2.4, corresponding CBS limits are obtained by using the oxygen basis set cardinal numbers.

Table 2.4: *RI-MP2(fc) single-point calculations for the 2T zeolite cluster model water binding energy using Dunning's basis sets. Uncorrected and counterpoise corrected results, ΔE and ΔE^{cp}, corresponding correlation energy contributions, ΔE_{MP2} and ΔE^{cp}_{MP2}, and 2-point extrapolated CBS limits, ΔE^{∞}_{MP2} and $\Delta E^{cp,\infty}_{MP2}$, are given (in kJ/mol)*

n	H, Al, Si	O	N [a]	ΔE	ΔE^{cp}	ΔE_{MP2}	ΔE^{cp}_{MP2}	f [b]	(n) [c]	ΔE^{∞}_{MP2}	$\Delta E^{cp,\infty}_{MP2}$
1	cc-pVDZ	cc-pVDZ	193	88.0	53.1	21.55	5.89	0.45			
2		cc-pVTZ	321	72.6	57.5	20.52	12.59	0.53			
3		cc-pVQZ	521	67.6	59.5	20.12	15.47	0.57			
4		cc-pV5Z	809	65.6	60.8	19.67	16.73	0.60			
5		aug-cc-pVDZ	265	64.4	54.6	17.74	11.43	0.65			
6		aug-cc-pVTZ	449	66.3	58.9	20.01	15.35	0.64			
7		aug-cc-pVQZ	721	67.1	61.3	21.27	17.10	0.72			
8		aug-cc-pV5Z	1097	66.7	62.2	21.44	17.88	0.79			
9	cc-pVTZ	cc-pVTZ	434	74.5	58.5	22.88	13.74	0.57	(*1*)	23.4	17.0
10		cc-pVQZ	634	68.7	60.6	21.06	16.01	0.63	(*2*)	21.5	18.5
11		cc-pV5Z	922	65.4	61.7	19.94	17.17	0.74	(*3*)	19.7	19.0
12		aug-cc-pVTZ	562	65.3	59.9	20.13	15.75	0.81	(*5*)	21.1	17.6
13		aug-cc-pVQZ	834	65.5	61.6	20.69	17.25	0.90	(*6*)	21.2	18.6
14		aug-cc-pV5Z	1210	66.1	62.4	21.38	17.97	0.92	(*7*)	21.5	18.9
15	cc-pVQZ	cc-pVQZ	828	69.7	61.3	22.53	16.66	0.70	(*9*)	22.3	18.8
16		cc-pV5Z	1116	67.1	62.0	21.98	17.54	0.88	(*10*)	23.0	19.1
17		aug-cc-pVQZ	1028	65.9	61.8	21.21	17.48	0.93	(*12*)	22.0	18.7
18		aug-cc-pV5Z	1404	65.9	62.5	21.42	18.10	0.97	(*13*)	22.2	19.0
19	cc-pV5Z	cc-pV5Z	1413	65.1	62.2	20.13	17.79	0.80	(*15*)	17.6	19.0
20		aug-cc-pV5Z	1701	64.1	62.5	19.70	18.15	0.96	(*17*)	18.1	18.9

[a] total number of contracted spherical basis functions for the adsorption complex; [b] fraction of the MP2 based BSSE on the full BSSE; [c] line n from which the second point is taken for extrapolation (oxygen basis set cardinal numbers are used)

be clearly overestimated. Similar observations were made by Halkier *et al.* [227] for small hydrogen-bonded complexes. The two important findings are that as soon as one of the two extrapolation points is generated with a quadruple-ζ (or better) basis set on oxygen—no matter what basis sets are used for the other elements—the obtained $\Delta E_{\mathrm{MP2}}^{\mathrm{cp},\infty}$ values differ by 0.5 kJ/mol at most from the "best" CBS limit. Additionally, in these cases the effect of diffuse basis functions on oxygen atoms can be neglected since differences in values for $\Delta E_{\mathrm{MP2}}^{\mathrm{cp},\infty}$ obtained with cc-pV*X*Z and aug-cc-pV*X*Z basis sets, respectively, differ by 0.1 kJ/mol only.

Finally, a few remarks on these results are made which might be of use in situations where extrapolations to the CBS limit are not intended or simply not affordable. The numbers in Tab. 2.4 show that the fraction of the MP2 based BSSE on the full (incl. HF) BSSE increases to more than 90 % with growing size of the basis set. This is due to the faster (exponential) CBS limit convergence of the HF energy compared to the correlation energy, also observed by other authors for different hydrogen-bonded complexes (see, *e. g.*, refs. [147, 227–230]). The HF CBS limit is virtually reached (BSSE clearly smaller than 1 kJ/mol) when aug-cc-pVQZ and cc-pVQZ or better basis sets for oxygen and the other elements, respectively, are used. For all basis sets counterpoise corrected HF binding energies are clearly closer to the CBS limit[26] than uncorrected values. This is not the case for MP2-only results, uncorrected values tend to be closer to the CBS limit[27] than those corrected for the BSSE, particularly for very small basis sets. Observations of that kind were also made by other authors [227–229, 231] promoting the idea that uncorrected aug-cc-pVDZ results are reliable in calculations for correlation energy contributions. This, however, is a case of fortuitous cancellation of the BSSE and the BSIE. Due to the opposite sign of BSSE and BSIE in correlated calculations, for larger basis sets the mean value of the uncorrected and counterpoise corrected binding energies may serve as an estimate for the final result. Whenever affordable one set of diffuse functions should be included in the oxygen basis set. This usually reduces the BSSE by a factor of two in a computationally cheaper way than increasing the oxygen basis set cardinal number. A further introduction of diffuse basis functions for the other elements or even of a second set for oxygen ('d-aug-cc-pV*X*Z' [232])

[26] $\Delta E_{\mathrm{HF}} = \Delta E_{\mathrm{HF}}^{\mathrm{cp}} = 44.4$ kJ/mol from largest basis set
[27] $\Delta E_{\mathrm{MP2}}^{\mathrm{cp},\infty} = 18.9$ kJ/mol from largest basis sets

cannot be recommended since it reverses the trend of reducing the BSSE (numbers not included in the present work).

Dunning's series of correlation-consistent basis sets are constructed in a way that all functions making approximately equal contributions to the correlation energy are added at the same time when the cardinal number is increased. This scheme does not necessarily result in basis sets optimised for a given quality level. In cases where extrapolations to the CBS limit are not intended other basis sets than these might be advantageous, *e. g.*, the basis sets developed by Ahlrichs *et al.* [156, 157]. For this reason another series of RI-MP2(fc) calculations[28] for the water binding energy in the 2T zeolite cluster model is performed, see Tab. B.4 (Appendix, page 138). The main observation is that BSSE values obtained here tend to be close to the BSSE with Dunning basis sets of the next higher quality level (Tab.2.4). Additional diffuse basis functions on oxygen atoms are very effective, uncorrected binding energies ΔE show maximum deviations of only +2 kJ/mol from the CBS limit extrapolated before (63.3 kJ/mol).

In this work optimised basis sets developed by Ahlrichs *et al.* will be preferred over the cc-pV*X*Z basis set series for MP2 energy and gradient calculations (*i. e.*, structure optimisations) since the basis set truncation error of the former is smaller for a given number of basis functions. Dunning basis sets, however, will be employed in single-point energy calculations for CBS limit extrapolations.

[28] using the TURBOMOLE code [151, 207] and optimised auxiliary basis sets [210, 212]

Chapter 3

WATER-ASSISTED PROTON JUMPS IN ACIDIC CHABAZITE[1]

3.1 INTRODUCTION

In the first application of the MP2/DFT combination proton jump reactions in the zeolite H-SSZ-13, both loaded with one water molecule per Brønsted site or completely dry, are studied. This type of reaction has already been examined using different approaches [86, 234–242]. Without inclusion of exact exchange DFT calculations underestimate reaction barriers for proton jump reactions. For example, using a 3T cluster model, Auerbach *et al.* [235] report 72.8, 90.2,[2] and 99.1 kJ/mol for the proton jump barrier in the zeolite H-Y when BLYP, B3LYP, and MP2, respectively, are used. Ryder *et al.* [236] investigated a proton jump in the zeolite H-ZSM-5 employing a 5T cluster model and found energy barriers of 85.8, 108.4, and 135.1 kJ/mol (BPW91, B3LYP, BH&HLYP, respectively). For water assisted proton jumps the cluster model study by Krossner and Sauer [238] yielded 8.1 and 16.4 kJ/mol (BP86, MP2, respectively) for the energy barrier. Zygmunt *et al.* [239] estimated this barrier for H-ZSM-5 from HF and MP2 calculations on cluster models of different size and obtained a similar value of 22.1 kJ/mol. These examples illustrate the need of at least local improvements over GGA type density functionals in studies of proton jump barriers.

[1] based on ref. [233]

[2] In a more recent study, Auerbach *et al.* [242] show that with increasing size of the cluster model the B3LYP value converges to 135 ± 5 kJ/mol.

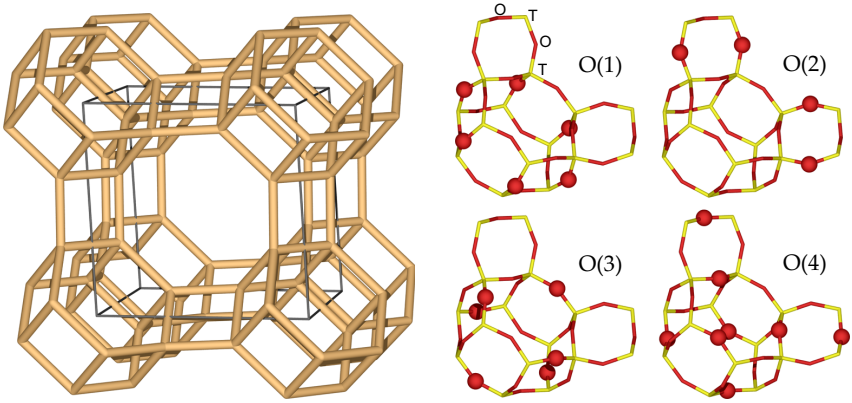

Figure 3.1: *T-atom framework (left panel) and crystallographic oxygen atom sites O(1) – O(4) of all-silica (T = Si) chabazite (right panel)*

3.2 Models and Methods

Chabazite. The T-atom framework of the natural zeolite chabazite (see ref. [243] and references therein) consists of hexagonal prisms centred at the corners of periodically repeating rhombohedra as shown on the left panel in Fig. 3.1. The unit cell contents of dry all-silica chabazite has the stoichiometry $Si_{12}O_{24}$. All silicon atoms are equivalent by symmetry, and the oxygen atoms occupy four crystallographically different sites O(1) – O(4) as shown in the right panel of Fig. 3.1 (space group no. 166, $R\bar{3}m$). The high-silica Brønsted acid form of chabazite, H-SSZ-13 (*cf.* refs. [244–246] for its preparation), is obtained by replacement of a silicon atom by aluminium and addition of a charge compensating proton forming a bridging OH-group between silicon and aluminium atoms (space group no. 1, $P1$). The energetically most stable configuration is given with the proton bound to an O(1) oxygen atom (see Section 2.1.1) which is confirmed in many studies using a number of different approaches [86, 237, 246–257]. Unit cell parameters of this structure are determined from constant pressure ion-pair shell-model potential [258] calculations [86] ($a = 945.3$ pm, $b = 938.7$ pm, $c = 944.1$ pm, $\alpha = 94.0°$, $\beta = 95.4°$, and $\gamma = 94.8°$). In subsequent calculations on H-SSZ-13 these cell parameters are kept constant.

Cluster Model. The cluster model for the embedding calculations, indicated in Fig. 3.2, consists of three tetrahedral corner-sharing $T[O_{1/2}]_4$ units (denoted '3T'). It contains eight hydrogen atoms added to saturate dangling bonds of the inner part. Corresponding link atom bond lengths TO – H (T = {Al, Si}) are set according to the values listed in Tab. B.1. In the QM-Pot approach these distances are kept at fixed values, *cf.* eqn. (1.9), and they do not change upon structure relaxation.

DFT. The PBE functional (Perdew, Burke, and Ernzerhof, [126]) is employed in connection with a computational efficient Padé form for exchange and correlation [159] as the low-level method in the embedding calculations. For all elements in the system norm-conserving pseudopotentials are used (Troullier and Martins [140], see Tab. B.2). The plane wave basis set kinetic energy cut-off is 70 Ry in a first series of calculations. This value is commonly used in plane wave DFT studies on condensed (aqueous) or gas-phase systems with this type of pseudopotential (see *e. g.*, refs. [25, 93, 98, 259–264]). As demonstrated in Section 2.1.1 a much higher cut-off than 70 Ry is required to obtain converged energies for systems containing oxygen as the 'hardest' element. For this reason calculations employing 100 Ry are also performed.

The 3T cluster model is treated as an isolated (gas-phase) system, that is, without periodic boundary conditions in plane wave DFT calculations. Due to its size—the maximum distance between two atoms is about 9 Å—a computational box bigger than the unit cell of H-SSZ-13 is required. This means that the basis sets for the periodic system and the cluster model include different numbers of plane waves, see eqn. (2.3). However, as shown in Section 2.1.1, the quality of a plane wave basis set is determined by its kinetic energy cut-off value. Different numbers of plane waves resulting from cells of different volume leave the basis set quality unchanged. For the 3T cluster model convergence in the total energy is achieved with computational boxes bigger than 12 Å. Under this condition total energy fluctuations due to different numbers of plane waves per volume (*cf.* Section 2.1.1) are about 1.5 and 0.2 mE_h at 70 and 100 Ry cut-off, respectively. This error can be neglected in the context of the embedding calculations. Cubic computational boxes with a length of 14 Å for the cluster model and of 10 Å for the water molecule are used. Periodic images are decoupled in either case (see note 2 on page 15).

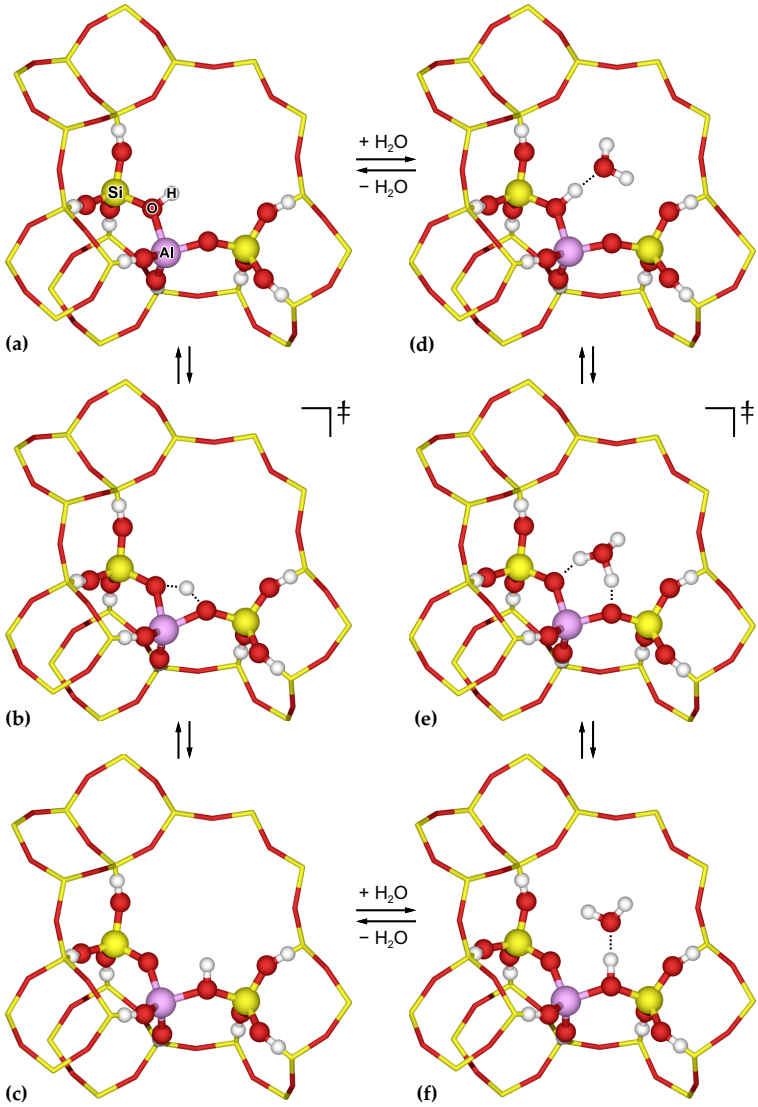

Figure 3.2: *Proton jump reactions in dry zeolite H-SSZ-13 (**a**-**b**-**c**) and in the presence of a water molecule (**d**-**e**-**f**). The 3T cluster model used for embedding is highlighted*

MP2. In the high-level part of the embedding calculations second-order Møller–Plesset perturbation theory is applied. Ahlrichs' T(O)DZP Gaussian basis sets (see footnote 18 on page 34) are employed for the 3T cluster model in a first series of calculations including all electrons in the correlation scheme. This basis set can be regarded rather small for MP2 calculations. Higher angular momentum functions are necessary to achieve reasonable MP2 results, and diffuse functions are needed to reduce the basis set superposition error (BSSE). The basis set convergence study in Section 2.2.2 is of great use to make a decent choice for a basis set yielding reliable MP2 results at affordable computational cost. The values for the water binding energies in Tab. 2.4 show that MP2 results converge very slowly to their CBS limit. When cc-pVTZ (H, Al, Si) and aug-cc-pVQZ (O) basis sets ($\Delta E^{\mathrm{cp}}_{\mathrm{MP2}} = 17.25$ kJ/mol) are used 91 % of the CBS limit ($\Delta E^{\mathrm{cp},\infty}_{\mathrm{MP2}} = 18.9$ kJ/mol) are recovered. Further improvement is only possible by substantial enlargement of the basis set causing an unacceptably high cost–benefit relation. Hence, this Dunning basis set combination is applied for the 3T cluster model in a second series of embedding calculations. Due to the large number of basis functions (up to 1136) approximations using the resolution of the identity (RI) approach and a frozen core[3] are employed, see Section 2.2.1.

QM-Pot. Using the QMPOT program [86] geometry optimisations[4] are carried out at the combined MP2/DFT level. The TURBOMOLE [151, 174, 203] and CPMD codes [104] are driven by QMPOT interface functions to perform the high-level (MP2) and low-level (DFT) calculations, respectively. In regard to the issues considered before two different basis set combinations are employed. Ahlrichs' Gaussian basis sets (T(O)DZP) for MP2 and 70 Ry kinetic energy cut-off for plane wave DFT calculations, henceforth labelled 'A', as well as Dunning's Gaussian basis sets (aug-cc-pVQZ (O), cc-pVTZ (H, Al, Si)) for RI-MP2 and 100 Ry kinetic energy cut-off for DFT, denoted 'B', are chosen. Numerical force constant calculations are performed[5] to characterise stationary points found and to obtain zero-point vibrational energy (ZPVE) contributions (MP2/DFT,

[3] electrons in molecular orbitals corresponding to oxygen 1*s*, aluminium 1*s*, and silicon 1*s* atomic orbitals are excluded from the MP2 correlation scheme

[4] max. component of the Cartesian gradient $1{*}10^{-4}\ E_{\mathrm{h}}/a_0$

[5] atom displacements $\pm 0.01\ a_0$, translational modes projected from the Hessian matrix

Table 3.1: *Selected atomic distances (in pm) for structures* ***a*** *–* ***f*** *(see Fig. 3.2) calculated with the hybrid MP2/DFT scheme (basis set A, basis set B). Values in parentheses are plain DFT results (70 Ry, 100 Ry)*

	reactant	transition structure	product
dry	(**a**)	(**b**)	(**c**)
$r_{O(1)-H}$	97.4, 96.6 (97.8, 97.3)	123.4, 123.7 (124.1, 124.4)	
$r_{O(2)-H}$		125.1, 125.3 (127.2, 127.0)	97.6, 96.9 (98.1, 97.6)
hydrated	(**d**)	(**e**)	(**f**)
$r_{O(1)-H}$	103.7, 102.1 (105.7, 104.6)	148.6, 151.9 (150.8, 147.1)	
$r_{O(1)\cdots OH_2}$	251.7, 253.1 (254.5, 254.0)	246.2, 247.2 (249.7, 246.9)	
$r_{O(2)\cdots OH_2}$		241.7, 242.3 (244.5, 244.0)	250.5, 251.1 (251.3, 250.8)
$r_{O(2)-H}$		134.9, 136.9 (134.3, 135.9)	104.9, 103.6 (107.6, 106.5)

basis set A). Plain DFT calculations (CPMD) are carried out for comparison (PBE, 70 and 100 Ry cut-off). Water binding energy calculations include counterpoise corrections for the BSSE [91] in the high-level part.

3.3 Results and Discussion

For the proton jumps between oxygen sites O(1) and O(2) both minimum structures with the proton bound either to O(1) or O(2) and the corresponding transition structures are located. This is done using the combined MP2/DFT scheme and plain DFT (PBE) for comparison. Both the dry zeolite and the adsorption complex with water are considered. Table 3.1 lists selected atomic distances in the reactants, transition structures, and products. In hybrid MP2/DFT calculations smaller O – H bond

Table 3.2: *H-SSZ-13 water molecule binding energies for different proton sites (in kJ/mol). Values in parentheses are corrected for the BSSE*

method	$H_2O\cdots H-O(1)$	$H_2O\cdots H-O(2)$
DFT-only (70 Ry)	78	73
DFT-only (100 Ry)	75	71
MP2/DFT (basis set A)	86 (71)	81 (63)
MP2/DFT (basis set B)	82 (76)	77 (72)

lengths in the reactants and products compared to the plain DFT (PBE) results are obtained. The distance between the water molecule and the acidic site is reduced as well.

DFT-only (70 Ry, 100 Ry) and MP2/DFT (basis set A) calculations yield imaginary frequencies for the transition structures at 1274i, 1202i, and 1304i cm^{-1}, respectively, for the dry zeolite (Fig. 3.2, **b**), and at 251i, 283i, and 229i cm^{-1}, respectively, for the hydrated system (Fig. 3.2, **e**).

Table 3.2 summarises the binding energies of the water molecule to the two investigated acidic sites in H-SSZ-13. Plain DFT results (100 Ry) differ from the counterpoise corrected MP2/DFT (basis set B) results by less than 1 kJ/mol. This is a result of partial error cancellation since the GGA tends to overestimate hydrogen bonding and also cannot properly account for dispersion interactions. For basis set A the BSSE is about three times bigger than for basis set B. This is already expected from the basis set convergence study presented in Section 2.2.2. The latter can also be used to make a final estimate for the MP2/DFT water binding energy. It is assumed that the fraction of the CBS MP2 correlation energy limit recovered with the Dunning basis set combination (B) is the same for both the 2T cluster model in Section 2.2.2 and for the present 3T cluster model. Counterpoise corrected contributions of the MP2 correlation energy to the binding energy are 27.0 and 32.3 kJ/mol for water adsorbed at the H-O(1) and H-O(2) sites, respectively. Associating these numbers with 91 % of the corresponding CBS limits the latter result in 29.6 and 35.5 kJ/mol. Furthermore, 0.5 kJ/mol are added to account for the frozen core approximation (see Section 2.2.1, page 37). HF contributions are not corrected since they are converged to CBS limits within less than 1 kJ/mol.

Table 3.3: *Barriers and reaction energies, $\Delta E^{\ddagger}$ and ΔE, for H-SSZ-13 proton jumps from oxygen site O(1) to site O(2). Values in parentheses are ZPE corrected (all numbers in kJ/mol)*

	dry		*hydrated*	
method	$\Delta E^{\ddagger}$	ΔE	$\Delta E^{\ddagger}$	ΔE
DFT-only (70 Ry)	65 (54)	10 (11)	20 (16)	14 (14)
DFT-only (100 Ry)	68 (54)	11 (11)	22 (18)	15 (16)
MP2/DFT (basis set A)	71 (55)	11 (6)	26 (16)	16 (9)
MP2(*C*)	53	−8	23	10
DFT(*S*)−DFT(*C*)	18	19	3	6
DFT(*S*)	66	10	20	13
MP2(*C*)−DFT(*C*)	5	1	6	3
MP2/DFT (basis set B) [a]	81 (65)	13 (8)	30 (20)	17 (10)
MP2(*C*)	64	0	27	11
DFT(*S*)−DFT(*C*)	17	13	3	6
DFT(*S*)	68	10	22	14
MP2(*C*)−DFT(*C*)	13	3	8	3

[a] ZPE corrections taken from calculations with basis set A

Thus, 80 and 75 kJ/mol are obtained as best estimates for the MP2/DFT binding energies of water at the H-O(1) and H-O(2) sites in H-SSZ-13, respectively. To the author's knowledge these are the most accurate water binding energies calculated for zeolites so far.[6] After adding zero-point vibrational and thermal corrections, the predicted heats of adsorption ΔH(298 K) are 75 and 71 kJ/mol, respectively. Experimental estimates are rather uncertain and range from 51 to 85 kJ/mol (Tab. 26 in ref. [266]).

Table 3.3 shows results for the energy barriers, $\Delta E^{\ddagger}$, and reaction energies, ΔE, of the proton jump reactions. Going from 70 to 100 Ry cut-off in the plain DFT calculations does not change energy differences by more than 3 kJ/mol. Comparison with the combined MP2/DFT results

[6] In a recent study [265] full periodic B3LYP calculations using a polarised double-ζ basis set yielded 110 and 84 kJ/mol for uncorrected and BSSE corrected water binding energies at the H−O(1) site in H-SSZ-13.

confirms the expected underestimation of reaction barriers by the GGA type density functional (PBE). Using basis set A the barriers increase by 6 kJ/mol compared to the DFT-only result (70 Ry). The qualitatively better basis set B yields even larger differences (8 – 13 kJ/mol) to the 100 Ry plain DFT results. These are significant changes (*e. g.*, increase of up to 36 % for the hydrated zeolite) which become important when predictions for rates of such processes are made (see below). A small increase of only 1 – 2 kJ/mol is also observed in the reaction energies calculated using the hybrid MP2/DFT approach but this is assigned to cancellation effects since reactants and products are very similar.

Within the applied embedding scheme contributions to the total energy $E(S, L)$ can, in general, be analysed in two different ways, that is

$$E(S,L) = E(C)_{\text{high}} + \Big(E(S)_{\text{low}} - E(C)_{\text{low}}\Big) \tag{3.1}$$

and

$$E(S,L) = \Big(E(C)_{\text{high}} - E(C)_{\text{low}}\Big) + E(S)_{\text{low}} \quad . \tag{3.2}$$

Corresponding numbers for these terms are included in Tab. 3.3. In the first interpretation (eqn. (3.1)) one starts from the MP2 value for the 3T cluster model calculated at the structure obtained with the combined MP2/DFT approach, 'MP2(C)'. A long-range correction term, defined as the DFT energy difference between the total system and the cluster model, 'DFT(S)–DFT(C)', is added. This term is expected to become smaller with growing size of the cluster model. For the proton jump in dry H-SSZ-13 the long-range correction raises the barrier significantly compared to the MP2 cluster model result, and for the reaction energy it can even change the sign. Although being constrained to the geometry of the periodic solid, the 3T model itself is too small to yield reliable results. For hydrated H-SSZ-13 the effect of long-range corrections is smaller (but still important) for two reasons. First, the additional water molecule increases the size of the cluster model, and second, it attenuates the deformation of the entire zeolite lattice during the proton jump. In the second interpretation (eqn. (3.2)) the DFT result for the complete periodic system at the structure obtained with the combined method, 'DFT(S)', is given. Corresponding values agree within 1 kJ/mol to the results of plain DFT calculations showing that structures do not change much

upon switching to the hybrid MP2/DFT approach. The correction term, 'MP2(*C*)–DFT(*C*)', represents the local MP2 correction to the full periodic DFT result. As expected, this correction clearly increases the barriers.

Sierka and Sauer [86] used the B3LYP hybrid functional in full periodic single-point calculations. For the energy barrier, $\Delta E^{\ddagger}$, and the reaction energy, ΔE, they report values of 72 and 12 kJ/mol, respectively (dry zeolite). This is an improvement compared to the PBE results obtained here and in good agreement to the MP2/DFT (basis set A) results. Their value for the barrier, however, is still underestimated compared to the MP2/DFT (basis set B) result of 81 kJ/mol. Employing a small 1T cluster model, Sierka and Sauer [237] also introduced coupled-cluster (CCSD(T)) corrections to their B3LYP results which raise the proton jump barrier by 13 kJ/mol. This correction includes an MP2 part of 8 kJ/mol,[7] and it is concluded that CCSD(T) corrections to MP2/DFT results may increase the proton jump barrier by another 5 kJ/mol (dry zeolite).

As also shown in Tab. 3.3 zero-point vibrational energies reduce energy barriers by 11 – 14 kJ/mol for the dry zeolite and by 4 kJ/mol in the water assisted proton jump (plain DFT calculations). Employing the hybrid MP2/DFT (basis set A) approach values of 16 and 10 kJ/mol, respectively, are obtained. This suggests that ZPE corrected energy barriers are less different than uncorrected energy barriers (plain DFT *vs.* MP2/DFT).

To illustrate the importance of reliable predictions of energy barriers for the kinetics of proton jump reactions, rate constants are calculated according to classical transition state theory (see Tab. 3.4). Using a cluster model for the zeolite H-ZSM-5, Ryder *et al.* [236] showed that the presence of water significantly lowers the energy barrier and therefore increases the rate for proton jumps compared to dry systems. For H-SSZ-13 differences of about eight orders of magnitude are obtained between the rate constants for the dry and the hydrated zeolite at room temperature. In a DFT molecular dynamics simulation of water in the zeolite gmelinite [234] spontaneous proton transfer is observed after 1.2 ps. The characteristic time for the reverse proton jump in hydrated H-SSZ-13, calculated as reciprocal rate constant from the present data, is also about 1.2 ps (plain DFT, 100 Ry; see Tab. 3.4). However, improving the potential energy surface by hybrid MP2/DFT embedding may change rate constants and, hence, characteristic times by up to two orders of magnitude.

[7] private communication with the authors

Table 3.4: *Rate constants (per site) in s^{-1} at different temperatures for proton jump reactions from oxygen site O(1) to O(2) in H-SSZ-13 for the dry zeolite and in presence of one water molecule*

	forward		*reverse*	
	dry	*hydrated*	*dry*	*hydrated*
DFT-only (100 Ry)				
298 K	$2 * 10^3$	$7 * 10^8$	$2 * 10^5$	$8 * 10^{11}$
400 K	$5 * 10^5$	$3 * 10^9$	$2 * 10^7$	$9 * 10^{11}$
500 K	$2 * 10^7$	$9 * 10^9$	$3 * 10^8$	$9 * 10^{11}$
MP2/DFT (basis set B)[a]				
298 K	$4 * 10^1$	$3 * 10^9$	$9 * 10^2$	$5 * 10^9$
400 K	$4 * 10^4$	$3 * 10^{10}$	$3 * 10^5$	$1 * 10^{10}$
500 K	$2 * 10^6$	$1 * 10^{11}$	$1 * 10^7$	$2 * 10^{10}$

[a] partition functions required for the calculation of the rate constants are taken from calculations with basis set A

3.4 Conclusion

The applied hybrid QM/QM approach improves DFT potential energy surfaces of extended systems locally, *e. g.*, at reaction sites, by embedding of an MP2 correction. Particularly in situations where the GGA approach in DFT fails to make reliable predictions the combined MP2/DFT method proves to be a useful tool. In addition to proton jump reactions studied here the hybrid approach can also be employed to calculate van der Waals contributions for the binding of small molecules to surfaces (see, *e. g.*, ref. [267]) and for biomolecules. Extension beyond MP2 is possible when plane wave DFT codes are combined with codes for CCSD(T) gradients. Since such structure optimisations can be prohibitive it is advised that at least single-point calculations, if possible, are considered to assess the quality of the MP2/DFT results obtained. Another issue left for further investigation is the cluster model size required to obtain converged results in MP2/DFT embedding calculations. These two points will be addressed in the next chapter.

Chapter 4

PROTONATION REACTIONS OF ISOBUTENE IN ACIDIC FERRIERITE[1]

4.1 INTRODUCTION

Acid zeolite catalysts are industrially used for a variety of hydrocarbon transformation processes. Initially it has been assumed that these reactions follow mechanisms known from superacidic media and involve carbocations as intermediates formed on protonation of hydrocarbons by Brønsted acid sites [270, 271]. However, NMR studies failed to find simple carbenium ions as intermediates [272, 273], but rather produced evidence for surface alkoxides [274–277]. Around the same time, quantum chemistry calculations employing small cluster models also reached the conclusion that alkoxides are minima on the potential energy surface (PES) and, hence, intermediates, while carbenium ions represent saddle points on the PES and are only present as extremely short-lived transition structures [278–282]. So far, evidence for persistent carbenium ions in zeolites has been produced only for alkenyl or aromatic based carbenium ions by NMR [283], UV-Vis [284–286], IR [287, 288], or computational [289–291] techniques.

Among carbenium ions derived from small alkenes, the *tert*-butyl cation has attracted much interest because it is more stable than primary or secondary carbenium ions. In the 1960s, Olah *et al.* were the first to generate and describe the *tert*-butyl carbenium ion in superacidic media by means of NMR and vibrational spectroscopy (see refs. [292, 293] and literature cited therein). Stable salts containing the *tert*-butyl carbenium

[1] based on refs. [268, 269]

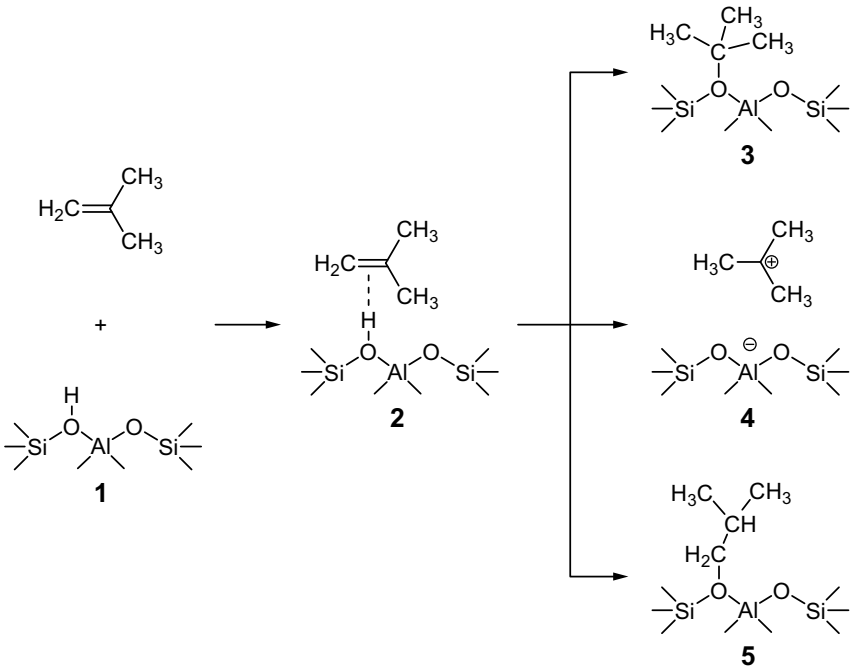

Figure 4.1: *Isobutene adsorption and protonation reactions in Brønsted acid zeolites. Formation of the π-complex **2**, the tert-butoxide **3**, the tert-butyl carbenium ion **4**, and the isobutoxide **5** structures considered in this work*

ion have been synthesised during the last years and characterised by X-ray structure analysis [294, 295]. Carbenium ions might also be stabilised in the micropores of zeolites when the competing formation of an alkoxide is sterically hindered. This issue is addressed in the present chapter by considering different protonation reactions for isobutene adsorbed at a zeolite Brønsted acid site, see Fig. 4.1. Previous computational studies have indeed shown that, depending on the framework and the position at the zeolite wall to which they are bound, the *tert*-butoxide **3** may be as unstable as the *tert*-butyl carbenium ion structure **4** [291, 296–299]. Only the embedded cluster study of Boronat *et al.* [291] reports a local minimum on the PES for the *tert*-butyl carbenium ion in mordenite. It is, however, about 26 kJ/mol less stable than the adsorption π-complex **2**

of isobutene with the Brønsted acid site. Nevertheless, all experimental attempts to detect the *tert*-butyl carbenium ion in various zeolites have been unsuccessful so far, supplying evidence only for the formation of persistent *tert*-butoxides or alkoxides of isobutene oligomers [274, 276, 277, 300–303]. The existence of *tert*-butyl carbenium ions in zeolites remains controversial.

In recent years DFT became the most popular method in computational chemistry to describe zeolites and to model elementary steps of zeolite catalysed chemical processes, *e. g.*, hydrocarbon reactions. Examples of such studies employing periodic boundary conditions (PBC) can be found in the recent review by Hafner *et al.* [304]. It is known, however, that routinely employed density functionals cannot properly account for the longe-range part of dispersion (see Chapter 2, Section 2.1.3), limiting the use of DFT in applications that involve non-bonded interactions between the hydrocarbon part and the zeolite framework. Electron correlation is the origin of dispersion, and the simplest quantum mechanical (QM) method to account for this effect is second-order Møller–Plesset perturbation theory (MP2). There have been previous attempts to use MP2 for such problems either within hybrid QM/MM calculations [296] or as single-point calculations [298]. These calculations were far from being converged, neither with respect to the basis set nor to the cluster model size. Unfortunately, MP2 calculations on zeolites employing PBC will not be feasible in the near future (see Chapter 2, Section 2.2).

Another workaround proposed for this DFT related problem is to add a damped dispersion term calculated from atom–atom C_6 contributions [33–37]. Given the availability of corresponding model parameters this empirical approach can easily be applied to large systems including PBC. In the present chapter advantage is taken of both MP2 and the empirical approach, that is, hybrid MP2/DFT calculations on embedded cluster models of increasing size are carried out to parametrise a damped dispersion term. The model potentials obtained are applied to structures under PBC to estimate periodic MP2 results.

Further, the adequacy of MP2 for a reliable description of the systems investigated in this chapter is verified. To this end, coupled-cluster reaction energy calculations on small zeolite models are performed including single, double, and perturbatively treated connected triple excitations (CCSD(T)) [305].

4.2 Models and Methods

Ferrierite. The Brønsted acid form of a zeolite is obtained from the all-silica porous framework by substitution of a silicon atom by an aluminium atom and addition of a charge compensating proton to the $Al[O_{1/2}]_4$ tetrahedron forming a bridging OH-group. The unit cell of purely siliceous ferrierite is orthorhombic and has the composition $Si_{36}O_{72}$. Low and high temperature phases of this material are known from experiment. Corresponding space groups, however, are not clearly determined yet (see ref. [306] and literature cited therein). The framework of ferrierite shows straight pores of different sizes. 10-membered ring (10-MR) pores separated from each other extend along cell parameter *c*, fully intersected by 8-MR pores parallel to cell parameter *b*, see Fig. 4.2. To avoid couplings between periodic images of the hydrocarbon reaction site, the simulation cell is constructed by doubling the length of the smallest cell vector (*c*). Then, only one silicon atom is substituted by an aluminium atom yielding the simulation cell stoichiometry $HAlSi_{71}O_{144}$ for Brønsted acid ferrierite (H-FER). There are several crystallographic Si positions into which Al can be substituted, and for each position there are four oxygen sites to which the proton can be attached. Unfortunately, a preferred Al position is not known from experiment. Recent studies employing X-ray diffraction, neutron diffraction, IR, or solid-state NMR techniques suggest various distribution patterns for aluminium atoms and Brønsted acid sites in ferrierite [307–310]. In this work the aluminium atom is introduced at position T(2) in accordance with the choice of Nieminen *et al.* [311] (see ref. [312] for the framework atom numbering). The neighbouring oxygen atom O(7) forms the bridging OH-group which points into the intersection of the 8-MR and 10-MR pores, see Fig. 4.3. This choice is supported by stability simulations employing molecular mechanics [313] or semiempirical methods [314]. Experimental studies also reached the conclusion that only protons located in 10-MR pores show catalytic activity in the skeletal isomerisation of linear butenes to isobutene (see refs. [315–318] and references therein).

Cluster Model. The H-FER cluster model used in embedding calculations represents the intersection of 8-MR and 10-MR pores including the Brønsted acid site (see Fig. 4.3). It contains 47 framework atoms, 16 of

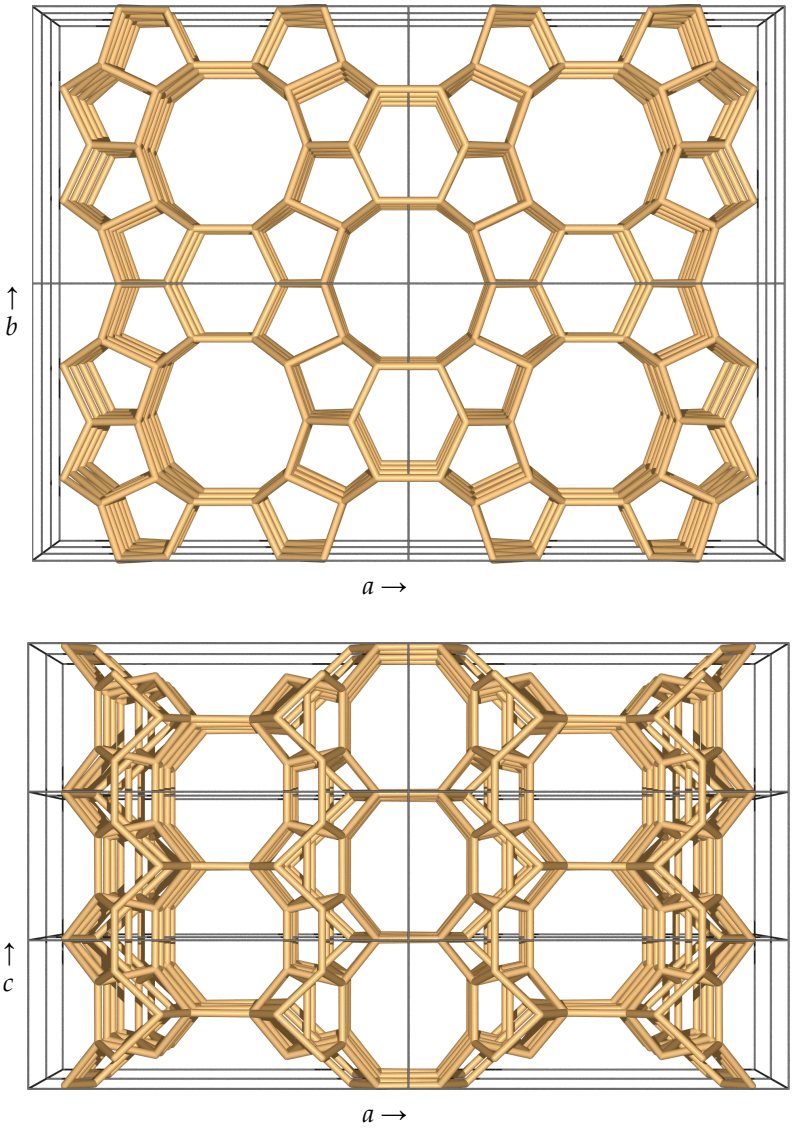

Figure 4.2: *2 x 2 x 3 unit cells of the T-atom framework of all-silica (T = Si) ferrierite. Views along cell parameter c (upper panel) and b (lower panel)*

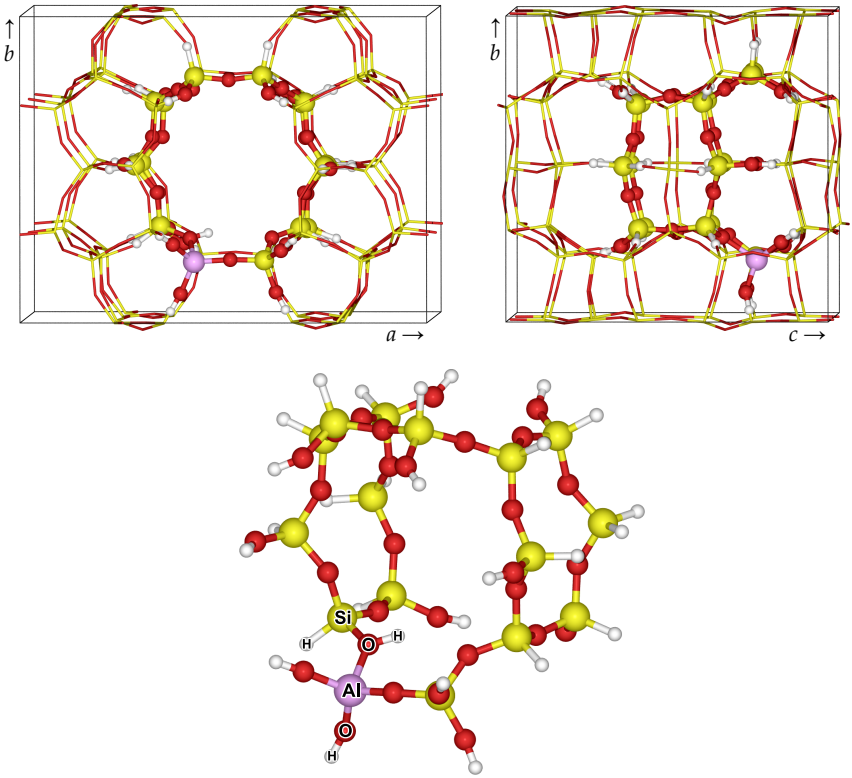

Figure 4.3: *H-FER simulation cell and the embedded $16T_{16H}$ cluster model*

them representing T-atoms ($H_{29}AlSi_{15}O_{30}$). To saturate all dangling bonds 28 link atoms (hydrogen) are added to the cluster model. This results in 12 TO – H and 16 T – H terminations of the cluster model, subsequently denoted "$16T_{16H}$". All link atom bond lengths are set according to the values listed in Tab. B.1 (Appendix, page 135).

DFT. Unless specified otherwise all DFT calculations in this chapter employ the Perdew, Burke, and Ernzerhof (PBE) [126] gradient corrected exchange–correlation functional combined with a computationally efficient Padé expression in the LDA part [159]. The PBE functional is known

to reproduce some dispersion at least for short interatomic distances (see Chapter 2, Section 2.1.3). To contrast this PBE feature to functionals containing Becke's exchange gradient correction, the BP86 functional (Becke [153], Perdew [154]) is also used in a few examples.

Pseudopotentials replace the electronic core of all atoms and facilitate a plane wave expansion of the valence orbitals. To allow for a small plane wave basis set kinetic energy cut-off (30 Ry) a combination of ultrasoft and soft norm-conserving atomic pseudopotentials (Vdb and BHS, see Tab. B.2) is employed. In this chapter this constitutes the standard set-up for plane wave DFT calculations.[2] Only for special purposes norm-conserving pseudopotentials (TM, see Tab. B.2) are used for all atoms combined with a high plane wave basis set cut-off value (110 Ry).

In a first series of DFT calculations the H-FER unit cell parameters are taken from the work by Nieminen *et al.* [311]. Corresponding values ($a = 1870.0$ pm, $b = 1416.8$ pm, $c = 1495.8$ pm, $\alpha = 89.8°$, $\beta = 89.8°$, $\gamma = 90.0°$) are the result of constant pressure cell optimisations employing a shell-model ion-pair potential [258]. In a second series of calculations cell parameters optimised consistently with DFT (PBE) are used obtained for unloaded H-FER **1** by stress tensor calculations within constant pressure optimisation of the simulation cell. Only the parameters α, β, and γ are not relaxed. They are set to 90° since negligible deviations from this value are expected [311]. For technical reasons norm-conserving pseudopotentials (TM, see above) are employed. The penalty function approach proposed by Bernasconi *et al.* [134] is used[3] to simulate a constant basis set cut-off with a constant number of plane waves at variable cell volume. Parameters $a = 1896.6$ pm, $b = 1425.5$ pm, and $c = 1501.5$ pm are obtained[4] for the relaxed orthorhombic simulation cell.

In structure optimisations all atom positions are fully relaxed.[5,6] Stationary points found on the DFT energy surface are characterised by harmonic frequencies obtained from numerical differentiation of forces.[7]

[2] performed with the CPMD code [104]

[3] $A = 400$, $\sigma = 0.4$; *cf.* Chapter 2, Section 2.1.1

[4] stress tensor elements σ_{ii} smaller than 0.2 kbar

[5] max. component of the Cartesian gradient $1*10^{-5}$ E_h/a_0

[6] employing a 10 Å cubic computational box for the isobutene molecule (decoupled periodic images, see note 2 on page 15)

[7] atom displacements ±0.02 a_0, translational modes projected from the Hessian matrix

MP2. Local basis sets constructed from Gaussian functions are used for MP2 calculations on cluster models representing parts of the H-FER framework. Apart from CBS limit extrapolations all MP2 calculations are performed employing Ahlrichs' optimised triple-ζ valence basis set (TZV) [156] combined with different types of augmentation functions. A single set of polarisation functions with exponents 0.8, 0.8, 1.2, 0.3, and 0.35 for hydrogen, carbon, oxygen, aluminium, and silicon atoms, respectively, is added to form the TZVP basis set. The TZVPP basis includes double sets of polarisation functions taken from Dunning's cc-pVTZ basis [155], and aug(O)-TZVPP denotes a combination which, for all oxygen atoms, contains an additional single set of diffuse functions adopted from Dunning's aug-cc-pVTZ basis set [158].

The counterpoise procedure (CP) [91] is applied to correct QM-Pot reaction energy results for the MP2 basis set superposition error (BSSE). Extrapolations to the CBS limit are performed from BSSE corrected reaction energies, ΔE^{cp}. To this end the triple-ζ and quadruple-ζ basis sets from Dunning's correlation-consistent polarised valence series, cc-pVXZ [155], are employed. For the Hartree–Fock (HF) energy contribution to the MP2 reaction energy an exponential extrapolation scheme [319, 320] is chosen,

$$\Delta E^{\mathrm{cp}}_{\mathrm{HF}}(X) = a + b\exp(-cX) \quad , \tag{4.1}$$

whereas an inverse power law [222] is applied for the extrapolation of the correlation energy contribution to the MP2 reaction energy,

$$\Delta E^{\mathrm{cp}}_{\mathrm{MP2(correl.)}}(X) = a + bX^{-3} \quad . \tag{4.2}$$

The nonlinear parameter c in eqn. (4.1) is set to 1.5 [320]. Corresponding CBS limits are calculated directly from 2 data points ($X_1 = 3$, $X_2 = 4$), see eqn. (2.15).

The sizes of the model systems investigated in this work are far too large for conventional MP2 calculations. For this reason the resolution of the identity (RI) approximation is employed combined with a frozen core approach (*cf.* Chapter 2, Section 2.2.1). Electrons in molecular orbitals corresponding to carbon 1s, oxygen 1s, aluminium 1s, and silicon 1s atomic orbitals are excluded from the MP2 correlation scheme. Optimised auxiliary basis sets [210, 211] are used for RI-MP2 energy and gradient calculations employing a recently parallelised version of the TURBOMOLE [151] 'ricc2' module [213, 321].

QM-Pot. Employing the $16T_{16H}$ cluster model shown in Fig. 4.3 hybrid MP2 ("high-level") plane wave DFT ("low-level") structure optimisations under periodic boundary conditions are carried out[8] following the QM-Pot scheme [61, 75, 86] (see Chapter 1, Section 1.2). The energy of the full periodic system, $E(S)_{\mathrm{low}}$, is obtained with DFT (see above).[9] RI-MP2 and DFT are used for cluster model calculations of $E(C)_{\mathrm{high}}$ and $E(C)_{\mathrm{low}}$, respectively. *Via* its interface functions QMPOT operates the CPMD and TURBOMOLE program packages for DFT and RI-MP2 calculations, respectively, of energies and gradients. In the MP2 part TZVPP basis sets are applied for carbon atoms and for those oxygen atoms which connect two cluster model T-atoms (T – O – T). For all other atoms TZVP basis sets are chosen. The resulting basis set combination is denoted TZVP(P).

In DFT calculations the $16T_{16H}$ cluster model is put into the centre of a cubic computational box. Its length of 25 Å ensures that the electron density is virtually zero at the cell border; periodic images are decoupled (see note 2 on page 15). To employ a plane wave basis set of the same quality as for the full periodic system the corresponding kinetic energy cut-off value is adopted.

Cluster Model Convergence Studies. The computational work in RI-MP2 energy and gradient calculations, in particular its scaling with the system size (*cf.* Chapter 2, Section 2.2.1), does not allow for a further increase of the size of the embedded cluster model in QM-Pot structure optimisations while keeping the same Gaussian basis set quality. To assess the convergence behaviour of hybrid MP2/DFT reaction energies with respect to the size of the embedded cluster, systematic series of RI-MP2 and DFT single-point cluster model reaction energy calculations are performed. Relaxed geometries for periodic structures **1** – **5** available from the first series of plain DFT calculations serve to construct 17 fully TO – H terminated cluster models for each of these systems. They contain the reaction site including the hydrocarbon part and 2 to 29 T-atoms, in total 12 hydrocarbon atoms plus 16 to 145 atoms representing the zeolite framework. Figure 4.4 illustrates the construction principle. DFT calculations on these cluster models are performed as described above.

[8] using the QMPOT code [86]; max. component of the Cartesian gradient $1*10^{-4}\ E_{\mathrm{h}}/a_0$

[9] PBE functional; Vdb and BHS pseudopotentials, 30 Ry plane wave basis set cut-off

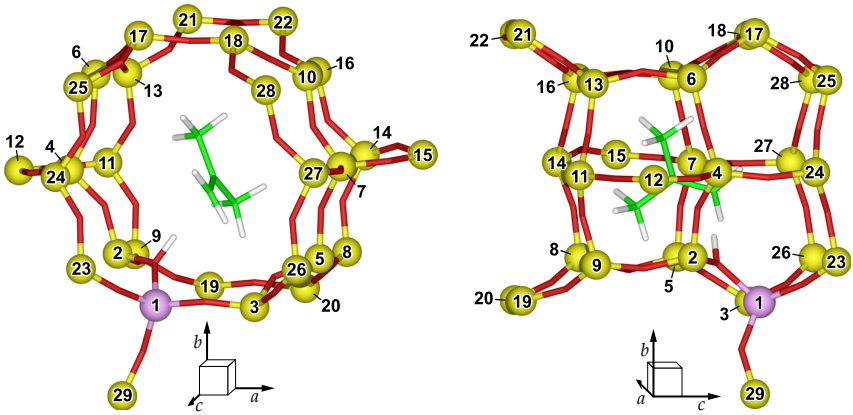

Figure 4.4: *Views along c (left panel) and a direction (right panel) of the largest cluster model used in the convergence study. The numbering indicates the order of T-atoms included in successive cluster models of increasing size. Terminating OH-groups are not shown*

Due to different cluster model sizes the length of corresponding cubic computational boxes varies between 21 and 31 Å.[10] Two series of cluster model RI-MP2 calculations are carried out employing different basis sets. First, the TZVP basis set is used for all cluster models. TZVP, however, is known to yield MP2 reaction energies significantly influenced by the BSSE. For this reason a second series of RI-MP2 reaction energy calculations is performed which employs the aug(O)-TZVPP basis set for all cluster models containing not more than 25 T-atoms. BSSE corrections of MP2 reaction energies are made for neither basis set.

Differences between cluster model MP2 and DFT reaction energies show monotonic and convergent behaviour with respect to the cluster size (see Results and Discussion). To extrapolate to the limiting case of an infinitely large cluster, *i. e.*, to the periodic limit, an analytic expression describing this convergence behaviour is required. It is assumed that the size dependence is mainly due to dispersion effects between the growing part

[10]The same computational box is used for the isobutene molecule and cluster models of structures **1** – **5** showing the same number of T-atoms (periodic images are decoupled). This ensures strict basis set consistency in reaction energy calculations.

of the zeolite framework and the hydrocarbon species. Hence, a damped atom–atom pair expansion is used to form an analytic representation,

$$E_{\mathrm{disp}}(n) = -\sum_{i}^{\mathrm{C,H_a}} \sum_{j}^{\mathrm{O,H_z}} \frac{2C_6(i)C_6(j)}{C_6(i)+C_6(j)} \frac{1}{r_{ij}^6} f_{\mathrm{damp}}(r_{ij}) \quad . \tag{4.3}$$

Besides hydrogen (link) atoms H_z only oxygen atoms O are considered as zeolite dispersion sites forming interaction pairs with all carbon and hydrogen atoms, C and H_a, of the hydrocarbon. The damping function, $f_{\mathrm{damp}}(r_{ij})$, quickly decays at interatomic distances r_{ij} smaller than the sum of corresponding van der Waals atom radii. Its functional form and parameter values are taken from the work by Grimme [37]. The term $f_{\mathrm{damp}}(r_{ij})/r_{ij}^6$ is given by the structure of the cluster models, and for a selected series of $n_{\max}$ models,[11] $C(n)$, $E_{\mathrm{disp}}(n)$ is a function of only the C_6 coefficients for C, H_a, O, and H_z.

These coefficients are determined separately for each of the structures **2**–**5** by minimising

$$\Delta\big(\{C_6\}, E_{\mathrm{add}}\big) = \sum_{n=1}^{n_{\max}} \Big[\big(\Delta E_{\mathrm{MP2}}(n) - \Delta E_{\mathrm{PBE}}(n)\big) - \big(E_{\mathrm{disp}}(n) + E_{\mathrm{add}}\big)\Big]^2 \tag{4.4}$$

using standard numerical procedures. For this purpose analytic partial first derivatives of Δ with respect to the variables $(\{C_6\}, E_{\mathrm{add}})$ are supplied. The additional parameter E_{add} accounts for differences in reaction energies between MP2 and DFT common to all cluster models, that is, including high-level corrections not exclusively related to dispersion. With results obtained for $\{C_6\}$ the interatomic potential dispersion energy for an infinitely large cluster, $E_{\mathrm{disp}}(\infty)$, is calculated (see eqn. (4.3)) applying periodic boundary conditions. Inclusion of E_{add} yields a high-level correction extrapolated for the full periodic case,

$$\Delta E_{\mathrm{MP2}}(\infty) - \Delta E_{\mathrm{PBE}}(\infty) \approx E_{\mathrm{disp}}(\infty) + E_{\mathrm{add}} \quad , \tag{4.5}$$

which, after identifying $\Delta E_{\mathrm{PBE}}(\infty)$ as the periodic boundary plane wave DFT result, yields an estimate for the periodic boundary MP2 reaction energy, $\Delta E_{\mathrm{MP2}}(\infty)$.

[11] all cut-outs of the same periodic structure

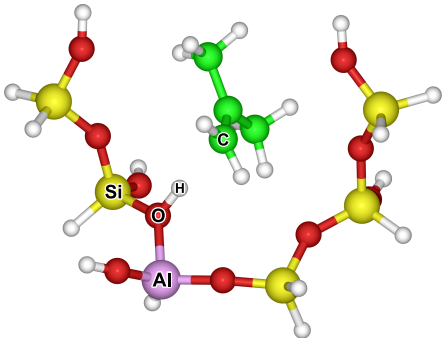

Figure 4.5: *The $6T_{9H}$ cluster model used in CCSD(T) single-point reaction energy calculations*

Note, that the C_6 coefficients determined this way are characteristic for a given structure (**2**–**5**). They are fitted to reproduce reaction energy differences between MP2 and DFT (PBE functional) and as such they do not necessarily represent true C_6 parameters. This prevents transfer of the C_6 coefficients to different systems.

CCSD(T). To assess the reliability of MP2 for hydrocarbon reactions in zeolites, single-point CCSD(T) reaction energy calculations are carried out for the formation of structures **2**–**5** from unloaded H-FER and isobutene. In comparison to MP2, CCSD(T) is computationally much more expensive. In the present case this limits the system to a size smaller than the $16T_{16H}$ cluster model used for hybrid MP2/DFT structure optimisations. A reduced model including 6 zeolite framework T-atoms is constructed from the MP2/DFT optimised periodic structure. 14 hydrogen atoms are added to saturate dangling bonds resulting in 5 TO–H and 9 T–H cluster model terminations. This model, denoted "$6T_{9H}$", is shown in Fig. 4.5. Using Ahlrich's TZVP basis sets for both the $6T_{9H}$ zeolite model and the hydrocarbon part results in system sizes up to 536 contracted basis functions. A frozen core is employed comprising molecular orbitals corresponding to carbon 1s, oxygen 1s, aluminium 1s2s2p, and silicon 1s2s2p atomic orbitals. All CCSD(T) calculations are carried out using the MOLPRO code [176].

Table 4.1: *Reaction energies, ΔE, ZPVE corrected reaction energies, ΔE_0, and reaction enthalpies at 298 K, ΔH_{298}, for the formation of structures **2**–**5** from **1** and isobutene employing simulation cell parameters optimised consistently with DFT (PBE functional). Values in parentheses are obtained with various density functional/pseudopotential combinations employing cell parameters optimised with a shell-model ion-pair potential (all numbers in kJ/mol)*

	2	**3**	**4**	**5**
PBE/Vdb,BHS				
ΔE	−16 (–9)	19 (17)	8 (36)	−3 (5)
ΔE_0	−13 (–7)	30 (35)	−2 (32)	6 (24)
ΔH_{298}	−12 (–5)	27 (28)	2 (35)	7 (19)
PBE/TM				
ΔE	(–9)	(18)	(37)	(7)
BP86/TM				
ΔE	(18)	(44)	(63)	(33)

4.3 Results and Discussion

DFT Structures and Energies. Table 4.1 lists DFT reaction energies for the formation of structures **2**–**5** (see Fig. 4.6) from unloaded H-FER **1** and isobutene; results for two different simulation cells are shown. With either set of cell parameters the π-adsorption complex **2** is energetically preferred over the chemisorption structures **3**–**5**. Employing cell parameters optimised consistently with DFT the carbenium ion **4** is the most stable chemisorption product when zero-point vibrational energy (ZPVE) contributions are included. At room temperature only formation of the π-adsorption complex is exothermic while chemisorption yielding *tert*-butyl carbenium ion or isobutoxide structures is slightly endothermic. Numbers in Tab. 4.1 shown in parentheses are from DFT calculations employing cell parameters obtained with a shell-model ion-pair potential [258, 311]. They predict the isobutoxide **5** as the most stable chemisorption structure. Relative stabilities similar to the present results have been found in previous DFT studies for chabazite, ZSM-22, and mordenite (PW91 functional) [299] and for mordenite (B3PW91 functional) [291].

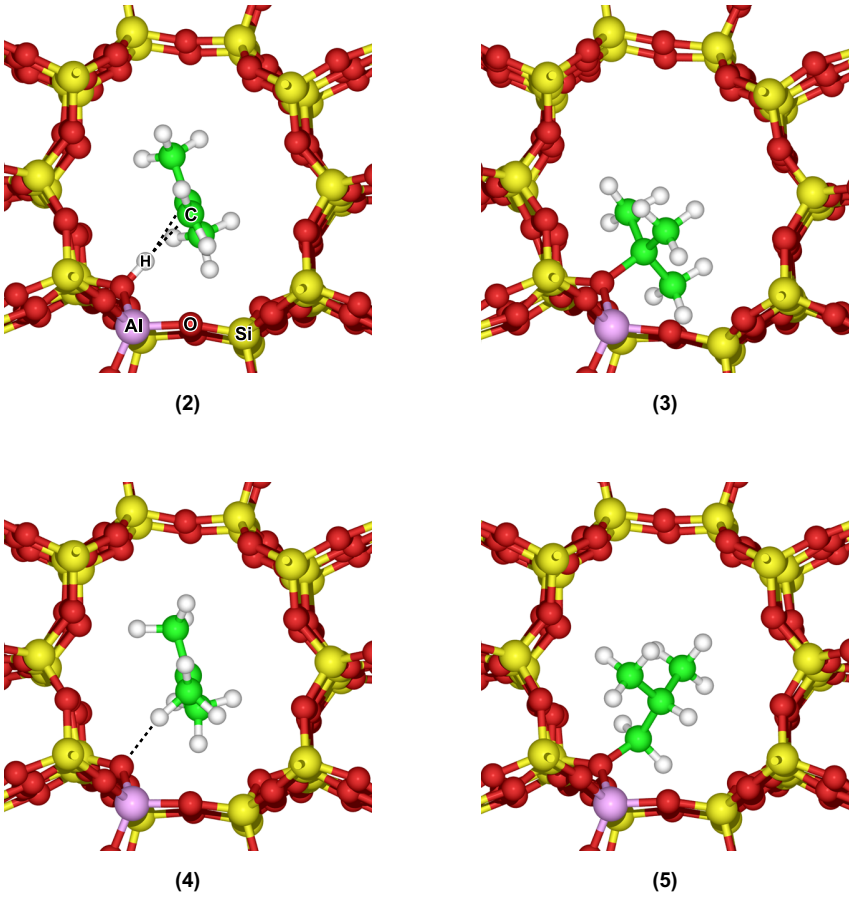

Figure 4.6: *Structure cut-outs of the isobutene – ferrierite π-complex* ***2****, the tert-butoxide* ***3****, the tert-butyl carbenium ion* ***4****, and the isobutoxide* ***5****. Dashed lines represent hydrogen bonds*

It is worth mentioning that PBE reaction energies obtained with a combination of soft and ultrasoft pseudopotentials (BHS and Vdb) and a low plane wave basis set cut-off (30 Ry) are reproduced by computationally much more expensive calculations using norm-conserving pseudopo-

tentials (TM, 110 Ry). Corresponding deviations are 2 kJ/mol at most. In addition to the test calculations performed in Chapter 2, this further supports the use of soft and ultrasoft pseudopotentials in CPMD plane wave DFT calculations. The last line in Tab. 4.1 shows reaction energies obtained with the BP86 functional. As expected they are bigger than those calculated with PBE. Uniform differences between BP86 and PBE reaction energies of 27±1 kJ/mol indicate systematic deficiencies of one or both these forms of the generalised gradient approximation (GGA) for the description of hydrocarbon reactions in zeolite catalysts.

In relation to the results obtained with the shell-model ion-pair potential, lattice parameters *a*, *b*, and *c* increase by 27, 9, and 6 pm, respectively, when the H-FER simulation cell is optimised consistently at the DFT level. Corresponding changes of the total energy per simulation cell for structures **1**–**5** are –21, –28, –19, –50, and –29 kJ/mol, respectively. Compared to the value for the unloaded zeolite **1**, the additional stabilisation of structures **2**, **4**, and **5** can be explained in terms of reduced steric constraints for the hydrocarbon due to slightly increased pore sizes. Far the largest stabilisation is found for the carbenium ion structure (–50 kJ/mol). Finite temperature corrections to reaction energies are less affected by the change of cell parameters. Since each of the relaxed structures **1**–**5** shows a gain in total energy when using consistently optimised cell parameters results obtained with the shell-model ion-pair potential simulation cell are not discussed any further.

Of the two different alkoxides the isobutoxide **5** is more stable than the *tert*-butoxide **3**. The C–O bond length in **3** (161 pm) is elongated compared to that in **5** (152 pm) indicating increased steric constraints due to the presence of three methyl substituents at the C–O carbon atom close to the zeolite wall. Both the adsorbed isobutene and the *tert*-butyl cation are connected to the zeolite framework by hydrogen bonds. Corresponding atom distances are 191 and 247 pm for $r_{\mathrm{ZOH}\cdots\mathrm{C(1)}}$ and $r_{\mathrm{ZOH}\cdots\mathrm{C(2)}}$, respectively, in the π-complex **2** and 182 pm for $r_{\mathrm{ZO}\cdots\mathrm{HC}}$ in the carbenium ion structure **4** (*cf.* Fig. 4.6).

DFT Vibrational Frequencies. Vibrational frequencies obtained by numerical differentiation of forces are shown in Fig. 4.7. A nearly continuous vibrational region from 1250 cm^{-1} down to far infrared with a window between about 1000 and 800 cm^{-1} is seen for unloaded H-FER as well

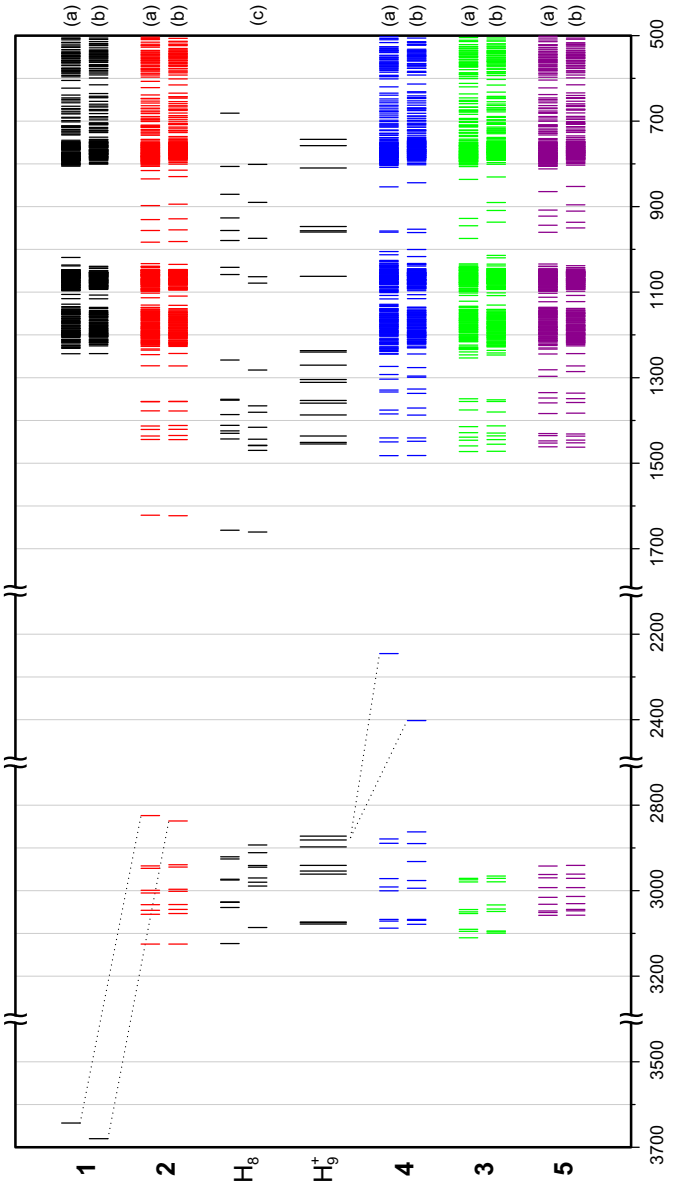

Figure 4.7: *DFT (PBE) vibrational frequencies calculated for periodic structures* ***1*** *–* ***5****, the isobutene molecule (C_4H_8), and the tert-butyl carbenium ion ($C_4H_9^+$). Results obtained with a simulation cell optimised for unloaded H-FER using a shell-model ion-pair potential (a) and DFT (b) are shown. Isobutene vibrational frequencies observed experimentally (c) are included for comparison*

as for the hydrocarbon containing structures.[12] This is characteristic of zeolite lattice vibrations [322]. All stationary points obtained are minima on the DFT potential energy surface indicated by the absence of imaginary vibrational modes. The calculated frequency for the zeolitic O – H (O – D) stretching mode in unloaded H-FER, 3680 (2678) cm^{-1}, does not exactly reproduce experimental data, 3609 (2663) cm^{-1} [303]. Quantitative agreement is not expected because of the limited accuracy of DFT and neglected anharmonicities. The vibrational spectra of structures **2** – **5** approximately resemble superpositions of those of the unloaded zeolite and the gas-phase species. In the isobutene π-complex hydrogen bond formation shifts the zeolitic O – H (O – D) stretching mode by –843 (–603) cm^{-1}. Corresponding measurements on deuterated forms of different zeolites yield somewhat smaller O – D shifts, –416 cm^{-1} (mordenite) [301] and –388 cm^{-1} (faujasite) [302]. It is known [149] that the PBE functional overestimates O – H frequency shifts on hydrogen bond formation. A significant change is predicted for the IR spectrum of the carbenium ion structure **4**. Only 8 instead of 9 vibrational modes are seen in the C – H stretching region around 3000 cm^{-1}. The remaining mode corresponding to the ZO$\cdots$HC hydrogen bond is found at 2402 cm^{-1}, *i. e.*, well separated from all others. This is an important prediction which may help to identify the *tert*-butyl carbenium ion as a transient species in future laser spectroscopic experiments [323, 324].

QM-Pot Structures and Energies. Structural parameters obtained from hybrid MP2/DFT geometry optimisations are different compared to corresponding DFT results. In the π-adsorption complex **2** the hydrogen bond distance between the zeolite acid site and the carbon atom of the methylene group in isobutene increases from 191 pm (DFT) to 202 pm (hybrid MP2/DFT). The length of the π-complex donor O – H bond decreases from 102 pm (DFT) to 99 pm (hybrid MP2/DFT). Similar observations are made for the hydrogen bond of the carbenium ion structure **4**, $r_{ZO\cdots HC} = 227$ pm with $r_{H-C} = 111$ pm (182 and 115 pm, respectively, with DFT). These examples illustrate a correction of the known overbinding tendency of GGA functionals for hydrogen bonds. MP2 corrected structures should also include a shortening of alkoxide C – O bond lengths since the repulsion between hydrocarbon groups and the zeolite surface

[12] numerical data available in Section A.2 (Appendix)

Table 4.2: *Hybrid MP2/DFT reaction energies, $\Delta E(S,L)$, for the formation of structures **2**–**5** from **1** and isobutene. $\Delta E(S,L)$ is decomposed into different QM-Pot energy terms. Values in parentheses are corrected for the BSSE (all numbers in kJ/mol)*

	2	**3**	**4**	**5**
$\Delta E(S,L)$	–77 (–44)	–66 (–8)	–13 (20)	–80 (–27)
$\Delta E(S)_{\mathrm{PBE}}$	–14	21	15	0
$\Delta E(C)_{\mathrm{MP2}} - \Delta E(C)_{\mathrm{PBE}}$	–62 (–30)	–86 (–29)	–28 (5)	–80 (–27)
$\Delta E(C)_{\mathrm{MP2}}$	–78 (–45)	–99 (–41)	23 (56)	–92 (–39)
$\Delta E(S)_{\mathrm{PBE}} - \Delta E(C)_{\mathrm{PBE}}$	1	33	–36	12

is expected to be weaker when dispersion is included. This is confirmed by hybrid MP2/DFT results for the C–O bond length in the *tert*-butoxide **3** (155 pm) and isobutoxide **5** (149 pm) structures when comparing to corresponding DFT values (161 and 152 pm, respectively).

Table 4.2 shows reaction energies obtained from hybrid MP2/DFT calculations. For all structures significantly stronger binding is predicted in comparison to plain DFT (PBE) results. This table also includes decompositions of hybrid MP2/DFT results[13] into contributions from periodic structure DFT, $\Delta E(S)_{\mathrm{PBE}}$, and high-level corrections for the cluster, $\Delta E(C)_{\mathrm{MP2}} - \Delta E(C)_{\mathrm{PBE}}$. The former are similar to the pure DFT results listed in Tab. 4.1. Differences are not bigger than 7 kJ/mol and reflect the changes from DFT to hybrid MP2/DFT optimised structures. Cluster model high-level corrections yield substantial negative contributions to reaction energies, which, in first approximation, is attributed to dispersion effects neglected with DFT (PBE). Another decomposition of $\Delta E(S,L)$ is possible, separating MP2 cluster model results from long-range corrections evaluated at the DFT level, $\Delta E(S)_{\mathrm{PBE}} - \Delta E(C)_{\mathrm{PBE}}$. As the numbers in Tab. 4.2 show, long-range effects must not be neglected and are very different for all structures. For the carbenium ion structure **4** a remarkably large correction, –36 kJ/mol, is observed.

[13] see eqn. (1.4) in Chapter 1, page 6

Table 4.3: *HF and MP2 correlation energy contributions to QM-Pot high-level reaction energies, $\Delta E(C)_{MP2}$, for the formation of structures **2**–**5** from **1** and isobutene obtained with different basis sets.[a] Values in parentheses are corrected for the BSSE. CBS limits are extrapolated from cc-pVXZ basis set results (all numbers in kJ/mol)*

basis set/ component	**2**	**3**	**4**	**5**
TZVP(P)/				
HF	24 (31)	29 (40)	99 (106)	17 (28)
MP2(correl.)	−102 (−76)	−127 (−82)	−76 (−50)	−108 (−66)
cc-pVTZ/				
HF	19 (31)	27 (42)	101 (112)	15 (29)
MP2(correl.)	−105 (−81)	−128 (−86)	−77 (−53)	−109 (−71)
cc-pVQZ/				
HF	28 (31)	38 (41)	110 (113)	25 (29)
MP2(correl.)	−105 (−88)	−124 (−94)	−82 (−64)	−108 (−80)
CBS limit				
HF	31	41	113	29
MP2(correl.)	−94	−99	−72	−87

[a] single-point $16T_{16H}$ cluster model calculations based on hybrid MP2/DFT optimised periodic structures

BSSE and CBS Limits. The MP2 part of the hybrid QM/QM calculations needs further attention because of the presence of the BSSE. For the π-complex **2** and the carbenium ion structure **4** the BSSE is similar, 33 kJ/mol, while for the isobutoxide **5** and the *tert*-butoxide **3** the BSSE is as large as 53 and 58 kJ/mol, respectively (TZVP(P) basis set, see Tab. 4.2). Note, that the BSSE calculation for the alkoxide structures assumes fragments that resemble the corresponding carbenium ion and the negatively charged zeolite framework. Here the BSSE may be due to both close non-bonded contacts of the alkoxides' hydrocarbon part with the zeolite surface and "intramolecular" contributions from the C–O surface bond. Since the BSSE vanishes in the limit of a complete one-particle basis

set, $16T_{16H}$ cluster model MP2 reaction energy CBS limit extrapolations are performed, see eqns. (4.1) and (4.2). Employed HF and MP2 correlation energy contributions obtained with Dunning's basis sets are shown in Tab. 4.3 together with extrapolated CBS limits. Ahlrichs' optimised TZVP(P) basis sets yield smaller BSSE values for HF energies than the larger Dunning cc-pVTZ basis sets whereas for MP2 correlation energies the TZVP(P) BSSE values are slightly bigger. HF reaction energies, in general, converge quicker to the CBS limit than MP2 correlation energy contributions do. MP2 CBS limit corrected hybrid MP2/DFT reaction energies for the formation of structures **2** – **5** add up to −62, −26, 5, and −47 kJ/mol, respectively.

In the next step these hybrid MP2/DFT results are corrected further to account for the finite size of the embedded cluster model.

Convergence with Cluster Model Size. Corrections for long-range effects are missing in calculations employing free cluster models for the reaction site. For this reason it is important to examine the behaviour of the results obtained as a function of the model size. When periodic systems are investigated one can, if available, use full periodic model results as a reference to compare to. In the present case this applies to the series of cluster model DFT reaction energy calculations, see Fig. 4.8. For all systems **2** – **5** monotonic convergence of reaction energies is not observed. Signs and relative stabilities change in an apparently unsystematic manner, and even for the largest cluster models (29 T-atoms) there is by far no agreement to full periodic model reference values.[14]

Convergence patterns similar to those with DFT are obtained for MP2 cluster model reaction energies (Fig. 4.8) and are not suited to estimate corresponding periodic model limits either. However, when differences between MP2 and PBE reaction energies are considered, that is, when the QM-Pot cluster model high-level corrections, $\Delta E(C)_{\mathrm{MP2}} - \Delta E(C)_{\mathrm{PBE}}$, are plotted, monotonically decaying curves are obtained showing asymptotic convergence, see Fig. 4.9. These reaction energy differences are used for fitting an analytic expression, see eqns. (4.3) and (4.4). Results obtained for the parameters[15] in each of the 8 fits are not unique. Depending on

[14] Full periodic model reference values are parenthesised in the first line of Tab. 4.1.
[15] see Tab. B.7 (Appendix), page 141

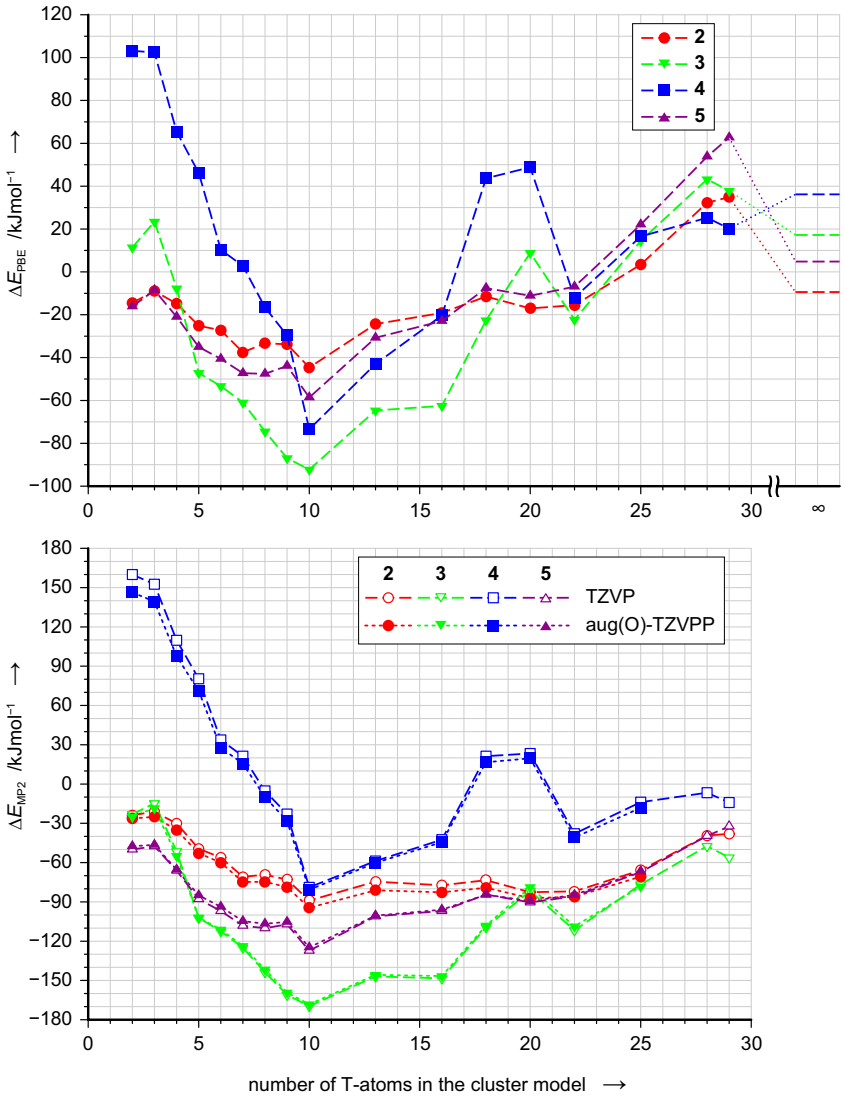

Figure 4.8: *Cluster model reaction energies for the formation of structures* ***2*** *–* ***5*** *from* ***1*** *and isobutene calculated with DFT (upper panel) and MP2 (lower panel). See Tabs. B.5 and B.6 (Appendix) for numerical data*

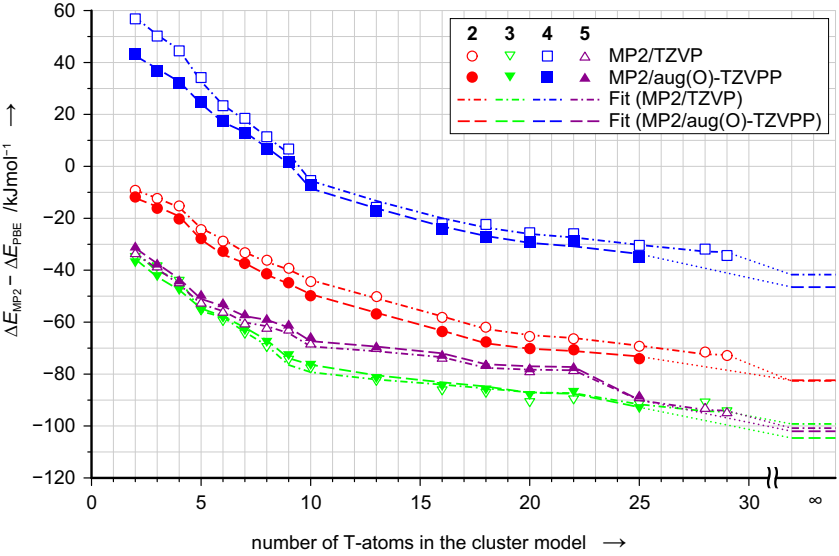

Figure 4.9: *Differences in cluster model reaction energies between MP2 and DFT for the formation of structures **2**–**5** from **1** and isobutene (point plots). Values reproduced by a fitted analytic expression including corresponding results for the full periodic limit are also shown (line plots)*

numerical strategies and initial values employed many solutions with respect to a set of reference data can be found which show virtually the same mean error (RMS).[16] These solutions largely vary in the values for $\{C_6\}$ whereas corresponding parameters E_{add} do not differ. The constant E_{add} can be interpreted in terms of two types of MP2–DFT correction contributions. A probably small fraction is due to dispersion present in even the smallest cluster model, *C*(2T), while the dominating contribution arises from a correction which is independent of the size of the cluster model and not related to dispersion neglected with the PBE functional. RMS errors in fitted reaction energy differences $\Delta E(C)_{\text{MP2}} - \Delta E(C)_{\text{PBE}}$ are 0.54, 1.77, 1.18 and 0.71 kJ/mol for cluster models of structures **2**–**5**, respectively, employing MP2/TZVP data. These errors change to 0.59, 0.73, 0.88, and 0.81 kJ/mol when MP2/aug(O)-TZVPP data are used.

[16] defined as $(\Delta/n_{\text{max}})^{0.5}$ (root mean square), see also eqn. (4.4)

Table 4.4: *Differences in reaction energies between MP2 and PBE, $\Delta E(C)_{MP2} - \Delta E(C)_{PBE}$, for the formation of structures **2** – **5** from **1** and isobutene. Infinite cluster model results are estimated using an analytic expression fitted to corresponding sets of reference data (numbers in kJ/mol)*

model	basis set (MP2)	**2**	**3**	**4**	**5**
infinite cluster model	TZVP	–83	–99	–42	–101
	aug(O)-TZVPP	–83	–104	–47	–102
$16T_{16H}$ cluster model	TZVP	–62	–83	–15	–76
	aug(O)-TZVPP	–67	–82	–21	–76

With parameters obtained in these fits, E_{disp} is calculated (eqn. (4.3)) for every structure **2** – **5** applying periodic boundary conditions. Adding E_{add} allows estimating MP2 – DFT high-level corrections in the full periodic limit, see eqn. (4.5). Table 4.4 summarises the results. It is noted that extrapolated values are virtually the same for all the various equivalent results ($\{C_6\}$, E_{add}) obtained in different fitting runs using the same reference data set. Differences are 6 kJ/mol at most when periodic limit results obtained using MP2/TZVP and MP2/aug(O)-TZVPP basis set data are compared.

To assess the robustness of the fitted model potential (*i. e.*, the stability of estimated MP2 – DFT corrections in the periodic limit), the size of the reference data set, n_{max}, can be reduced and the fitting procedure be repeated (eqn. (4.4)). An interesting test case is the isobutoxide structure **5**. For cluster models containing more than 22 T-atoms, $\Delta E(C)_{\mathrm{MP2}} - \Delta E(C)_{\mathrm{PBE}}$ shows a remarkable drop (Fig. 4.9). This is reproduced very well by the fit on all data points ($n_{\mathrm{max}} = 17$). However, the drop is also predicted from fits including fewer reference points ($n_{\mathrm{max}} < 17$), that is, when only smaller cluster models are considered, see Fig. 4.10. Although not strictly true, the smaller the number of reference values included for fitting, the higher the maximum deviation e_{max} of corresponding reproduced data from the 17 reference points. With all reference values included in the fitting procedure e_{max} is smallest (1 kJ/mol). When n_{max} is reduced to, *e. g.*, 12, 10, 7, and 5 reference values, e_{max} increases to 3, 6, 5, and 9 kJ/mol, respectively. For the purpose of extrapolation, however, it is more important to look at corresponding values obtained in the limit of

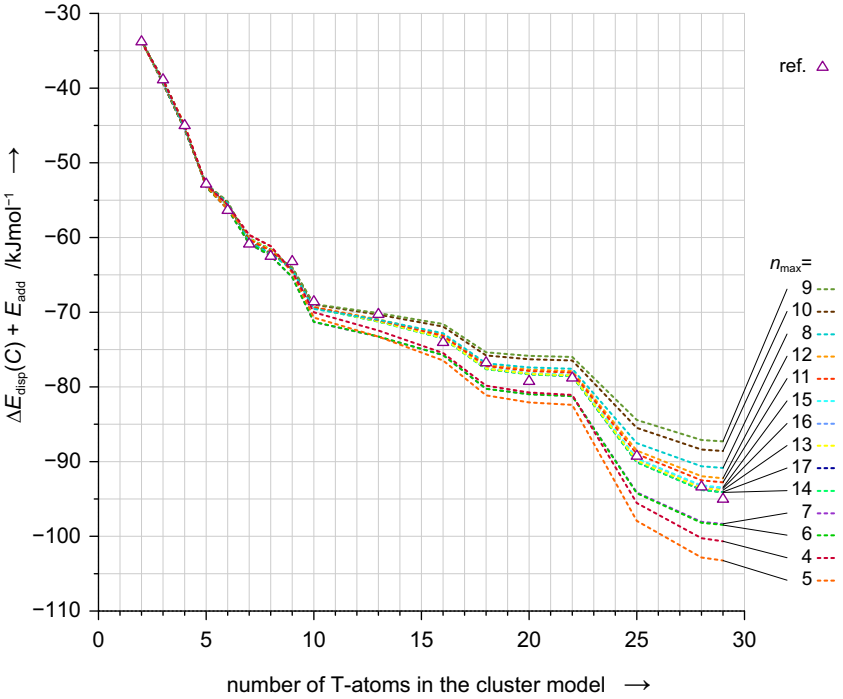

Figure 4.10: *Differences in cluster model reaction energies between MP2 (TZVP basis set) and DFT (PBE) for isobutoxide **5** formation from unloaded H-FER **1** and isobutene (reference data). Dashed lines show corresponding energy values calculated with an analytic expression using parameters fitted to reproduce reference data of the n_{max} smallest cluster models*

the periodic model as a function of $n_{\max}$. Figure 4.11 shows that results constant within 1 kJ/mol are obtained when all cluster models containing at least 20 T-atoms ($n_{\max} \geq 13$) are included in the fitting data set. Errors of about 1 kJ/mol are in the order of the MP2 basis set effect observed before, see Tab. 4.4. Clearly higher fluctuations occur when less cluster model reference points are considered. These observations, in general, prove the reliability of the results obtained from the extrapolation procedure. It also shows that in future applications fewer cluster models might suffice to obtain reliable parametrisations of an analytic model potential.

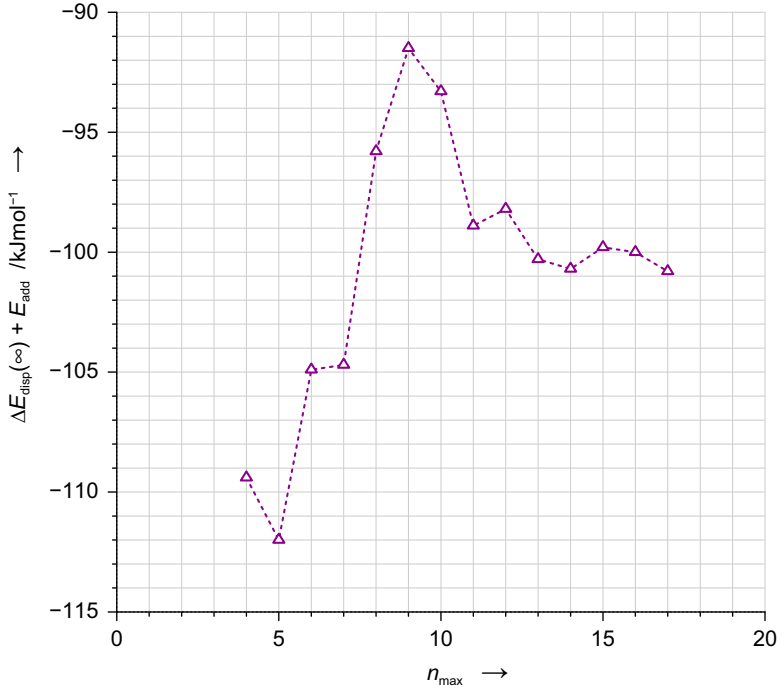

Figure 4.11: *Estimates of the reaction energy difference between MP2 (TZVP basis set) and DFT (PBE) for isobutoxide **5** formation from unloaded H-FER **1** and isobutene obtained in the periodic limit with a damped dispersion term using parameters from fits on n_{max} reference points (eqns. 4.3 – 4.5)*

The QM-Pot $16T_{16H}$ cluster model is not included in the series of models used for fitting and extrapolation. In order to correct the hybrid MP2/DFT results for the finite size of the embedded cluster, single-point $16T_{16H}$ cluster model MP2 reaction energy calculations employing TZVP and aug(O)-TZVPP basis sets, respectively, are carried out as well as corresponding plane wave DFT calculations (see Tab. 4.4). Differences in $\Delta E(C)_{MP2} - \Delta E(C)_{PBE}$ between $16T_{16H}$ and infinite cluster model results constitute the missing corrections[17] to estimate periodic boundary MP2

[17] assuming that MP2 reaction energy basis set superposition errors present with both the $16T_{16H}$ and infinite cluster models approximately cancel out

Table 4.5: *Contributions to estimate periodic boundary MP2 reaction energies for the formation of structures **2**–**5** from **1** and isobutene (in kJ/mol)*

	2	**3**	**4**	**5**
MP2/DFT QM-Pot result [a]	–77	–66	–13	–80
CBS limit correction [b]	15	40	18	33
periodic model correction [c]	–16	–22	–26	–26
estimate periodic MP2	–78	–48	–21	–73
(difference to DFT [d])	(–62)	(–67)	(–29)	(–70)

[a] not corrected for the BSSE (Tab. 4.2); [b] difference in $\Delta E(16T_{16H})_{MP2}$ between the CBS limit and the TZVP(P) basis set results (Tab. 4.3); [c] difference in $\Delta E(C)_{MP2} - \Delta E(C)_{PBE}$ between the infinite and the $16T_{16H}$ cluster model results (Tab. 4.4, aug(O)-TZVPP basis set); [d] with respect to periodic DFT (PBE) structure optimisation results (Tab. 4.1)

reaction energies. Table 4.5 summarises corresponding contributions discussed so far. It shows that finite basis set and finite cluster size corrections go in opposite directions. The net effect is small, –1, –8, and +7 kJ/mol for structures **2**, **4**, and **5**, respectively. For the *tert*-butoxide structure **3** it results in +18 kJ/mol due to a large basis set error correction.

Compared to DFT, MP2 introduces substantial changes in reaction energies describing the formation of structures **2**–**5** from **1** and isobutene as exoenergetic processes. The π-complex **2** and the isobutoxide **5** are clearly the most stable products. Reaction energy differences between MP2 and DFT are similar for the π-complex **2** (–62 kJ/mol) and the alkoxides **3** and **5** (–67 and –70 kJ/mol), the latter two showing gains in relative stabilities compared to **2** (–5 and –8 kJ/mol)[18] when passing from DFT to MP2. This effect is due to van der Waals contacts between the hydrocarbon and the zeolite wall shorter in the alkoxides than in the π-complex. For the formation of the carbenium ion structure **4** from **1** and isobutene, however, only half the difference in reaction energy between MP2 and DFT seen for the other products is observed (–29 kJ/mol). This corresponds to an increase of +33 kJ/mol [19] in the proton transfer energy for the conversion of **2** into **4**, indicating lower stabilities of carbenium

[18] from +35 to +30 and from +13 to +5 kJ/mol, respectively
[19] from +24 to +57 kJ/mol

Table 4.6: *Hartree–Fock (HF) energy, MP2 and CCSD(T) correlation energy contributions to $6T_{9H}$ cluster model reaction energies for the formation of structures **2**–**5** from **1** and isobutene obtained from single-point CCSD(T) calculations (all numbers in kJ/mol)*

	2	**3**	**4**	**5**
HF	14.7	17.8	119.3	86.8
MP2 (correl.)	−59.1	−87.5	−29.3	−68.7
CCSD(T) (correl.)	−59.0	−88.2	−33.3	−69.0
CCSD(T) (total)	−44.3	−70.4	86.0	17.8

ion intermediates in zeolites than predicted by the PBE DFT approach. Figure 4.9 shows how to interpret this finding from the methodological point of view. As all plots show nearly the same progression, that is, the same cluster size effect of reaction energy differences between MP2 and DFT[20], dispersion is hardly to make for the decreased stability of **4**. In first approximation the plots in Fig. 4.9 differ by an energy offset which the additive constant E_{add} within the fitted model potential accounts for. E_{add} is by far largest for the carbenium ion structure, see Tab. B.7 (Appendix, page 141). Structure **4** is of ionic nature, and is has already been observed before that with the PBE density functional the electrostatic attraction between weakly bound fragments tends to be overestimated (see, *e. g.*, protonated water clusters [149, 164] and selected charge-transfer complexes [18]). With hybrid MP2/DFT this overestimation is corrected, and in the present case of the carbenium ion structure MP2 periodic limit this results in partial cancellation of the long-range dispersion energy introduced by MP2.

Energy Corrections beyond MP2. Table 4.6 shows CCSD(T) reaction energies obtained from single-point calculations employing the $6T_{9H}$ cluster model. Differences between CCSD(T) and MP2 correlation energy contributions are very small. They are below ±1 kJ/mol for the formation of the adsorption complex **2** and the alkoxides **3**, **5**. For the carbenium ion structure **4** the MP2 result is corrected by −4 kJ/mol. It is concluded that

[20] see also the periodic model correction in Tab. 4.5

the MP2 description of the systems investigated in the present work yields chemically accurate results. Previous comparisons for, *e. g.*, hydrogen-bonded systems [227, 228] or the water–benzene complex [325] show CCSD(T) corrections to MP2 binding energies of less than 10 %.

Final Estimates. It is difficult to assess the remaining uncertainty of the extrapolated MP2 results, but a range of ±10 kJ/mol is likely to account for possible errors of both the CBS and periodic limit corrections. Also changes due to higher order correlation effects (as obtained by CCSD(T) calculations) are within this limit.

Adopting ZPVE and finite temperature energy contributions calculated with periodic model plane wave DFT (see Tab. 4.1), hybrid MP2/DFT standard heats of formation for structures **2**, **3**, **4**, and **5** are –74, –40, –27, and –63 kJ/mol, respectively. Experimental heats of adsorption for unsaturated hydrocarbons in Brønsted acid zeolites are not available, but it is expected that they will not be very different from the values of the respective saturated hydrocarbons. The presence of a >C=CH_2 group instead of a >CH–CH_3 group will reduce the dispersion interaction, but this is likely to be compensated by specific (hydrogen bond) interaction between the double bond and the zeolitic OH group. Hence, the heat of adsorption of *n*-butane in H-FER (–59 kJ/mol [326], –63 kJ/mol [327]) is taken as a likely value also for isobutene in H-FER. It supports the MP2 estimate for ΔH_{298} = –(74±10) kJ/mol while it contradicts the DFT PBE result of –12 kJ/mol (Tab. 4.1).

4.4 Conclusion

When performing periodic boundary DFT calculations for hydrocarbon reactions in zeolites the choice of the unit cell parameters constitutes an important aspect. They can affect relative stabilities of hydrocarbon species not only in a quantitative but also in a qualitative way. The largest source of error in standard DFT calculations, however, is lack of long-range dispersion. When dispersion is included at the MP2 level, the heat of adsorption changes from –12 kJ/mol (PBE) to the realistic value of –(74±10) kJ/mol (MP2). Dispersion stabilises surface alkoxides to a slightly larger extent (–67 kJ/mol for the *tert*-butoxide and –70 kJ/mol for

the isobutoxide). The *tert*-butyl carbenium ion, hydrogen-bonded to the zeolite framework, is a stable species in H-FER. Seemingly this structure is much less stabilised when passing from DFT to MP2, but this is due to partial cancellation between electrostatic interaction overestimated with the PBE density functional and dispersion introduced with MP2. Complete basis set limit extrapolations, in general, are highly recommended to eliminate the BSIE present in Gaussian basis set MP2 reaction energy calculations. Negligible differences in CCSD(T) and MP2 formation energies obtained from single-point calculations on small cluster models indicate that the structures investigated in this work are well described by MP2.

It is concluded that DFT PBE calculations are not suitable for calculating reaction energy profiles for catalytic hydrocarbon transformations in zeolites. MP2 non-embedded cluster model reaction energies do not converge for cluster sizes up to ~150 atoms, they neither do with DFT. However, MP2 calculations on cluster models embedded in a periodic environment treated by DFT show a smooth asymptotically convergent behaviour as a function of the cluster size. This permits extrapolations of MP2 reaction energies for full periodic models using an analytic damped dispersion term fitted to finite size cluster model reference data.

The present methodology cannot be routinely applied to hydrocarbon reactions in zeolites, but the MP2 results accumulated can serve as benchmarks for DFT+dispersion calculations [37] or for hybrid DFT/force-field calculations [289, 290, 311]. They may also be used as data base for fitting parameters for DFT+dispersion calculations.

Chapter 5

CONCLUDING REMARKS

The hybrid method presented in this work is designed to study problems which involve both bond rearrangements and van der Waals interactions. Reactions between a small or medium sized substrate molecule and a large chemical system, including periodic boundary conditions, can be studied. Though only processes in the pores of zeolites are investigated in this work the method can also be applied to study catalytic transformations of substrates in the binding pockets of enzymes or on solid surfaces, for example. In any case, several constraints apply. First, as for every embedding calculation, a cluster model representing the active site must be defined. This can be a difficult task with, *e. g.*, densely packed systems, delocalised electron orbitals, or when multiple order bonds must be cut. Second, MP2 theory, in principle, should be appropriate to describe both the full system and the cluster model. Third, MP2 cluster model calculations must be feasible. They have been the bottleneck in all MP2/DFT calculations in this work limiting the size of the cluster model in QM-Pot structure optimisations to include less than 100 atoms. Future embedding applications might incorporate local electron correlation schemes in addition to the resolution of the identity approximation, and in this case the HF self-consistent field calculation will limit the maximum size of the cluster model. Extension beyond MP2 is possible when plane wave DFT codes are combined with codes for CCSD(T) gradients. QM/QM calculations of this type, however, are prohibitively expensive at present and will only be carried out in exceptional cases.

Bibliography

[1] P. Hohenberg and W. Kohn. Inhomogeneous Electron Gas. *Phys. Rev. B*, 136:864, 1964.

[2] W. Kohn and L. J. Sham. Self-Consistent Equations Including Exchange and Correlation Effects. *Phys. Rev. A*, 140:1133, 1965.

[3] R. G. Parr and W. Yang. *Density-Functional Theory of Atoms and Molecules*, volume 16 of *International series of monographs on chemistry*. Oxford University Press, Inc., New York, 1989. ISBN 0-19-504279-4.

[4] W. Kohn, A. D. Becke, and R. G. Parr. Density Functional Theory of Electronic Structure. *J. Phys. Chem.*, 100:12974, 1996.

[5] P. M. W. Gill. Density Functional Theory (DFT), Hartree–Fock (HF), and the Self-consistent Field. In P. von Ragué Schleyer, N. L. Allinger, T. Clark, J. Gasteiger, P. A. Kollman, and H. F. Schäfer, III, editors, *Encyclopedia of Computational Chemistry*, volume 1, pages 678–689, Chichester, 1998. John Wiley & Sons, Ltd. ISBN 0-471-96588-X.

[6] W. Koch and M. C. Holthausen. *A Chemist's Guide to Density Functional Theory*. Wiley-VCH, Weinheim, 2000. ISBN 3-527-29918-1.

[7] C. J. Cramer. *Essentials of Computational Chemistry*. John Wiley & Sons, Ltd, Chichester, 2nd edition, 2004. ISBN 0-470-09182-7.

[8] G. E. Scuseria. Linear Scaling Density Functional Calculations with Gaussian Orbitals. *J. Phys. Chem. A*, 103:4782, 1999.

[9] S. Goedecker and G. E. Scuseria. Linear Scaling Electronic Structure Methods in Chemistry and Physics. *Comput. Sci. Eng.*, 5:14, 2003.

[10] J. Grotendorst, editor. *High Performance Computing in Chemistry*, volume 25 of *Publication Series of the John von Neumann Institute for Computing (NIC)*, Jülich, 2005. NIC-Directors, Research Centre Jülich. ISBN 3-00-013618-5.

[11] C.-H. Hu and D. P. Chong. Density Functional Applications. In P. von Ragué Schleyer, N. L. Allinger, T. Clark, J. Gasteiger, P. A. Kollman, and H. F. Schäfer, III, editors, *Encyclopedia of Computational Chemistry*, volume 1, pages 664–678, Chichester, 1998. John Wiley & Sons, Ltd. ISBN 0-471-96588-X.

[12] T. A. Wesołowski. Comment on "Anisotropic intermolecular interactions in van der Waals and hydrogen-bonded complexes: What can we get from density-functional calculations?" [J. Chem. Phys. 111, 7727 (1999)]. *J. Chem. Phys.*, 113:1666, 2000.

[13] B. J. Lynch and D. G. Truhlar. How Well Can Hybrid Density Functional Methods Predict Transition State Geometries and Barrier Heights? *J. Phys. Chem. A*, 105:2936, 2001.

[14] S. Tsuzuki and H. P. Lüthi. Interaction energies of van der Waals and hydrogen bonded systems calculated using density functional theory: Assessing the PW91 model. *J. Chem. Phys.*, 114:3949, 2001.

[15] T. van Mourik and R. J. Gdanitz. A critical note on density functional theory studies on rare-gas dimers. *J. Chem. Phys.*, 116:9620, 2002.

[16] Y. Zhao, J. Pu, B. J. Lynch, and D. G. Truhlar. Tests of second-generation and third-generation density functionals for thermochemical kinetics. *Phys. Chem. Chem. Phys.*, 6:673, 2004.

[17] S. Andersson and M. Grüning. Performance of Density Functionals for Calculating Barrier Heights of Chemical Reactions Relevant to Astrophysics. *J. Phys. Chem. A*, 108:7621, 2004.

[18] Y. Zhao and D. G. Truhlar. Benchmark Databases for Nonbonded Interactions and Their Use To Test Density Functional Theory. *J. Chem. Theory Comput.*, 1:415, 2005.

[19] J. Černý and P. Hobza. The X3LYP extended density functional accurately describes H-bonding but fails completely for stacking. *Phys. Chem. Chem. Phys.*, 7:1624, 2005.

[20] Y. Zhao, N. González-García, and D. G. Truhlar. Benchmark Database of Barrier Heights for Heavy Atom Transfer, Nucleophilic Substitution, Association, and Unimolecular Reactions and Its Use to Test Theoretical Methods. *J. Phys. Chem. A*, 109:2012, 2005.

[21] A. Ruzsinszky, J. P. Perdew, and G. I. Csonka. Binding Energy Curves from Nonempirical Density Functionals II. van der Waals Bonds in Rare-Gas and Alkaline-Earth Diatomics. *J. Phys. Chem. A*, 109:11015, 2005.

[22] E. R. Johnson and G. A. DiLabio. Structure and binding energies in van der Waals dimers: Comparison between density functional theory and correlated ab initio methods. *Chem. Phys. Lett.*, 419:333, 2006.

[23] A. E. Mattson. In Pursuit of the "Divine" Functional. *Science*, 298: 759, 2002.

[24] J. P. Perdew, A. Ruzsinszky, J. Tao, V. N. Staroverov, G. E. Scuseria, and G. I. Csonka. Prescription for the design and selection of density functional approximations: More constraint satisfaction with fewer fits. *J. Chem. Phys.*, 123:062201, 2005.

[25] A. D. Boese, N. L. Doltsinis, N. C. Handy, and M. Sprik. New generalized gradient approximation functionals. *J. Chem. Phys.*, 112: 1670, 2000.

[26] Y. Zhao, N. E. Schultz, and D. G. Truhlar. Design of Density Functionals by Combining the Method of Constraint Satisfaction with Parametrization for Thermochemistry, Thermochemical Kinetics, and Noncovalent Interactions. *J. Chem. Theory Comput.*, 2:364, 2006.

[27] J. F. Dobson and B. P. Dinte. Constraint Satisfaction in Local and Gradient Susceptibility Approximations: Application to a van der Waals Density Functional. *Phys. Rev. Lett.*, 76:1780, 1996.

[28] M. Dion, H. Rydberg, E. Schröder, D. C. Langreth, and B. I. Lundqvist. Van der Waals Density Functional for General Geometries. *Phys. Rev. Lett.*, 92:246401, 2004. Erratum: *Phys. Rev. Lett.*, 95:109902,2005.

[29] J. G. Ángyán, I. C. Gerber, A. Savin, and J. Toulouse. van der Waals forces in density functional theory: Perturbational long-range electron-interaction corrections. *Phys. Rev. A*, 72:012510, 2005.

[30] J. F. Dobson and J. Wang. Successful Test of a Seamless van der Waals Density Functional. *Phys. Rev. Lett.*, 82:2123, 1999.

[31] W. Kohn, Y. Meir, and D. E. Makarov. van der Waals Energies in Density Functional Theory. *Phys. Rev. Lett.*, 80:4153, 1998.

[32] F. Furche and T. Van Voorhis. Fluctuation-dissipation theorem density-functional theory. *J. Chem. Phys.*, 122:164106, 2005.

[33] M. Elstner, P. Hobza, T. Frauenheim, S. Suhai, and E. Kaxiras. Hydrogen bonding and stacking interactions of nucleic acid base pairs: A density-functional-theory based treatment. *J. Chem. Phys.*, 114: 5149, 2001.

[34] X. Wu, M. C. Vargas, S. Nayak, V. Lotrich, and G. Scoles. Towards extending the applicability of density functional theory to weakly bound systems. *J. Chem. Phys.*, 115:8748, 2001.

[35] Q. Wu and W. Yang. Empirical correction to density functional theory for van der Waals interactions. *J. Chem. Phys.*, 116:515, 2002.

[36] U. Zimmerli, M. Parrinello, and P. Koumoutsakos. Dispersion corrections to density functionals for water aromatic interactions. *J. Chem. Phys.*, 120:2693, 2004.

[37] S. Grimme. Accurate Description of van der Waals Complexes by Density Functional Theory Including Empirical Corrections. *J. Comput. Chem.*, 25:1463, 2004.

[38] S. J. A. van Gisbergen, J. G. Snijders, and E. J. Baerends. A density functional theory study of frequency-dependent polarizabilities and Van der Waals dispersion coefficients for polyatomic molecules. *J. Chem. Phys.*, 103:9347, 1995.

[39] A. D. Becke and E. R. Johnson. Exchange-hole dipole moment and the dispersion interaction. *J. Chem. Phys.*, 122:154104, 2005.

[40] E. R. Johnson and A. D. Becke. A post-Hartree–Fock model of intermolecular interactions. *J. Chem. Phys.*, 123:024101, 2005.

[41] D. R. Hartree. The Wave Mechanics of an Atom with a Non-Coulomb Central Field. Part I –Theory and Methods. *Proc. Camb. Phil. Soc.*, 24:89, 1928.

[42] V. Fock. Näherungsmethode zur Lösung des quantenmechanischen Mehrkörperproblems. *Z. Phys.*, 61:126, 1930.

[43] J. C. Slater. Note on Hartree's Method. *Phys. Rev.*, 35:210, 1930.

[44] C. C. J. Roothaan. New Developments in Molecular Orbital Theory. *Rev. Mod. Phys.*, 23:69, 1951.

[45] G. G. Hall. The Molecular Orbital Theory of Chemical Valency. VIII. A Method of Calculating Ionization Potentials. *Proc. Roy. Soc. Lond. A*, 205:541, 1951.

[46] A. Szabo and N. S. Ostlund. *Modern Quantum Chemistry: Introduction to Advanced Structure Theory*. Dover Publications, Inc., Mineola, New York, 1996. ISBN 0-486-69186-1.

[47] K. Raghavachari and J. B. Anderson. Electron Correlation Effects in Molecules. *J. Phys. Chem.*, 100:12960, 1996.

[48] P. Knowles, M. Schütz, and H.-J. Werner. Ab Initio Methods for Electron Correlation in Molecules. In J. Grotendorst, editor, *Modern Methods and Algorithms of Quantum Chemistry*, volume 3 (second edition) of *Publication Series of the John von Neumann Institute for Computing (NIC)*, pages 97–179, Jülich, 2000. NIC-Directors, Research Centre Jülich. ISBN 3-00-005834-6.

[49] W. Klopper. R12 Methods, Gaussian Geminals. In J. Grotendorst, editor, *Modern Methods and Algorithms of Quantum Chemistry*, volume 3 (second edition) of *Publication Series of the John von Neumann Institute for Computing (NIC)*, pages 181–229, Jülich, 2000. NIC-Directors, Research Centre Jülich. ISBN 3-00-005834-6.

[50] T. Helgaker, P. Jørgensen, and J. Olsen. *Molecular Electronic-Structure Theory*. John Wiley & Sons, Ltd, Chichester, 2000. ISBN 0-471-96755-6.

[51] C. Møller and M. S. Plesset. Note on an Approximation Treatment for Many-Electron Systems. *Phys. Rev.*, 46:618, 1934.

[52] D. Cremer. Møller–Plesset Perturbation Theory. In P. von Ragué Schleyer, N. L. Allinger, T. Clark, J. Gasteiger, P. A. Kollman, and H. F. Schäfer, III, editors, *Encyclopedia of Computational Chemistry*, volume 3, pages 1706–1735, Chichester, 1998. John Wiley & Sons, Ltd. ISBN 0-471-96588-X.

[53] A. Warshel and M. Levitt. Theoretical Studies of Enzymic Reactions: Dielectric, Electrostatic and Steric Stabilization of the Carbonium Ion in the Reaction of Lysozyme. *J. Mol. Biol.*, 103:227, 1976.

[54] J. Gao. Methods and Applications of Combined Quantum Mechanical and Molecular Mechanical Potentials. In K. B. Lipkowitz and D. B. Boyd, editors, *Reviews in Computatioinal Chemistry*, volume 7, pages 119–185, New York, 1996. VCH Publishers, Inc. ISBN 1-56081-915-4.

[55] D. Bakowies and W. Thiel. Hybrid Models for Combined Quantum Mechanical and Molecular Mechanical Approaches. *J. Phys. Chem.*, 100:10580, 1996.

[56] J. Gao and M. A. Thompson, editors. *Combined Quantum Mechanical and Molecular Mechanical Methods*, volume 712 of *ACS Symposium Series*, Washington, DC, 1998. American Chemical Society. ISBN 0-8412-3590-2.

[57] T. Z. Mordasini and W. Thiel. Combined quantum mechanical and molecular mechanical approaches. *Chimia*, 52:288, 1998.

[58] G. Monard and K. M. Merz, Jr. Combined Quantum Mechanical/Molecular Mechanical Methodologies Applied to Biomolecular Systems. *Acc. Chem. Res.*, 32:904, 1999.

[59] P. Sherwood. Hybrid Quantum Mechanics/Molecular Mechanics Approaches. In J. Grotendorst, editor, *Modern Methods and Algorithms of Quantum Chemistry*, volume 3 (second edition) of *Publication Series of the John von Neumann Institute for Computing (NIC)*, pages 285–305, Jülich, 2000. NIC-Directors, Research Centre Jülich. ISBN 3-00-005834-6.

[60] T. Vreven and K. Morokuma. On the Application of the IMOMO (Integrated Molecular Orbital + Molecular Orbital) Method. *J. Comput. Chem.*, 21:1419, 2000.

[61] J. Sauer and M. Sierka. Combining Quantum Mechanics and Interatomic Potential Functions in Ab Initio Studies of Extended Systems. *J. Comput. Chem.*, 21:1470, 2000.

[62] P. Sherwood, A. H. de Vries, M. F. Guest, G. Schreckenbach, C. R. A. Catlow, S. A. French, A. A. Sokol, S. T. Bromley, W. Thiel, A. J. Turner, S. Billeter, F. Terstegen, S. Thiel, J. Kendrick, S. C. Rogers, J. Casci, M. Watson, F. King, E. Karlsen, M. Sjøvoll, A. Fahmi, A. Schäfer, and C. Lennartz. QUASI: A general purpose implementation of the QM/MM approach and its application to problems in catalysis. *J. Mol. Struct. (Theochem)*, 632:1, 2003.

[63] M. Sierka and J. Sauer. Hybrid Quantum Mechanics/Molecular Mechanics Methods and Their Application. In S. Yip, editor, *The Handbook of Materials Modeling*, pages 241–258, Dordrecht, 2005. Springer. ISBN 1-4020-3287-0.

[64] H. Lin and D. G. Truhlar. QM/MM: what have we learned, where are we, and where do we go from here? *Theor. Chem. Acc.*, 115:(in press), 2006.

[65] B. W. Hopkins and G. S. Tschumper. A Multicentered Approach to Integrated QM/QM Calculations. Applications to Multiply Hydrogen Bonded Systems. *J. Comput. Chem.*, 24:1563, 2003.

[66] M. A. Nygren, L. G. M. Pettersson, Z. Barandiarán, and L. Seijo. Bonding between CO and the MgO(001) surface: A modified picture. *J. Chem. Phys.*, 100:2010, 1994.

[67] E. V. Stefanovich and T. H. Truong. Embedded density functional approach for calculations of adsorption on ionic crystals. *J. Chem. Phys.*, 104:2946, 1996.

[68] N. Govind, Y. A. Wang, and E. A. Carter. Electronic-structure calculations by first-principles density-based embedding of explicitly correlated systems. *J. Chem. Phys.*, 110:7677, 1999.

[69] M. Eichinger, P. Tavan, J. Hutter, and M. Parrinello. A hybrid method for solutes in complex solvents: Density functional theory combined with empirical force fields. *J. Chem. Phys.*, 110:10452, 1999.

[70] V. A. Nasluzov, V. V. Rivanenkov, A. B. Gordienko, K. M. Neyman, U. Birkenheuer, and N. Rösch. Cluster embedding in an elastic polarizable environment: Density functional study of Pd atoms adsorbed at oxygen vacancies of MgO(001). *J. Chem. Phys.*, 115:8157, 2001.

[71] A. Laio, J. VandeVondele, and U. Rothlisberger. A Hamiltonian electrostatic coupling scheme for hybrid Car–Parrinello molecular dynamics simulations. *J. Chem. Phys.*, 116:6941, 2002.

[72] U. C. Singh and P. A. Kollman. A Combined *Ab Initio* Quantum Mechanical and Molecular Mechanical Method for Carrying out Simulations on Complex Molecular Systems: Applications to the $CH_3Cl + Cl^-$ Exchange Reaction and Gas Phase Protonation of Polyethers. *J. Comput. Chem.*, 7:718, 1986.

[73] J. Sauer. Molecular Models in ab Initio Studies of Solids and Surfaces: From Ionic Crystals and Semiconductors to Catalysts. *Chem. Rev.*, 89:199, 1989.

[74] M. J. Field, P. A. Bash, and M. Karplus. A Combined Quantum Mechanical and Molecular Mechanical Potential for Molecular Dynamics Simulations. *J. Comput. Chem.*, 11:700, 1990.

[75] U. Eichler, C. M. Kölmel, and J. Sauer. Combining Ab Initio Techniques with Analytical Potential Functions for Structure Predictions of Large Systems: Method and Application to Crystalline Silica Polymorphs. *J. Comput. Chem.*, 18:463, 1997.

[76] T. Krüger and A. F. Sax. Oligovalent Link Atoms in Embedding Calculations. *J. Comput. Chem.*, 23:371, 2002.

[77] D. Das, K. P. Eurenius, E. M. Billings, P. Sherwood, D. C. Chatfield, M. Hodošček, and B. R. Brooks. Optimization of quantum mechanical molecular mechanical partitioning schemes: Gaussian

delocalization of molecular mechanical charges and the double link atom method. *J. Chem. Phys.*, 117:10534, 2002.

[78] P. Amara and M. J. Field. Evaluation of an ab initio quantum mechanical/molecular mechanical hybrid-potential link-atom method. *Theor. Chem. Acc.*, 109:43, 2003.

[79] I. Antes and W. Thiel. Adjusted Connection Atoms for Combined Quantum Mechanical and Molecular Mechanical Methods. *J. Phys. Chem. A*, 103:9290, 1999.

[80] R. Poteau, I. Ortega, F. Alary, A. Ramirez Solis, J.-C. Barthelat, and J.-P. Daudey. Effective Group Potentials. 1. Method. *J. Phys. Chem. A*, 105:198, 2001.

[81] G. A. DiLabio, M. M. Hurley, and P. A. Christiansen. Simple one-electron quantum capping potentials for use in hybrid QM/MM studies of biological molecules. *J. Chem. Phys.*, 116:9578, 2002.

[82] Y. Zhang. Improved pseudobonds for combined *ab initio* quantum mechanical/molecular mechanical methods. *J. Chem. Phys.*, 122: 024114, 2005.

[83] V. Théry, D. Rinaldi, J.-L. Rivail, B. Maigret, and G. G. Ferenczy. Quantum Mechanical Computations on Very Large Molecular Systems: The Local Self-Consistent Field Method. *J. Comput. Chem.*, 15: 269, 1994.

[84] R. B. Murphy, D. M. Philipp, and R. A. Friesner. A Mixed Quantum Mechanics/Molecular Mechanics (QM/MM) Method for Large-Scale Modeling of Chemistry in Protein Environments. *J. Comput. Chem.*, 21:1442, 2000.

[85] J. Pu, J. Gao, and D. G. Truhlar. Generalized Hybrid-Orbital Method for Combining Density Functional Theory with Molecular Mechanicals. *ChemPhysChem*, 6:1853, 2005.

[86] M. Sierka and J. Sauer. Finding transition structures in extended systems: A strategy based on a combined quantum mechanics–empirical valence bond approach. *J. Chem. Phys.*, 112:6983, 2000.

[87] S. Dapprich, I. Komáromi, K. S. Byun, K. Morokuma, and M. J. Frisch. A new ONIOM implementation in Gaussian98. Part I. The calculation of energies, gradients, vibrational frequencies and electric field derivatives. *J. Mol. Struct. (Theochem)*, 461-462:1, 1999.

[88] M. Sierka. *Combining Quantum Mechanics and Interatomic Potential Functions in Quantum Chemical Studies of Extended Systems*. Phd thesis, Humboldt-Universität zu Berlin, 2000.

[89] D. Heidrich, W. Kliesch, and W. Quapp. *Properties of Chemically Interesting Potential Energy Surfaces*, volume 56 of *Lecture Notes in Chemistry*. Springer-Verlag, Berlin Heidelberg, 1991. ISBN 3-540-54286-8.

[90] B. Liu and A. D. McLean. Accurate calculation of the attractive interaction of two ground state helium atoms. *J. Chem. Phys.*, 59: 4557, 1973.

[91] S. F. Boys and F. Bernardi. The calculation of small molecular interactions by the differences of separate total energies. Some procedures with reduced errors. *Mol. Phys.*, 19:553, 1970.

[92] F. B. van Duijneveldt, J. G. C. M. van Duijneveldt-van de Rijdt, and J. H. van Lenthe. State of the Art in Counterpoise Theory. *Chem. Rev.*, 94:1873, 1994.

[93] M. Sprik, J. Hutter, and M. Parrinello. Ab initio molecular dynamics simulation of liquid water: Comparison of three gradient-corrected density functionals. *J. Chem. Phys.*, 105:1142, 1996.

[94] S. B. Andrews, N. A. Burton, I. H. Hillier, J. M. Holender, and M. J. Gillan. Molecular electronic structure calculations employing a plane wave basis: a comparison with Gaussian basis calculations. *Chem. Phys. Lett.*, 261:521, 1996.

[95] R. J. Meier. On the effectiveness of ultra-soft pseudopotentials in plane-wave based molecular electronic structure calculations. *J. Mol. Struct. (Theochem)*, 467:79, 1999.

[96] M. Preuss, W. G. Schmidt, K. Seino, J. Furthmüller, and F. Bechstedt. Ground- and Excited-State Properties of DNA Base Molecules from

Plane-Wave Calculations Using Ultrasoft Pseudopotentials. *J. Comput. Chem.*, 25:112, 2004.

[97] C. Raynaud, L. Maron, F. Jolibois, J.-P. Daudey, P. M. Esteves, and A. Ramírez-Solís. Ab initio molecular dynamics: Plane waves vs. local basis – The role of energy cutoff on the convergence of molecular properties. *Chem. Phys. Lett.*, 414:161, 2005.

[98] T. Todorova, A. P. Seitsonen, J. Hutter, I.-F. W. Kuo, and C. J. Mundy. Molecular Dynamics Simulation of Liquid Water: Hybrid Density Functionals. *J. Phys. Chem. B*, 110:3685, 2006.

[99] R. S. Fellers, D. Barsky, F. Gygi, and M. Colvin. An ab initio study of DNA base pair hydrogen bonding: a comparison of plane-wave versus Gaussian-type function methods. *Chem. Phys. Lett.*, 312:548, 1999.

[100] P. Pulay, S. Saebo, M. Malagoli, and J. Baker. Accuracy and Efficiency of Atomic Basis Set Methods Versus Plane Wave Calculations with Ultrasoft Pseudopotentials for DNA Base Molecules. *J. Comput. Chem.*, 26:599, 2005.

[101] C. Janfelt and F. Jensen. The magnitude of pseudo-potential errors for density functional calculations. *Chem. Phys. Lett.*, 406:501, 2005.

[102] F. Jensen and C. Janfelt. The magnitude of pseudo-potential errors for bond distances and vibrational frequencies. *Chem. Phys. Lett.*, 412:12, 2005.

[103] J. Paier, R. Hirschl, M. Marsman, and G. Kresse. The Perdew-Burke-Ernzerhof exchange-correlation functional applied to the G2-1 test set using a plane-wave basis set. *J. Chem. Phys.*, 122:234102, 2005.

[104] J. Hutter et al. *CPMD (versions 3.7.x)*. Copyright MPI für Festkörperforschung Stuttgart 1997–2001 and IBM Corp. 1990–2004. (see also `http://www.cpmd.org`).

[105] D. Marx and J. Hutter. *Ab Initio* Molecular Dynamics: Theory and Implementation. In J. Grotendorst, editor, *Modern Methods and Algorithms of Quantum Chemistry*, volume 3 (second edition) of *Publication Series of the John von Neumann Institute for Computing*

(NIC), pages 329–477, Jülich, 2000. NIC-Directors, Research Centre Jülich. ISBN 3-00-005834-6.

[106] W. Andreoni and A. Curioni. New advances in chemistry and materials science with CPMD and parallel computing. *Par. Comput.*, 26:819, 2000.

[107] J. Hutter and A. Curioni. Dual-level parallelism for ab initio molecular dynamics: Reaching teraflop performance with the CPMD code. *Par. Comput.*, 31:1, 2005.

[108] J. Hutter and A. Curioni. Car-Parrinello Molecular Dynamics on Massively Parallel Computers. *ChemPhysChem*, 6:1788, 2005.

[109] D. J. Singh. *Planewaves, Pseudopotentials and the LAPW Method*. Kluwer Academic Publishers, Norwell, 1994. ISBN 0-7923-9421-7.

[110] E. Wimmer, H. Krakauer, M. Weinert, and A. J. Freeman. Full-potential self-consistent linearized-augmented-plane-wave method for calculating the electronic structure of molecules and surfaces: O_2 molecule. *Phys. Rev. B*, 24:864, 1981.

[111] P. E. Blöchl. Projector augmented-wave method. *Phys. Rev. B*, 50: 17953, 1994.

[112] K. Schwarz, P. Blaha, and G. K. H. Madsen. Electronic structure calculations of solids using the WIEN2k package for material sciences. *Comput. Phys. Commun.*, 147:71, 2002.

[113] L. Füsti-Molnar and P. Pulay. Accurate molecular integrals and energies using combined plane wave and Gaussian basis sets in molecular electronic structure theory. *J. Chem. Phys.*, 116:7795, 2002.

[114] W. E. Pickett. Pseudopotential methods in condensed matter applications. *Comput. Phys. Rep.*, 9:115, 1989.

[115] M. C. Payne, M. P. Teter, D. C. Allan, T. A. Arias, and J. D. Joannopoulos. Iterative minimization techniques for *ab initio* total-energy calculations: molecular dynamics and conjugate gradients. *Rev. Mod. Phys.*, 64:1045, 1992.

[116] E. Ordejón, P. Artacho, and J. M. Soler. Self-consistent order-*N* density-functional calculations for very large systems. *Phys. Rev. B*, 53:R10441, 1996.

[117] G. Lippert, J. Hutter, and M. Parrinello. A hybrid Gaussian and plane wave density functional scheme. *Mol. Phys.*, 92:477, 1997.

[118] G. Lippert, J. Hutter, and M. Parrinello. The Gaussian and augmented-plane-wave density functional method for ab initio molecular dynamics simulations. *Theor. Chem. Acc.*, 103:124, 1999.

[119] M. Krack and M. Parrinello. All-electron *ab-initio* molecular dynamics. *Phys. Chem. Chem. Phys.*, 2:2105, 2000.

[120] L. Füsti-Molnár and P. Pulay. The Fourier transform Coulomb method: Efficient and accurate calculation of the Coulomb operator in a Gaussian basis. *J. Chem. Phys.*, 117:7827, 2002.

[121] F. Gygi and A. Baldereschi. Self-consistent Hartree-Fock and screened-exchange calculations in solids: Application to silicon. *Phys. Rev. B*, 34:4405, 1986.

[122] S. Chawla and G. A. Voth. Exact exchange in *ab initio* molecular dynamics: An efficient plane-wave based algorithm. *J. Chem. Phys.*, 108:4697, 1998.

[123] E. Ruiz, A. Rodríguez-Fortea, J. Tercero, T. Cauchy, and C. Massobrio. Exchange coupling in transition-metal complexes via density-functional theory: Comparison and reliability of different basis set approaches. *J. Chem. Phys.*, 123:074102, 2005.

[124] R. W. Hockney. The Potential Calculation and Some Applications. In B. Alder, editor, *Plasma Physics*, volume 9 of *Methods in Computational Physics*, pages 135–211, New York, 1970. Academic Press, Inc. ISBN 0-12-460809-4.

[125] J. W. Eastwood and D. R. K. Brownrigg. Remarks on the Solution of Poisson's Equation for Isolated Systems. *J. Comput. Phys.*, 32:24, 1979.

[126] J. P. Perdew, K. Burke, and M. Ernzerhof. Generalized Gradient Approximation Made Simple. *Phys. Rev. Lett.*, 77:3865, 1996. Erratum: *Phys. Rev. Lett.*, 78:1396,1997.

[127] R. Car and M. Parrinello. Unified Approach for Molecular Dynamics and Density-Functional Theory. *Phys. Rev. Lett.*, 55:2471, 1985.

[128] P. Pulay. *Ab initio* calculation of force constants and equilibrium geometries in polyatomic molecules. I. Theory. *Mol. Phys.*, 17:197, 1969.

[129] S. Froyen and M. L. Cohen. Structural properties of NaCl and KCl under pressure. *J. Phys. C: Solid State Phys.*, 19:2623, 1986.

[130] D. Vanderbilt. Absence of Large Compressive Stress on Si(111). *Phys. Rev. Lett.*, 59:1456, 1987.

[131] P. Gomes Dacosta, O. H. Nielsen, and K. Kunc. Stress theorem in the determination of static equilibrium by the density functional method. *J. Phys. C: Solid State Phys.*, 19:3163, 1986.

[132] G. P. Francis and M. C. Payne. Finite basis set corrections to total energy pseudopotential calculations. *J. Phys.: Condens. Matter*, 2: 4395, 1990.

[133] G.-M. Rignanese, P. Ghosez, J.-C. Charlier, J.-P. Michenaud, and X. Gonze. Scaling hypothesis for corrections to total energy and stress in plane-wave-based *ab initio* calculations. *Phys. Rev. B*, 52: 8160, 1995.

[134] M. Bernasconi, G. L. Chiarotti, P. Focher, S. Scandalo, E. Tosatti, and M. Parrinello. First-principle-constant pressure molecular dynamics. *J. Phys. Chem. Solids*, 56:501, 1995.

[135] M. Fuchs and M. Scheffler. Ab initio pseudopotentials for electronic structure calculations of poly-atomic systems using density-functional theory. *Comput. Phys. Commun.*, 119:67, 1999.

[136] W. C. Topp and J. J. Hopfield. Chemically Motivated Pseudopotential for Sodium. *Phys. Rev. B*, 7:1295, 1973.

[137] T. Starkloff and J. D. Joannopoulos. Local pseudopotential theory for transition metals. *Phys. Rev. B*, 16:5212, 1977.

[138] D. R. Hamann, M. Schlüter, and C. Chiang. Norm-Conserving Pseudopotentials. *Phys. Rev. Lett.*, 43:1494, 1979.

[139] G. B. Bachelet, D. R. Hamann, and M. Schlüter. Pseudopotentials that work: From H to Pu. *Phys. Rev. B*, 26:4199, 1982.

[140] N. Troullier and J. L. Martins. Efficient pseudopotentials for plane-wave calculations. *Phys. Rev. B*, 43:1993, 1991.

[141] L. Kleinman and D. M. Bylander. Efficacious Form for Model Pseudopotentials. *Phys. Rev. Lett.*, 48:1425, 1982.

[142] D. Vanderbilt. Soft self-consistent pseudopotentials in a generalized eigenvalue formalism. *Phys. Rev. B*, 41:7892, 1990.

[143] G. I. Csonka, A. Ruzsinszky, and J. P. Perdew. Proper Gaussian Basis Sets for Density Functional Studies of Water Dimers and Trimers. *J. Phys. Chem. B*, 109:21471, 2005.

[144] X. Xu, Q. Zhang, R. P. Muller, and W. A. Goddard, III. An extended hybrid density functional (X3LYP) with improved descriptions of nonbond interactions and thermodynamic properties of molecular systems. *J. Chem. Phys.*, 122:014105, 2005.

[145] R. J. Hall, I. H. Hillier, and M. A. Vincent. Which density functional should be used to model hydration? *Chem. Phys. Lett.*, 320:139, 2000.

[146] A. Milet, T. Korona, R. Moszynski, and E. Kochanski. Anisotropic intermolecular interactions in van der Waals and hydrogen-bonded complexes: What can we get from density functional calculations? *J. Chem. Phys.*, 111:7727, 1999.

[147] G. S. Tschumper, M. L. Leininger, B. C. Hoffman, E. F. Valeev, H. F. Schaefer, III, and M. Quack. Anchoring the water dimer potential energy surface with explicitly correlated computations and focal point analyses. *J. Chem. Phys.*, 116:690, 2002.

[148] W. Klopper, J. G. C. M. van Duijneveldt-van de Rijdt, and F. B. van Duijneveldt. Computational determination of equilibrium geometry and dissociation energy of the water dimer. *Phys. Chem. Chem. Phys.*, 2:2227, 2000.

[149] C. Tuma, A. D. Boese, and N. C. Handy. Predicting the binding energies of H-bonded complexes: A comparative DFT study. *Phys. Chem. Chem. Phys.*, 1:3939, 1999.

[150] W. Klopper and H. P. Lüthi. The MP2 limit correction applied to coupled cluster calculations of the electronic dissociation energies of the hydrogen fluoride and water dimers. *Mol. Phys.*, 96:559, 1999.

[151] R. Ahlrichs, M. Bär, M. Häser, H. Horn, and C. Kölmel. Electronic structure calculations on workstation computers: The program system TURBOMOLE. *Chem. Phys. Lett.*, 162:165, 1989.

[152] O. Treutler and R. Ahlrichs. Efficient molecular numerical integration schemes. *J. Chem. Phys.*, 102:346, 1995.

[153] A. D. Becke. Density-functional exchange-energy approximation with correct asymptotic behavior. *Phys. Rev. A*, 38:3098, 1988.

[154] J. P. Perdew. Density-functional approximation for the correlation energy of the inhomogeneous electron gas. *Phys. Rev. B*, 33:8822, 1986. Erratum: *Phys. Rev. B*, 34:7406,1986.

[155] T. H. Dunning, Jr. Gaussian basis sets for use in correlated molecular calculations. I. The atoms boron through neon and hydrogen. *J. Chem. Phys.*, 90:1007, 1989.

[156] A. Schäfer, C. Huber, and R. Ahlrichs. Fully optimized contracted Gaussian basis sets of triple zeta valence quality for atoms Li to Kr. *J. Chem. Phys.*, 100:5829, 1994.

[157] F. Weigend, F. Furche, and R. Ahlrichs. Gaussian basis sets of quadruple zeta valence quality for atoms H–Kr. *J. Chem. Phys.*, 119: 12753, 2003.

[158] R. A. Kendall, T. H. Dunning, Jr., and R. J. Harrison. Electron affinities of the first-row atoms revisited. Systematic basis sets and wave functions. *J. Chem. Phys.*, 96:6796, 1992.

[159] S. Goedecker, M. Teter, and J. Hutter. Separable dual-space Gaussian pseudopotentials. *Phys. Rev. B*, 54:1703, 1996.

[160] J. C. Slater. A Simplification of the Hartree-Fock Method. *Phys. Rev.*, 81:385, 1951.

[161] P. A. M. Dirac. Quantum Mechanics of Many-Electron Systems. *Proc. Roy. Soc. Lond. A*, 123:714, 1929.

[162] S. H. Vosko, L. Wilk, and M. Nusair. Accurate spin-dependent electron liquid correlation energies for local spin density calculations: a critical analysis. *Can. J. Phys.*, 58:1200, 1980.

[163] J. P. Perdew and Y. Wang. Accurate and simple analytic representation of the electron-gas correlation energy. *Phys. Rev. B*, 45:13244, 1992.

[164] C. Tuma. *Zum Einsatz ebener Wellen und atomarer Pseudopotentiale in Dichtefunktionalrechnungen und Kombination mit störungstheoretischen Methoden*. Diploma thesis, Humboldt-Universität zu Berlin, 2000.

[165] C. Lee, W. Yang, and R. G. Parr. Development of the Colle-Salvetti correlation-energy formula into a functional of the electron density. *Phys. Rev. B*, 37:785, 1988.

[166] J. P. Perdew. Unified theory of exchange and correlation beyond the local density approximation. In P. Ziesche and H. Eschrig, editors, *Electronic Structure of Solids '91*, volume 17 of *Physical Research*, pages 11–20, Berlin, 1991. Akademie Verlag GmbH. ISBN 3-05-501504-5.

[167] J. P. Perdew, J. A. Chevary, S. H. Vosko, K. A. Jackson, M. R. Pederson, D. J. Singh, and C. Fiolhais. Atoms, molecules, solids, and surfaces: Applications of the generalized gradient approximation for exchange and correlation. *Phys. Rev. B*, 46:6671, 1992. Erratum: *Phys. Rev. B*, 48:4978,1993.

[168] T. A. Wesołowski, O. Parisel, Y. Ellinger, and J. Weber. Comparative Study of Benzene$\cdots$X (X = O_2, N_2, CO) Complexes Using Density Functional Theory: The Importance of an Accurate Exchange-Correlation Energy Density at High Reduced Density Gradients. *J. Phys. Chem. A*, 101:7818, 1997.

[169] Y. Zhang, W. Pan, and W. Yang. Describing van der Waals Interaction in diatomic molecules with generalized gradient approximations: The role of the exchange functional. *J. Chem. Phys.*, 107:7921, 1997.

[170] J. M. Pérez-Jordá, E. San-Fabián, and A. J. Pérez-Jiménez. Density-functional study of van der Waals forces on rare-gas diatomics: Hartree–Fock exchange. *J. Chem. Phys.*, 110:1916, 1999.

[171] J. A. White and D. M. Bird. Implementation of gradient-corrected exchange-correlation potentials in Car-Parrinello total-energy calculations. *Phys. Rev. B*, 50:4954, 1994.

[172] A. J. Austin, M. J. Frisch, J. A. Montgomery, Jr., and G. A. Petersson. An overlap criterion for selection of core orbitals. *Theor. Chem. Acc.*, 107:180, 2002.

[173] J. M. L. Martin. On the effect of core correlation on the geometry and harmonic frequencies of small polyatomic molecules. *Chem. Phys. Lett.*, 242:343, 1995.

[174] F. Haase and R. Ahlrichs. Semidirect MP2 Gradient Evaluation on Workstation Computers: The MPGRAD Program. *J. Comput. Chem.*, 14:907, 1993.

[175] A. Schäfer, H. Horn, and R. Ahlrichs. Fully optimized contracted Gaussian basis sets for atoms Li to Kr. *J. Chem. Phys.*, 97:2571, 1992.

[176] H.-J. Werner, P. J. Knowles, R. Lindh, M. Schütz, P. Celani, T. Korona, F. R. Manby, G. Rauhut, R. D. Amos, A. Bernhardsson, A. Berning, D. L. Cooper, M. J. O. Deegan, A. J. Dobbyn, F. Eckert, C. Hampel, G. Hetzer, A. W. Lloyd, S. J. McNicholas, W. Meyer, M. E. Mura, A. Nicklass, P. Palmieri, R. Pitzer, U. Schumann, H. Stoll, A. J. Stone, R. Tarroni, and T. Thorsteinsson. *MOLPRO – a package of ab initio programs (version 2002.6)*. Birmingham, UK, 2003. (see also `http://www.molpro.net`).

[177] D. E. Woon and T. H. Dunning, Jr. Gaussian basis sets for use in correlated molecular calculations. III. The atoms aluminum through argon. *J. Chem. Phys.*, 98:1358, 1993.

[178] D. E. Woon and T. H. Dunning, Jr. Gaussian basis sets for use in correlated molecular calculations. V. Core-valence basis sets for boron through neon. *J. Chem. Phys.*, 103:4572, 1995.

[179] K. A. Peterson and T. H. Dunning, Jr. Accurate correlation consistent basis sets for molecular core-valence correlation effects: The second row atoms Al–Ar, and the first row atoms B–Ne revisited. *J. Chem. Phys.*, 117:10548, 2002.

[180] High Performance Computational Chemistry Group. *NWChem, A Computational Chemistry Package for Parallel Computers (version 4.1)*. Pacific Northwest National Laboratory, Richland, Washington 99352, USA, 2002. (see also `http://www.emsl.pnl.gov/docs/nwchem/nwchem.html`).

[181] J. L. Whitten. Coulombic potential energy integrals and approximations. *J. Chem. Phys.*, 58:4496, 1973.

[182] B. I. Dunlap, J. W. D. Connolly, and J. R. Sabin. On first-row diatomic molecules and local density models. *J. Chem. Phys.*, 71:4993, 1979.

[183] D. M. Schrader and S. Prager. Use of Electrostatic Variation Principles in Molecular Energy Calculations. *J. Chem. Phys.*, 37:1456, 1962.

[184] C. van Alsenoy. *Ab initio* calculations on large molecules: The multiplicative integral approximation. *J. Comput. Chem.*, 9:620, 1988.

[185] E. J. Baerends, D. E. Ellis, and P. Ros. Self-consistent molecular Hartree-Fock-Slater calculations I. The computational procedure. *Chem. Phys.*, 2:41, 1973.

[186] R. A. Kendall and H. A. Früchtl. The impact of the resolution of the identity approximate integral method on modern ab initio algorithm development. *Theor. Chem. Acc.*, 97:158, 1997.

[187] B. I. Dunlap. Robust and variational fitting. *Phys. Chem. Chem. Phys.*, 2:2113, 2000.

[188] R. Ahlrichs. Efficient evaluation of three-center two-electron integrals over Gaussian functions. *Phys. Chem. Chem. Phys.*, 6:5119, 2004.

[189] Y. Jung, A. Sodt, P. M. W. Gill, and M. Head-Gordon. Auxiliary basis expansions for large-scale electronic structure calculations. *Proc. Natl. Acad. Sci. U.S.A.*, 102:6692, 2005.

[190] J. Andzelm and E. Wimmer. Density functional Gaussian-type-orbital approach to molecular geometries, vibrations, and reaction energies. *J. Chem. Phys.*, 96:1280, 1992.

[191] A. Komornicki and G. Fitzgerald. Molecular gradients and hessians implemented in density functional theory. *J. Chem. Phys.*, 98:1398, 1993.

[192] K. Eichkorn, O. Treutler, H. Öhm, M. Häser, and R. Ahlrichs. Auxiliary basis sets to approximate Coulomb potentials. *Chem. Phys. Lett.*, 240:283, 1995. Erratum: *Chem. Phys. Lett.*, 242:652,1995.

[193] F. R. Manby, P. J. Knowles, and A. W. Lloyd. The Poisson equation in density fitting for the Kohn-Sham Coulomb problem. *J. Chem. Phys.*, 115:9144, 2001.

[194] C.-K. Skylaris, L. Gagliardi, N. C. Handy, A. G. Ioannou, S. Spencer, and A. Willetts. On the resolution of identity Coulomb energy approximation in density functional theory. *J. Mol. Struct. (Theochem)*, 501–502:229, 2000.

[195] O. Vahtras, J. Almlöf, and M. W. Feyereisen. Integral approximations for LCAO-SCF calculations. *Chem. Phys. Lett.*, 213:514, 1993.

[196] H. A. Früchtl, R. A. Kendall, R. J. Harrison, and K. G. Dyall. An Implementation of RI-SCF on Parallel Computers. *Int. J. Quantum Chem.*, 64:63, 1997.

[197] F. Weigend. A fully direct RI-HF algorithm: Implementation, optimised auxiliary basis sets, demonstration of accuracy and efficiency. *Phys. Chem. Chem. Phys.*, 4:4285, 2002.

[198] H.-J. Werner, F. R. Manby, and P. J. Knowles. Fast linear scaling second-order Møller-Plesset perturbation theory (MP2) using local and density fitting approximations. *J. Chem. Phys.*, 118:8149, 2003.

[199] R. Polly, H.-J. Werner, F. R. Manby, and P. J. Knowles. Fast Hartree-Fock theory using local density fitting approximations. *Mol. Phys.*, 102:2311, 2004.

[200] S. Ten-no and S. Iwata. Multiconfiguration self-consistent field procedure employing linear combination of atomic-electron distributions. *J. Chem. Phys.*, 105:3604, 1996.

[201] M. Feyereisen, G. Fitzgerald, and A. Komornicki. Use of approximate integrals in ab initio theory. An application in MP2 energy calculations. *Chem. Phys. Lett.*, 208:359, 1993.

[202] D. E. Bernholdt and R. J. Harrison. Large-scale correlated electronic structure calculations: the RI-MP2 method on parallel computers. *Chem. Phys. Lett.*, 250:477, 1996.

[203] F. Weigend and M. Häser. RI-MP2: first derivatives and global consistency. *Theor. Chem. Acc.*, 97:331, 1997.

[204] S. Grimme and M. Waletzke. Multi-reference Møller-Plesset theory: computational strategies for large molecules. *Phys. Chem. Chem. Phys.*, 2:2075, 2000.

[205] M. Schütz, H.-J. Werner, R. Lindh, and F. R. Manby. Analytical energy gradients for local second-order Møller-Plesset perturbation theory using density fitting approximations. *J. Chem. Phys.*, 121:737, 2004.

[206] A. P. Rendell and T. J. Lee. Coupled-cluster theory employing approximate integrals: An approach to avoid the input/output and storage bottlenecks. *J. Chem. Phys.*, 101:400, 1994.

[207] C. Hättig and F. Weigend. CC2 excitation energy calculations on large molecules using the resolution of the identity approximation. *J. Chem. Phys.*, 113:5154, 2000.

[208] M. Schütz and F. R. Manby. Linear scaling local coupled cluster theory with density fitting. Part I: 4-external integrals. *Phys. Chem. Chem. Phys.*, 5:3349, 2003.

[209] D. E. Bernholdt and R. J. Harrison. Fitting basis sets for the RI-MP2 approximate second-order many-body perturbation theory method. *J. Chem. Phys.*, 109:1593, 1998.

[210] F. Weigend, M. Häser, H. Patzelt, and R. Ahlrichs. RI-MP2: optimized auxiliary basis sets and demonstration of efficiency. *Chem. Phys. Lett.*, 294:143, 1998.

[211] F. Weigend, A. Köhn, and C. Hättig. Efficient use of the correlation consistent basis sets in resolution of the identity MP2 calculations. *J. Chem. Phys.*, 116:3175, 2002.

[212] C. Hättig. Optimization of auxiliary basis sets for RI-MP2 and RI-CC2 calculations: Core-valence and quintuple-ζ basis sets for H to Ar and QZVPP basis sets for Li to Kr. *Phys. Chem. Chem. Phys.*, 7:59, 2005.

[213] C. Hättig, A. Hellweg, and A. Köhn. Distributed memory parallel implementation of energies and gradients for second-order Møller–Plesset perturbation theory with the resolution-of-the-identity approximation. *Phys. Chem. Chem. Phys.*, 8:1159, 2006.

[214] N. C. Handy and H. F. Schaefer, III. On the evaluation of analytic energy derivatives for correlated wave functions. *J. Chem. Phys.*, 81: 5031, 1984.

[215] M. Schütz, G. Hetzer, and H.-J. Werner. Low-order scaling local electron correlation methods. I. Linear scaling local MP2. *J. Chem. Phys.*, 111:5691, 1999.

[216] M. S. Lee, P. E. Maslen, and M. Head-Gordon. Closely approximating second-order Møller–Plesset perturbation theory with a local triatomics in molecules model. *J. Chem. Phys.*, 112:3592, 2000.

[217] P. Y. Ayala and G. E. Scuseria. Linear scaling second-order Møller–Plesset theory in the atomic orbital basis for large molecular systems. *J. Chem. Phys.*, 110:3660, 1999.

[218] K. Ishimura, P. Pulay, and S. Nagase. A New Parallel Algorithm of MP2 Energy Calculations. *J. Comput. Chem.*, 27:407, 2006.

[219] P. Y. Ayala, K. N. Kudin, and G. E. Scuseria. Atomic orbital Laplace-transformed second-order Møller–Plesset theory for periodic systems. *J. Chem. Phys.*, 115:9698, 2001.

[220] C. Pisani, G. Capecchi, S. Casassa, and L. Maschio. Computational aspects of a local-MP2 treatment of electron correlation in periodic systems: SiC vs BeS. *Mol. Phys.*, 103:2527, 2005.

[221] C. Pisani, M. Busso, G. Capecchi, S. Casassa, R. Dovesi, L. Maschio, C. Zicovich-Wilson, and M. Schütz. Local-MP2 electron correlation method for nonconducting crystals. *J. Chem. Phys.*, 122:094113, 2005.

[222] T. Helgaker, W. Klopper, H. Koch, and J. Noga. Basis-set convergence of correlated calculations on water. *J. Chem. Phys.*, 106:9639, 1997.

[223] A. Halkier, T. Helgaker, P. Jørgensen, W. Klopper, H. Koch, J. Olsen, and A. K. Wilson. Basis-set convergence in correlated calculations on Ne, N_2, and H_2O. *Chem. Phys. Lett.*, 286:243, 1998.

[224] D. W. Schwenke. The extrapolation of one-electron basis sets in electronic structure calculations: How it should work and how it can be made to work. *J. Chem. Phys.*, 122:014107, 2005.

[225] S. Y. Park and J. S. Lee. Basis set limit binding energies of dimers derived from basis set convergence of monomer energies. *J. Chem. Phys.*, 116:5389, 2002.

[226] D. E. Woon and T. H. Dunning, Jr. Benchmark calculations with correlated molecular wave functions. I. Multireference configuration interaction calculations for the second row diatomic hydrides. *J. Chem. Phys.*, 99:1914, 1993.

[227] A. Halkier, W. Klopper, T. Helgaker, P. Jørgensen, and P. R. Taylor. Basis set convergence of the interaction energy of hydrogen-bonded complexes. *J. Chem. Phys.*, 111:9157, 1999.

[228] A. Halkier, H. Koch, P. Jørgensen, O. Christiansen, I. M. Beck Nielsen, and T. Helgaker. A systematic ab initio study of the water dimer in hierarchies of basis sets and correlation models. *Theor. Chem. Acc.*, 97:150, 1997.

[229] D. Feller. Application of systematic sequences of wave functions to the water dimer. *J. Chem. Phys.*, 96:6104, 1992.

[230] K. A. Peterson and T. H. Dunning, Jr. Benchmark calculations with correlated molecular wavefunctions. VII. Binding energy and structure of the HF dimer. *J. Chem. Phys.*, 102:2032, 1995.

[231] M. Masamura. The effect of basis set superposition error on the convergence of interaction energies. *Theor. Chem. Acc.*, 106:301, 2001.

[232] D. E. Woon and T. H. Dunning, Jr. Gaussian basis sets for use in correlated molecular calculations. IV. Calculation of static electrical response properties. *J. Chem. Phys.*, 100:2975, 1994.

[233] C. Tuma and J. Sauer. A hybrid MP2/planewave-DFT scheme for large chemical systems: proton jumps in zeolites. *Chem. Phys. Lett.*, 387:388, 2004.

[234] L'. Benco, Th. Demuth, J. Hafner, and F. Hutschka. Spontaneous proton transfer between O-sites in zeolites. *Chem. Phys. Lett.*, 324: 373, 2000.

[235] J. T. Fermann, C. Blanco, and S. Auerbach. Modeling proton mobility in acidic zeolite clusters. I. Convergence of transition state parameters from quantum chemistry. *J. Chem. Phys.*, 112:6779, 2000.

[236] J. A. Ryder, A. K. Chakraborty, and A. T. Bell. Density Functional Theory Study of Proton Mobility in Zeolites: Proton Migration and Hydrogen Exchange in ZSM-5. *J. Phys. Chem. B*, 104:6998, 2000.

[237] M. Sierka and J. Sauer. Proton Mobility in Chabazite, Faujasite, and ZSM-5 Zeolite Catalysts. Comparison Based on ab Initio Calculations. *J. Phys. Chem. B*, 105:1603, 2001.

[238] M. Krossner and J. Sauer. Interaction of Water with Brønsted Acidic Sites of Zeolite Catalysts. Ab Initio Study of 1:1 and 2:1 Surface Complexes. *J. Phys. Chem.*, 100:6199, 1996.

[239] S. A. Zygmunt, L. A. Curtiss, L. E. Iton, and M. K. Erhardt. Computational Studies of Water Adsorption in the Zeolite H-ZSM-5. *J. Phys. Chem.*, 100:6663, 1996.

[240] A. M. Vos, F. De Proft, R. A. Schoonheydt, and P. Geerlings. Calculation of reaction rate constants for hydrogen-deuterium exchange reactions of methane catalysed by acid zeolites. *Chem. Commun.*, 12: 1108, 2001.

[241] A. H. de Vries, P. Sherwood, S. J. Collins, A. M. Rigby, M. Rigutto, and G. J. Kramer. Zeolite Structure and Reactivity by Combined Quantum-Chemical–Classical Calculations. *J. Phys. Chem. B*, 103: 6133, 1999.

[242] J. T. Fermann, T. Moniz, O. Kiowski, T. J. McIntire, S. M. Auerbach, T. Vreven, and M. J. Frisch. Modeling Proton Transfer in Zeolites: Convergence Behavior of Embedded and Constrained Cluster Calculations. *J. Chem. Theory Comput.*, 1:1232, 2005.

[243] M. Calligaris, G. Nardin, L. Randaccio, and P. Comin-Chiaramonti. Cation-Site Location in a Natural Chabazite. *Acta Cryst. B*, 38:602, 1982.

[244] S. I. Zones and R. A. Van Nordstrand. Novel zeolite transformations: The template-mediated conversion of Cubic P zeolite to SSZ-13. *Zeolites*, 8:166, 1988.

[245] S. I. Zones. Conversion of Faujasites to High-silica Chabazite SSZ-13 in the Presence of *N,N,N*-Trimethyl-1-adamantammonium Iodide. *J. Chem. Soc. Faraday Trans.*, 87:3709, 1991.

[246] S. Bordiga, L. Regli, D. Cocina, C. Lamberti, M. Bjørgen, and K. P. Lillerud. Assessing the Acidity of High Silica Chabazite H–SSZ-13 by FTIR Using CO as Molecular Probe: Comparison with H–SAPO-34. *J. Phys. Chem. B*, 109:2779, 2005.

[247] L. J. Smith, A. Davidson, and A. K. Cheetham. A neutron diffraction and infrared spectroscopy study of the acid form of the aluminosilicate zeolite, chabazite (H-SSZ-13). *Catal. Lett.*, 49:143, 1997.

[248] R. Shah, J. D. Gale, and M. C. Payne. Methanol Adsorption in Zeolites – A First-Principles Study. *J. Phys. Chem.*, 100:11688, 1996.

[249] R. Shah, J. D. Gale, and M. C. Payne. The active sites of microporous solid acid catalysts. *Phase Transitions*, 61:67, 1997.

[250] Y. Jeanvoine, J. G. Ángyán, G. Kresse, and J. Hafner. Brønsted Acid Sites in HSAPO-34 and Chabazite: An Ab Initio Structural Study. *J. Phys. Chem. B*, 102:5573, 1998.

[251] F. Haase, J. Sauer, and J. Hutter. Ab initio molecular dynamics simulation of methanol adsorbed in chabazite. *Chem. Phys. Lett.*, 266:397, 1997.

[252] M. Brändle, J. Sauer, R. Dovesi, and N. M. Harrison. Comparison of a combined quantum mechanics/interatomic potential function approach with its periodic quantum-mechanical limit: Proton siting and ammonia adsorption in zeolite chabazite. *J. Chem. Phys.*, 109: 10379, 1998.

[253] P. Ugliengo, B. Civalleri, C. M. Zicovich-Wilson, and R. Dovesi. H-Chabazite with variable Si/Al ratio: stability and OH vibrational frequency computed in a periodic LCAO B3-LYP approach. *Chem. Phys. Lett.*, 318:247, 2000.

[254] V. V. Mihaleva, R. A. van Santen, and A. P. J. Jansen. A DFT Study of Methanol Adsorption in 8T Rings of Chabazite. *J. Phys. Chem. B*, 105:6874, 2001.

[255] V. V. Mihaleva, R. A. van Santen, and A. P. J. Jansen. The heterogeneity of the hydroxyl groups in chabazite. *J. Chem. Phys.*, 119: 13053, 2003.

[256] P. Treesukol, J. P. Lewis, J. Limtrakul, and T. N. Truong. A full quantum embedded cluster study of proton siting in chabazite. *Chem. Phys. Lett.*, 350:128, 2001.

[257] B. Civalleri, A. M. Ferrari, M. Llunell, R. Orlando, M. Mérawa, and P. Ugliengo. Cation Selectivity in Alkali-Exchanged Chabazite: An ab Initio Periodic Study. *Chem. Mater.*, 15:3996, 2003.

[258] M. Sierka and J. Sauer. Structure and reactivity of silica and zeolite catalysts by a combined quantum mechanics–shell-model potential approach based on DFT. *Faraday Discuss.*, 106:41, 1997.

[259] I.-F. W. Kuo and C. J. Mundy. An ab Initio Molecular Dynamics Study of the Aqueous Liquid-Vapor Interface. *Science*, 303:658, 2004.

[260] P. L. Geissler, C. Dellago, D. Chandler, J. Hutter, and M. Parrinello. Ab initio analysis of proton transfer dynamics in $(H_2O)_3H^+$. *Chem. Phys. Lett.*, 321:225, 2000.

[261] D. M. Sullivan, K. Bagchi, M. E. Tuckerman, and M. L. Klein. Ab Initio Molecular Dynamics Study of Crystalline Nitric Acid Trihydrate. *J. Phys. Chem. A*, 103:8678, 1999.

[262] I. Frank, J. Hutter, D. Marx, and M. Parrinello. Molecular dynamics in low-spin excited states. *J. Chem. Phys.*, 108:4060, 1998.

[263] J. Ireta, J. Neugebauer, M. Scheffler, A. Rojo, and M. Galván. Density Functional Theory Study of the Cooperativity of Hydrogen Bonds in Finite and Infinite α-Helices. *J. Phys. Chem. B*, 107:1432, 2003.

[264] J. Ireta, J. Neugebauer, and M. Scheffler. On the Accuracy of DFT for Describing Hydrogen Bonds: Dependence on the Bond Directionality. *J. Phys. Chem. A*, 108:5692, 2004.

[265] X. Solans-Monfort, M. Sodupe, V. Branchadell, J. Sauer, R. Orlando, and P. Ugliengo. Adsorption of NH_3 and H_2O in Acidic Chabazite. Comparison of ONIOM Approach with Periodic Calculations. *J. Phys. Chem. B*, 109:3539, 2005.

[266] J. Sauer, P. Ugliengo, E. Garrone, and V. R. Saunders. Theoretical Study of van der Waals Complexes at Surface Sites in Comparison with the Experiment. *Chem. Rev.*, 94:2095, 1994.

[267] P. Ugliengo and A. Damin. Are dispersive forces relevant for CO adsorption on the MgO(001) surface? *Chem. Phys. Lett.*, 366:683, 2002.

[268] C. Tuma and J. Sauer. Protonated Isobutene in Zeolites: *tert*-Butyl Cation or Alkoxide? *Angew. Chem. Int. Ed.*, 44:4769, 2005.

[269] C. Tuma and J. Sauer. Treating dispersion effects in extended systems by hybrid MP2:DFT calculations—protonation of isobutene in zeolite ferrierite. *Phys. Chem. Chem. Phys.*, 8:3955, 2006.

[270] G. A. Olah, G. K. S. Prakash, and J. Sommer. *Superacids*. Wiley, New York, 1985. ISBN 0-471-88469-3.

[271] P. A. Jacobs. *Carboniogenic Activity of Zeolites*. Elsevier, New York, 1977. ISBN 0-444-41556-4.

[272] T. Xu, J. Zhang, E. J. Munson, and J. F. Haw. A Report of a Persistent Allyl Cation on H-ZSM-5 Zeolite was due to Propanal. *J. Chem. Soc. Chem. Commun.*, page 2733, 1994.

[273] J. F. Haw, J. B. Nicholas, T. Xu, L. W. Beck, and D. B. Ferguson. Physical Organic Chemistry of Solid Acids: Lessons from in Situ NMR and Theoretical Chemistry. *Acc. Chem. Res.*, 29:259, 1996.

[274] M. T. Aronson, R. J. Gorte, W. E. Farneth, and D. White. ^{13}C NMR Identification of Intermediates Formed by 2-Methyl-2-propanol Adsorption in H-ZSM-5. *J. Am. Chem. Soc.*, 111:840, 1989.

[275] J. F. Haw, B. R. Richardson, I. S. Oshiro, N. D. Lazo, and J. A. Speed. Reactions of Propene on Zeolite HY Catalyst Studied by in Situ Variable-Temperature Solid-State Nuclear Magnetic Resonance Spectroscopy. *J. Am. Chem. Soc.*, 111:2052, 1989.

[276] N. D. Lazo, B. R. Richardson, P. D. Schettler, J. L. White, E. J. Munson, and J. F. Haw. In Situ Variable-Temperature MAS ^{13}C NMR Study of the Reactions of Isobutylene in Zeolites HY and HZSM-5. *J. Phys. Chem.*, 95:9420, 1991.

[277] A. G. Stepanov, K. I. Zamaraev, and J. M. Thomas. ^{13}C CP/MAS and ^{2}H NMR study of tert-butyl alcohol dehydration on H-ZSM-5 zeolite. Evidence for the formation of tert-butyl cation and tert-butyl silyl ether intermediates. *Catal. Lett.*, 13:407, 1992.

[278] V. B. Kazansky and I. N. Senchenya. Quantum Chemical Study of the Electronic Structure and Geometry of Surface Alkoxy Groups as Probable Active Intermediates of Heterogeneous Acidic Catalysts: What Are the Adsorbed Carbenium Ions? *J. Catal.*, 119:108, 1989.

[279] I. N. Senchenya and V. B. Kazansky. Quantum chemical studies of ethylene interaction with zeolite OH-groups. *Catal. Lett.*, 8:317, 1991.

[280] V. B. Kazansky. The Nature of Adsorbed Carbenium Ions as Active Intermediates in Catalysis by Solid Acids. *Acc. Chem. Res.*, 24:379, 1991.

[281] P. Viruela-Martín, C. M. Zicovich-Wilson, and A. Corma. Ab Initio Molecular Orbital Calculations of the Protonation Reaction of Propylene and Isobutene by Acidic OH Groups of Isomorphously Substituted Zeolites. *J. Phys. Chem.*, 97:13713, 1993.

[282] V. B. Kazansky, M. V. Frash, and R. A. van Santen. Quantumchemical study of the isobutane cracking on zeolites. *Appl. Catal. A Gen.*, 146:225, 1996.

[283] J. F. Haw. Zeolite acid strength and reaction mechanisms in catalysis. *Phys. Chem. Chem. Phys.*, 4:5431, 2002.

[284] C. Pazè, B. Sazak, A. Zecchina, and J. Dwyer. FTIR and UV–Vis Spectroscopic Study of Interaction of 1-Butene on H–Ferrierite Zeolite. *J. Phys. Chem. B*, 103:9978, 1999.

[285] W. Adam, I. Casades, V. Fornés, H. García, and O. Weichold. UV–vis and IR Spectral Characterization of Persistent Carbenium Ions, Generated upon Incorporation of Cinnamyl Alcohols in the Acid Zeolites HZSM-5 and HMor. *J. Org. Chem.*, 65:3947, 2000.

[286] M. Bjørgen, F. Bonino, S. Kolboe, K.-P. Lillerud, A. Zecchina, and S. Bordiga. Spectroscopic Evidence for a Persistent Benzenium Cation in Zeolite H-Beta. *J. Am. Chem. Soc.*, 125:15863, 2003.

[287] S. Yang, J. N. Kondo, and K. Domen. Simultaneous Observation of Alkenyl Carbenium Ions and Alkoxy Species on HZSM-5 Zeolite by Adsorption of 1-Methylcyclopentene and 1-Methylcyclopentanol. *J. Phys. Chem. B*, 105:7878, 2001.

[288] S. Yang, J. N. Kondo, and K. Domen. Formation of alkenyl carbenium ions by adsorption of cyclic precursors on zeolites. *Catal. Today*, 73:113, 2002.

[289] L. A. Clark, M. Sierka, and J. Sauer. Stable Mechanistically-Relevant Aromatic-Based Carbenium Ions in Zeolite Catalysts. *J. Am. Chem. Soc.*, 125:2136, 2003.

[290] L. A. Clark, M. Sierka, and J. Sauer. Computational Elucidation of the Transition State Shape Selectivity Phenomenon. *J. Am. Chem. Soc.*, 126:936, 2004.

[291] M. Boronat, P. M. Viruela, and A. Corma. Reaction Intermediates in Acid Catalysis by Zeolites: Prediction of the Relative Tendency To Form Alkoxides or Carbocations as a Function of Hydrocarbon Nature and Active Site Structure. *J. Am. Chem. Soc.*, 126:3300, 2004.

[292] G. A. Olah. My Search for Carbocations and Their Role in Chemistry (Nobel Lecture). *Angew. Chem. Int. Ed. Engl.*, 34:1393, 1995.

[293] G. A. Olah. 100 Years of Carbocations and Their Significance in Chemistry. *J. Org. Chem.*, 66:5943, 2001.

[294] S. Hollenstein and T. Laube. Crystal Structure of the *tert*-Butyl Cation. *J. Am. Chem. Soc.*, 115:7240, 1993.

[295] T. Kato and C. A. Reed. Putting *tert*-Butyl Cation in a Bottle. *Angew. Chem. Int. Ed.*, 43:2907, 2004.

[296] P. E. Sinclair, A. de Vries, P. Sherwood, C. R. A. Catlow, and R. A. van Santen. Quantum-chemical studies of alkene chemisorption in chabazite: A comparison of cluster and embedded-cluster models. *J. Chem. Soc. Faraday Trans.*, 94:3401, 1998.

[297] M. Boronat, P. Viruela, and A. Corma. The skeletal isomerization of but-1-ene catalyzed by theta-1 zeolite. *Phys. Chem. Chem. Phys.*, 3: 3235, 2001.

[298] M. Boronat, C. M. Zicovich-Wilson, P. Viruela, and A. Corma. Influence of the Local Geometry of Zeolite Active Sites and Olefin Size on the Stability of Alkoxide Intermediates. *J. Phys. Chem. B*, 105: 11169, 2001.

[299] X. Rozanska, R. A. van Santen, T. Demuth, F. Hutschka, and J. Hafner. A Periodic DFT Study of Isobutene Chemisorption in Proton-Exchanged Zeolites: Dependence of Reactivity on the Zeolite Framework Structure. *J. Phys. Chem. B*, 107:1309, 2003.

[300] M. Trombetta, G. Busca, S. Rossini, V. Piccoli, and U. Cornaro. FT-IR Studies on Light Olefin Skeletal Isomerization Catalysis. II. The Interaction of C4 Olefins and Alcohols with HZSM5 Zeolite. *J. Catal.*, 168:349, 1997.

[301] H. Ishikawa, E. Yoda, J. N. Kondo, F. Wakabayashi, and K. Domen. Stable Dimerized Alkoxy Species of 2-Methylpropene on Mordenite Zeolite Studied by FT-IR. *J. Phys. Chem. B*, 103:5681, 1999.

[302] J. N. Kondo, H. Ishikawa, E. Yoda, F. Wakabayashi, and K. Domen. Structure of Dimerized Alkoxy Species of 2-Methylpropene on Zeolites and Silica–Alumina Studied by FT-IR. *J. Phys. Chem. B*, 103: 8538, 1999.

[303] J. N. Kondo, E. Yoda, H. Ishikawa, F. Wakabayashi, and K. Domen. Acid Property of Silanol Groups on Zeolites Assessed by Reaction Probe IR Study. *J. Catal.*, 191:275, 2000.

[304] J. Hafner, L. Benco, and T. Bučko. Acid-based catalysis in zeolites investigated by density-functional methods. *Top. Catal.*, 37:41, 2006.

[305] K. Raghavachari, G. W. Trucks, J. A. Pople, and M. Head-Gordon. A fifth-order perturbation comparison of electron correlation theories. *Chem. Phys. Lett.*, 157:479, 1989.

[306] R. J. Darton, P. Wormald, and R. E. Morris. Variable temperature high resolution ^{29}Si MAS NMR of siliceous zeolite ferrierite. *J. Mater. Chem.*, 14:2036, 2004.

[307] A. Martucci, A. Alberti, G. Cruciani, P. Radaelli, P. Ciambelli, and M. Rapacciulo. Location of Brønsted sites in D-ferrierite by neutron powder diffraction. *Micropor. Mesopor. Mat.*, 30:95, 1999.

[308] Y. Yokomori, J. Wachsmuth, and K. Nishi. Structure and Brønsted acid sites of ferrierite. *Micropor. Mesopor. Mat.*, 50:137, 2001.

[309] P. Sarv, B. Wichterlová, and J. Čejka. Multinuclear MQMAS NMR Study of NH_4/Na-Ferrierites. *J. Phys. Chem. B*, 102:1372, 1998.

[310] V. L. Zholobenko, D. B. Lukyanov, J. Dwyer, and W. J. Smith. Ferrierite and SUZ-4 Zeolite: Characterization of Acid Sites. *J. Phys. Chem. B*, 102:2715, 1998.

[311] V. Nieminen, M. Sierka, D. Yu. Murzin, and J. Sauer. Stabilities of C_3–C_5 alkoxide species inside H-FER zeolite: a hybrid QM/MM study. *J. Catal.*, 231:393, 2005.

[312] P. A. Vaughan. The Crystal Structure of the Zeolite Ferrierite. *Acta Cryst.*, 21:983, 1966.

[313] F. Jousse, L. Leherte, and D. P. Vercauteren. Molecular mechanical investigation of the energetics of butene sorbed in H-ferrierite. *Mol. Simul.*, 17:175, 1996.

[314] F. Blanco, G. Urbina-Villalba, and M. M. Ramírez de Agudelo. Theoretical calculations on zeolites: The aluminium substitution in mordenite, ferrierite and ZSM-5. *Mol. Simul.*, 14:165, 1995.

[315] L. Domokos, L. Lefferts, K. Seshan, and J. A. Lercher. The importance of acid site locations for *n*-butene skeletal isomerization on ferrierite. *J. Mol. Catal. A Chem.*, 162:147, 2000.

[316] L. Domokos, L. Lefferts, K. Seshan, and J. A. Lercher. Isomerization of Linear Butenes to iso-Butene over Medium Pore Zeolites. *J. Catal.*, 197:68, 2001.

[317] S. van Donk, E. Bus, A. Broersma, J. H. Bitter, and K. P. de Jong. Butene skeletal isomerization over H-ferrierite: a TEOM and in situ IR study on the role of carbonaceous deposits and the location of Brønsted acid sites. *Appl. Catal. A Gen.*, 237:149, 2002.

[318] B. de Ménorval, P. Ayrault, N. S. Gnep, and M. Guisnet. Mechanism of *n*-butene skeletal isomerization over HFER zeolites: a new proposal. *J. Catal.*, 230:38, 2005.

[319] A. Halkier, T. Helgaker, P. Jørgensen, W. Klopper, and J. Olsen. Basis-set convergence of the energy in molecular Hartree–Fock calculations. *Chem. Phys. Lett.*, 302:437, 1999.

[320] F. Jensen. Estimating the Hartree–Fock limit from finite basis set calculations. *Theor. Chem. Acc.*, 113:267, 2005.

[321] C. Hättig. Geometry optimizations with the coupled-cluster model CC2 using the resolution-of-the-identity approximation. *J. Chem. Phys.*, 118:7751, 2003.

[322] C. Li and Z. Wu. Microporous Materials Characterized by Vibrational Spectroscopies. In S. M. Auerbach, K. A. Carrado, and P. K.

Dutta, editors, *Handbook of Zeolite Science and Technology*, chapter 11. Marcel Dekker, Inc., New York, 2003. ISBN 0-8247-4020-3.

[323] K. Onda, K. Tanabe, H. Noguchi, K. Domen, and A. Wada. Dynamic Processes of Olefins Adsorbed on Hydroxyl Groups of DM20 Zeolite Excited by Picosecond Infrared Pulses: Vibrational Relaxation, Short-Lived Species and Desorption. *J. Phys. Chem. B*, 107:11391, 2003.

[324] H. Noguchi, E. Yoda, N. Ishizawa, J. N. Kondo, A. Wada, H. Kobayashi, and K. Domen. Direct Observation of Unstable Intermediate Species in the Reaction of *trans*-2-Butene on Ferrierite Zeolite by Picosecond Infrared Laser Spectroscopy. *J. Phys. Chem. B*, 109:17217, 2005.

[325] D. Feller. Strength of the Benzene–Water Hydrogen Bond. *J. Phys. Chem. A*, 103:7558, 1999.

[326] F. Eder and J. A. Lercher. On the Role of the Pore Size and Tortuosity for Sorption of Alkanes in Molecular Sieves. *J. Phys. Chem. B*, 101: 1273, 1997.

[327] E. Yoda, J. N. Kondo, and K. Domen. Detailed Process of Adsorption of Alkanes and Alkenes on Zeolites. *J. Phys. Chem. B*, 109:1464, 2005.

Appendix A

VIBRATIONAL FREQUENCIES

A.1 THE SYSTEM CHABAZITE/(WATER)

(see Chapter 3 for details; all numbers in cm^{-1})

- water (H_2O, 3 vibrational modes)

  PBE, 70 Ry:
  3694, 3583, 1593

  PBE, 100 Ry:
  3814, 3702, 1592

  MP2/PBE, basis set A:
  3938, 3806, 1622

- structure **a** ($HAlSi_{11}O_{24}$, 108 vibrational modes)

  PBE, 70 Ry:
  3584, 1190, 1180, 1164, 1158, 1152, 1144, 1143, 1138, 1129, 1120, 1084, 1056, 1046, 1040, 1035, 1031, 1026, 1023, 1018, 1017, 1012, 1010, 1001, 996, 799, 784, 769, 765, 761, 757, 751, 749, 746, 744, 740, 708, 692, 652, 645, 622, 611, 600, 591, 552, 540, 515, 513, 489, 471, 470, 466, 465, 460, 450, 444, 437, 432, 408, 406, 402, 398, 396, 389, 384, 381, 372, 364, 354, 345, 338, 334, 329, 323, 318, 311, 311, 303, 298, 296, 289, 282, 275, 273, 262, 256, 253, 241, 233, 217, 196, 188, 183, 178, 169, 162, 159, 150, 135, 132, 128, 125, 113, 108, 93, 89, 63, 54

  PBE, 100 Ry:
  3697, 1187, 1177, 1161, 1153, 1147, 1139, 1137, 1133, 1125, 1116, 1079, 1055, 1045, 1036, 1033, 1026, 1020, 1018, 1014, 1010, 1006, 1004, 1000, 996, 789, 780, 770, 766, 761, 758, 751,

749, 745, 744, 740, 706, 691, 650, 643, 620, 610, 598, 591, 551, 538, 513, 511, 493, 473, 466, 461, 459, 455, 446, 438, 437, 434, 411, 408, 400, 396, 395, 385, 383, 382, 373, 358, 351, 350, 338, 336, 326, 322, 319, 312, 302, 299, 296, 294, 289, 284, 280, 272, 267, 261, 252, 247, 238, 214, 195, 189, 186, 182, 178, 164, 154, 148, 144, 139, 129, 123, 118, 110, 108, 101, 86, 75

MP2/PBE, basis set A:
3787, 1219, 1219, 1190, 1186, 1169, 1160, 1152, 1149, 1145, 1144, 1109, 1102, 1080, 1069, 1063, 1053, 1048, 1031, 1030, 1026, 1024, 1016, 1015, 1006, 832, 799, 780, 772, 768, 764, 763, 759, 754, 751, 747, 745, 739, 670, 664, 650, 624, 616, 608, 578, 564, 540, 537, 530, 509, 500, 492, 482, 476, 471, 463, 463, 455, 451, 442, 425, 422, 418, 413, 409, 398, 397, 390, 388, 373, 369, 366, 361, 351, 349, 344, 339, 331, 323, 321, 316, 311, 309, 305, 295, 289, 282, 275, 255, 251, 238, 232, 216, 214, 209, 201, 187, 176, 168, 165, 155, 148, 145, 140, 130, 123, 101, 10

- structure **b** ($HAlSi_{11}O_{24}$, 108 vibrational modes)

PBE, 70 Ry:
1754, 1179, 1172, 1166, 1155, 1151, 1145, 1141, 1138, 1119, 1110, 1060, 1048, 1039, 1033, 1025, 1023, 1020, 1015, 1014, 1012, 1005, 1000, 990, 979, 841, 783, 768, 765, 762, 757, 754, 750, 749, 743, 742, 713, 682, 660, 644, 617, 613, 602, 587, 574, 554, 527, 518, 512, 472, 467, 464, 461, 455, 449, 442, 439, 434, 417, 406, 403, 401, 399, 398, 392, 378, 376, 366, 353, 350, 344, 331, 323, 322, 317, 311, 306, 303, 299, 296, 289, 286, 283, 279, 272, 261, 242, 240, 234, 200, 188, 181, 179, 171, 166, 164, 154, 146, 143, 136, 135, 121, 112, 103, 88, 82, 78, 1274*i*

PBE, 100 Ry:
1759, 1172, 1170, 1162, 1150, 1144, 1140, 1135, 1130, 1113, 1102, 1054, 1044, 1037, 1027, 1024, 1015, 1014, 1009, 1008, 1005, 1000, 990, 980, 978, 836, 784, 768, 766, 763, 758, 755, 751, 749, 743, 741, 712, 680, 658, 643, 615, 612, 602, 585, 571, 551, 528, 516, 510, 469, 465, 463, 462, 454, 450, 441, 437, 425, 419, 410, 409, 402, 396, 393, 388, 379, 374, 366, 351, 347, 338, 336, 320, 319, 315, 310, 307, 299, 295, 292, 291, 283, 277, 276, 269, 258, 245, 240, 228, 195, 189, 183, 181, 176, 164, 159, 153, 143, 139, 138, 126, 121, 113, 111, 84, 75, 51, 1202*i*

MP2/PBE, basis set A:
1915, 1200, 1193, 1180, 1167, 1165, 1156, 1150, 1149, 1145, 1127, 1101, 1093, 1084, 1064, 1058, 1051, 1037, 1037, 1025, 1023, 1018, 1016, 1011, 1004, 897, 793, 778, 770, 766, 764, 761, 761, 754, 751, 747, 746, 729, 684, 663, 644, 630, 623, 618, 607, 565, 549, 537, 531, 520, 491, 483, 476, 472, 465, 457, 452, 450, 440, 435, 421, 414, 410, 408, 399, 395, 388, 381, 372, 369, 363, 352, 349, 342, 339, 331, 327, 316, 311, 306, 300, 298, 293, 290, 287, 281, 267, 264, 252, 237, 229, 216, 200, 189, 180, 176, 172, 160, 155, 138, 130, 128, 117, 112, 106, 92, 19, 1304*i*

- structure **c** ($HAlSi_{11}O_{24}$, 108 vibrational modes)

  PBE, 70 Ry:
  3555, 1175, 1171, 1167, 1162, 1155, 1149, 1144, 1137, 1123, 1114, 1094, 1055, 1045, 1044, 1035, 1031, 1028, 1025, 1017, 1016, 1014, 1006, 1005, 998, 797, 779, 764, 760, 759, 757, 752, 749, 747, 742, 737, 709, 699, 659, 639, 614, 608, 598, 588, 565, 553, 521, 509, 496, 473, 467, 462, 461, 454, 451, 445, 438, 432, 415, 414, 407, 405, 398, 397, 388, 384, 372, 367, 359, 352, 347, 337, 326, 323, 319, 316, 308, 306, 300, 292, 290, 282, 280, 270, 266, 260, 252, 249, 231, 221, 200, 188, 182, 178, 171, 162, 152, 149, 137, 137, 125, 118, 113, 106, 99, 92, 85, 60

  PBE, 100 Ry:
  3669, 1170, 1167, 1161, 1158, 1152, 1144, 1139, 1132, 1117, 1110, 1090, 1050, 1042, 1039, 1031, 1026, 1021, 1021, 1012, 1011, 1010, 1002, 1000, 997, 793, 778, 764, 761, 760, 757, 753, 748, 747, 744, 736, 708, 699, 659, 637, 613, 606, 598, 584, 565, 550, 521, 512, 496, 471, 463, 457, 456, 454, 446, 443, 438, 437, 418, 410, 404, 400, 398, 395, 390, 385, 374, 365, 354, 353, 350, 332, 326, 319, 314, 313, 310, 306, 297, 293, 292, 282, 280, 278, 268, 265, 256, 241, 234, 223, 196, 187, 183, 179, 173, 163, 161, 159, 152, 140, 130, 125, 120, 112, 107, 99, 83, 72

  MP2/PBE, basis set A:
  3760, 1203, 1194, 1184, 1176, 1170, 1163, 1154, 1149, 1145, 1138, 1109, 1091, 1087, 1066, 1063, 1054, 1051, 1040, 1036, 1033, 1024, 1018, 1016, 1007, 827, 791, 780, 771, 769, 766, 764, 758, 755, 753, 749, 745, 740, 678, 655, 626, 622, 615, 610, 593, 561, 537, 531, 523, 503, 495, 484, 481, 471, 469, 459, 453, 450, 445, 426, 423, 413, 407, 406, 396, 392, 384, 381, 376, 369, 357, 354, 346, 334, 330, 328, 323, 316, 311, 306, 300, 297, 290, 280, 275, 275, 265, 255, 252, 229, 220, 201, 194, 191, 186, 180, 172, 169, 164, 153, 148, 143, 139, 133, 113, 97, 89, 44

- structure **d** ($H_3AlSi_{11}O_{25}$, 117 vibrational modes)

  PBE, 70 Ry:
  3599, 3455, 2375, 1567, 1409, 1185, 1164, 1162, 1153, 1147, 1137, 1132, 1125, 1116, 1114, 1079, 1047, 1039, 1037, 1029, 1026, 1022, 1018, 1013, 1004, 1004, 991, 987, 981, 861, 786, 769, 764, 762, 755, 752, 745, 745, 736, 734, 703, 689, 655, 648, 621, 609, 604, 593, 583, 562, 552, 529, 510, 507, 480, 467, 461, 458, 456, 454, 447, 440, 432, 431, 410, 407, 403, 398, 393, 389, 385, 379, 375, 362, 357, 347, 339, 337, 330, 325, 318, 316, 315, 305, 303, 296, 291, 288, 286, 282, 274, 265, 258, 254, 249, 239, 230, 202, 185, 178, 174, 169, 164, 157, 153, 146, 143, 136, 131, 127, 121, 115, 112, 106, 99, 93, 71

  PBE, 100 Ry:
  3722, 3579, 2411, 1572, 1412, 1180, 1159, 1156, 1147, 1142, 1132, 1125, 1121, 1112, 1109, 1072, 1044, 1038, 1034, 1025, 1022, 1016, 1015, 1008, 998, 996, 987, 977, 975, 846, 787, 770,

765, 763, 756, 752, 746, 745, 735, 734, 702, 688, 653, 643, 619, 609, 598, 592, 577, 557, 544, 524, 510, 504, 473, 466, 462, 461, 459, 450, 444, 438, 435, 424, 406, 403, 402, 400, 394, 390, 386, 381, 373, 363, 351, 342, 337, 334, 332, 329, 321, 313, 308, 306, 301, 297, 289, 286, 282, 278, 271, 263, 254, 247, 239, 228, 216, 194, 192, 189, 187, 179, 174, 168, 162, 154, 146, 136, 133, 130, 122, 108, 103, 99, 94, 76, 66

MP2/PBE, basis set A:

3846, 3699, 2636, 1607, 1474, 1223, 1194, 1183, 1178, 1164, 1155, 1145, 1143, 1142, 1133, 1099, 1095, 1079, 1060, 1049, 1041, 1028, 1027, 1019, 1010, 1008, 1001, 989, 971, 897, 798, 780, 771, 768, 763, 761, 755, 753, 750, 745, 738, 735, 678, 663, 647, 635, 621, 610, 604, 587, 565, 549, 532, 526, 501, 494, 490, 485, 477, 476, 468, 465, 460, 457, 454, 431, 422, 416, 413, 406, 401, 394, 393, 382, 379, 376, 369, 360, 358, 348, 342, 333, 329, 319, 317, 316, 312, 304, 302, 300, 297, 289, 286, 279, 273, 264, 257, 247, 234, 224, 215, 210, 203, 196, 188, 180, 178, 172, 166, 158, 151, 138, 135, 132, 116, 111, 89

- structure **e** ($H_3AlSi_{11}O_{25}$, 117 vibrational modes)

  PBE, 70 Ry:

  3575, 2500, 1818, 1593, 1372, 1282, 1179, 1162, 1160, 1152, 1147, 1143, 1140, 1126, 1109, 1103, 1069, 1047, 1039, 1036, 1031, 1024, 1022, 1017, 1011, 1009, 1008, 994, 954, 929, 784, 767, 765, 762, 758, 756, 749, 746, 743, 741, 726, 706, 676, 665, 644, 615, 610, 602, 583, 570, 566, 562, 531, 528, 509, 505, 491, 466, 464, 463, 457, 452, 445, 434, 424, 412, 410, 406, 404, 399, 397, 395, 389, 380, 375, 362, 351, 349, 337, 329, 326, 320, 316, 314, 308, 299, 296, 291, 288, 283, 275, 270, 269, 255, 246, 239, 223, 196, 191, 190, 182, 176, 170, 161, 152, 143, 140, 131, 127, 120, 116, 115, 110, 100, 98, 88, 251*i*

  PBE, 100 Ry:

  3696, 2391, 1817, 1600, 1366, 1287, 1173, 1156, 1151, 1144, 1139, 1136, 1133, 1119, 1106, 1097, 1065, 1042, 1032, 1029, 1026, 1018, 1014, 1011, 1003, 1002, 999, 986, 953, 938, 786, 768, 766, 762, 759, 756, 750, 746, 743, 741, 722, 705, 675, 665, 643, 613, 609, 602, 585, 570, 568, 558, 534, 528, 510, 506, 494, 470, 464, 460, 456, 453, 447, 436, 428, 416, 410, 404, 404, 400, 396, 394, 391, 380, 372, 363, 356, 349, 333, 331, 329, 320, 316, 313, 307, 298, 295, 291, 285, 281, 279, 274, 261, 250, 250, 239, 224, 198, 192, 190, 187, 181, 177, 165, 157, 152, 146, 140, 137, 130, 125, 115, 109, 103, 90, 77, 283*i*

  MP2/PBE, basis set A:

  3786, 2639, 1967, 1681, 1463, 1376, 1194, 1176, 1170, 1164, 1150, 1149, 1146, 1136, 1133, 1119, 1099, 1073, 1056, 1053, 1046, 1034, 1031, 1028, 1016, 1014, 1012, 1009, 999, 993, 799, 778, 773, 771, 766, 763, 758, 757, 749, 747, 744, 741, 721, 681, 663, 630, 621, 619, 611, 591, 582, 572, 556, 540, 535, 526, 512, 491, 490, 478, 473, 464, 460, 452, 451, 446, 443, 431, 426,

417, 407, 404, 400, 398, 395, 385, 371, 368, 364, 353, 348, 344, 339, 333, 324, 320, 310, 304, 300, 298, 287, 285, 279, 266, 264, 247, 242, 219, 205, 202, 201, 191, 182, 175, 173, 156, 152, 146, 138, 131, 130, 120, 112, 108, 85, 68, 229*i*

- structure **f** ($H_3AlSi_{11}O_{25}$, 117 vibrational modes)

  PBE, 70 Ry:

  3605, 3331, 2151, 1548, 1507, 1178, 1164, 1160, 1156, 1151, 1145, 1142, 1127, 1116, 1104, 1084, 1067, 1047, 1039, 1036, 1030, 1025, 1020, 1019, 1013, 1009, 1008, 996, 982, 871, 782, 766, 763, 760, 756, 754, 750, 745, 744, 740, 706, 689, 664, 657, 637, 612, 609, 597, 591, 568, 550, 530, 520, 512, 486, 473, 467, 463, 462, 457, 449, 446, 438, 432, 412, 407, 405, 402, 397, 395, 384, 379, 377, 370, 361, 350, 347, 338, 330, 327, 319, 316, 309, 306, 305, 300, 298, 287, 284, 278, 274, 266, 262, 253, 240, 234, 221, 193, 190, 182, 179, 174, 166, 161, 156, 149, 140, 137, 134, 128, 121, 115, 107, 101, 81, 67, 42

  PBE, 100 Ry:

  3727, 3464, 2163, 1556, 1505, 1171, 1158, 1153, 1148, 1144, 1139, 1134, 1120, 1110, 1097, 1075, 1061, 1042, 1033, 1029, 1024, 1016, 1015, 1013, 1004, 1002, 999, 989, 984, 860, 783, 768, 764, 761, 757, 753, 749, 745, 743, 739, 703, 685, 661, 647, 631, 611, 607, 595, 586, 563, 549, 527, 519, 510, 481, 474, 469, 461, 459, 456, 449, 446, 436, 426, 412, 406, 404, 403, 398, 397, 385, 383, 375, 368, 358, 353, 344, 339, 331, 328, 325, 318, 312, 308, 306, 300, 297, 292, 289, 279, 274, 274, 261, 253, 243, 235, 217, 195, 191, 185, 179, 172, 165, 158, 154, 147, 145, 142, 135, 129, 125, 121, 117, 106, 100, 92, 82

  MP2/PBE, basis set A:

  3846, 3715, 2448, 1589, 1550, 1194, 1183, 1177, 1174, 1159, 1152, 1150, 1141, 1137, 1114, 1100, 1081, 1073, 1062, 1058, 1050, 1043, 1034, 1033, 1030, 1018, 1014, 1011, 997, 885, 792, 774, 771, 768, 764, 762, 758, 753, 749, 745, 744, 736, 685, 658, 644, 620, 617, 612, 611, 563, 555, 536, 533, 512, 499, 491, 488, 475, 471, 466, 460, 456, 448, 446, 438, 425, 415, 412, 407, 404, 400, 394, 386, 378, 371, 366, 353, 349, 347, 339, 334, 329, 323, 319, 311, 308, 304, 301, 292, 289, 288, 274, 265, 250, 243, 233, 215, 205, 198, 191, 189, 179, 170, 169, 165, 161, 144, 141, 130, 127, 121, 119, 110, 90, 82, 70, 57

A.2 THE SYSTEM FERRIERITE/ISOBUTENE

(see Chapter 4 for details; all numbers in cm^{-1})

- isobutene (C_4H_8, 30 vibrational modes)

  3124, 3039, 3027, 3026, 2975, 2973, 2926, 2921, 1657, 1443, 1430, 1424, 1411, 1386, 1353, 1351, 1259, 1059, 1042, 979, 956, 926, 871, 806, 678, 425, 422, 368, 204, 169

- *tert*-butyl carbenium ion ($C_4H_9^+$, 33 vibrational modes)

  3078, 3075, 3073, 2961, 2954, 2941, 2898, 2881, 2872, 1455, 1452, 1436, 1387, 1360, 1353, 1311, 1304, 1271, 1240, 1237, 1063, 959, 956, 946, 809, 757, 743, 443, 399, 397, 178, 57, 40

- unloaded H-FER **1** ($HAlSi_{71}O_{144}$, 648 vibrational modes)

  3680, 1244, 1226, 1223, 1221, 1219, 1218, 1217, 1216, 1215, 1213, 1212, 1212, 1211, 1210, 1207, 1205, 1204, 1203, 1203, 1202, 1201, 1200, 1200, 1199, 1198, 1197, 1197, 1196, 1195, 1194, 1193, 1192, 1190, 1190, 1188, 1188, 1186, 1185, 1185, 1183, 1181, 1180, 1178, 1177, 1176, 1175, 1173, 1172, 1171, 1170, 1167, 1166, 1166, 1164, 1161, 1160, 1158, 1157, 1156, 1154, 1153, 1152, 1152, 1150, 1149, 1147, 1147, 1145, 1143, 1138, 1136, 1115, 1107, 1093, 1092, 1091, 1090, 1090, 1089, 1088, 1087, 1086, 1086, 1085, 1085, 1084, 1083, 1083, 1081, 1081, 1080, 1079, 1079, 1078, 1077, 1077, 1076, 1075, 1075, 1074, 1074, 1073, 1073, 1072, 1072, 1071, 1070, 1070, 1069, 1068, 1067, 1067, 1065, 1065, 1064, 1064, 1063, 1062, 1062, 1062, 1062, 1061, 1060, 1059, 1059, 1058, 1058, 1058, 1057, 1057, 1056, 1056, 1055, 1055, 1054, 1054, 1054, 1053, 1053, 1051, 1050, 1045, 1041, 1040, 801, 799, 797, 793, 791, 790, 789, 788, 788, 786, 785, 785, 785, 783, 783, 783, 782, 781, 780, 779, 778, 778, 777, 777, 776, 776, 775, 775, 774, 773, 773, 772, 771, 771, 770, 770, 770, 769, 768, 768, 767, 767, 766, 766, 765, 763, 761, 761, 761, 760, 759, 759, 758, 757, 757, 756, 756, 755, 754, 753, 752, 751, 751, 750, 750, 749, 748, 747, 745, 743, 743, 738, 727, 723, 722, 721, 718, 715, 709, 707, 707, 705, 704, 697, 692, 690, 682, 676, 674, 673, 667, 664, 660, 654, 645, 644, 642, 635, 615, 599, 592, 588, 585, 581, 578, 577, 572, 571, 569, 568, 563, 560, 559, 557, 555, 553, 552, 550, 548, 547, 545, 544, 543, 541, 539, 537, 535, 533, 528, 523, 521, 518, 514, 509, 506, 499, 496, 493, 491, 490, 486, 481, 477, 443, 439, 438, 437, 436, 435, 435, 434, 433, 432, 431, 431, 430, 430, 429, 428, 428, 427, 426, 426, 424, 423, 422, 422, 421, 420, 419, 419, 418, 418, 417, 417, 416, 415, 414, 413, 412, 411, 410, 409, 407, 407, 407, 405, 404, 404, 404, 403, 403, 403, 402, 402, 401, 401, 400, 399, 399, 398, 397, 397, 396, 395, 395, 394, 393, 392, 391, 390, 390, 389, 388, 388, 386, 386, 385, 384, 384, 383, 382, 380, 379, 379, 379, 378, 377, 377, 376, 375, 375, 373, 373, 372, 371, 370, 369, 369, 366, 366, 364, 362, 361, 361, 359, 358, 358, 357, 356, 354, 354, 353, 351,

350, 349, 349, 346, 346, 344, 343, 343, 343, 341, 340, 340, 338, 337, 337, 334, 334, 333, 333, 332, 330, 329, 328, 327, 327, 326, 324, 324, 322, 320, 319, 318, 317, 316, 315, 314, 313, 312, 311, 311, 310, 309, 309, 307, 306, 305, 303, 303, 302, 301, 300, 299, 298, 297, 296, 294, 293, 292, 290, 290, 289, 287, 286, 285, 283, 281, 280, 277, 275, 274, 272, 272, 271, 267, 266, 266, 265, 264, 263, 262, 262, 260, 260, 259, 258, 255, 254, 251, 251, 250, 249, 248, 246, 245, 243, 242, 240, 239, 238, 237, 236, 234, 234, 233, 232, 231, 230, 227, 226, 226, 225, 225, 224, 222, 219, 218, 216, 215, 214, 213, 210, 209, 206, 205, 203, 202, 202, 200, 196, 195, 193, 191, 190, 188, 188, 186, 185, 185, 183, 183, 181, 181, 180, 179, 177, 174, 168, 167, 166, 165, 163, 161, 161, 159, 159, 157, 156, 155, 154, 153, 151, 149, 147, 146, 144, 143, 142, 142, 140, 140, 136, 135, 134, 133, 131, 129, 129, 128, 127, 126, 125, 124, 123, 122, 121, 120, 118, 117, 116, 113, 110, 110, 108, 107, 106, 106, 105, 104, 102, 101, 100, 97, 97, 96, 93, 92, 91, 89, 89, 87, 86, 85, 81, 80, 78, 76, 73, 72, 71, 70, 69, 67, 63, 62, 62, 61, 60, 60, 58, 55, 55, 53, 52, 51, 50, 49, 48, 48, 47, 46, 44, 43, 42, 41, 41, 38, 37, 32, 28

- π-complex **2** ($C_4H_{13}AlSi_{71}O_{144}$, 684 vibrational modes)

  3125, 3053, 3044, 3032, 3001, 2996, 2945, 2939, 2837, 1623, 1445, 1435, 1421, 1412, 1378, 1356, 1355, 1272, 1243, 1227, 1225, 1222, 1221, 1220, 1219, 1218, 1217, 1216, 1214, 1213, 1212, 1209, 1208, 1207, 1206, 1205, 1204, 1202, 1202, 1201, 1200, 1199, 1197, 1197, 1196, 1195, 1194, 1194, 1191, 1191, 1190, 1188, 1186, 1185, 1184, 1184, 1183, 1182, 1181, 1179, 1178, 1176, 1175, 1174, 1172, 1171, 1171, 1169, 1168, 1167, 1166, 1164, 1163, 1161, 1159, 1157, 1156, 1156, 1154, 1153, 1152, 1151, 1149, 1148, 1147, 1145, 1144, 1141, 1139, 1131, 1109, 1095, 1094, 1093, 1093, 1091, 1091, 1090, 1089, 1089, 1088, 1086, 1084, 1083, 1082, 1081, 1081, 1081, 1080, 1079, 1079, 1078, 1077, 1077, 1076, 1075, 1074, 1074, 1073, 1073, 1072, 1072, 1072, 1071, 1070, 1069, 1069, 1068, 1068, 1067, 1066, 1065, 1063, 1062, 1062, 1061, 1061, 1060, 1060, 1060, 1060, 1059, 1059, 1058, 1058, 1057, 1056, 1056, 1056, 1056, 1055, 1054, 1054, 1054, 1053, 1051, 1051, 1050, 1049, 1049, 1048, 1048, 1047, 1035, 982, 954, 929, 894, 830, 815, 801, 797, 793, 791, 790, 789, 787, 787, 787, 786, 785, 785, 783, 783, 782, 781, 780, 780, 778, 778, 778, 777, 776, 776, 775, 775, 774, 774, 773, 773, 772, 772, 772, 770, 769, 769, 769, 768, 768, 767, 767, 766, 765, 764, 763, 763, 762, 761, 761, 759, 759, 759, 758, 756, 756, 756, 755, 754, 753, 753, 752, 752, 751, 751, 750, 749, 748, 746, 744, 743, 740, 736, 727, 723, 722, 721, 716, 714, 708, 707, 707, 706, 702, 697, 692, 691, 687, 681, 675, 672, 672, 667, 664, 659, 654, 646, 643, 643, 635, 615, 601, 592, 587, 585, 582, 578, 577, 572, 570, 569, 566, 563, 559, 558, 557, 555, 553, 551, 549, 548, 547, 545, 544, 542, 541, 539, 537, 535, 533, 530, 523, 521, 520, 515, 513, 506, 499, 496, 492, 491, 490, 486, 481, 478, 456, 444, 439, 438, 436, 436, 435, 434, 434, 434, 433, 432, 432, 430, 430, 429, 429, 427, 427, 425, 424, 424, 423, 423, 422, 422, 420, 420, 420, 418, 418, 417, 417, 416, 415, 415, 414, 413, 412, 412, 410, 409, 409, 408, 407, 407, 406, 405, 404, 404, 403, 403, 403, 402, 401, 401, 399, 399, 398, 398, 397,

397, 396, 396, 395, 394, 393, 392, 392, 390, 389, 388, 388, 387, 387, 386, 385, 384, 384, 382, 382, 381, 381, 379, 379, 378, 378, 377, 376, 376, 375, 375, 374, 372, 372, 372, 370, 370, 369, 368, 367, 364, 363, 362, 361, 359, 359, 358, 358, 356, 355, 353, 353, 351, 350, 350, 349, 348, 347, 345, 344, 343, 342, 341, 340, 339, 338, 337, 336, 335, 333, 332, 331, 330, 329, 329, 327, 326, 326, 325, 324, 324, 322, 320, 319, 318, 316, 315, 315, 314, 313, 312, 311, 310, 309, 309, 307, 307, 305, 305, 304, 303, 302, 301, 299, 298, 297, 296, 296, 295, 294, 292, 290, 289, 289, 287, 285, 283, 283, 281, 279, 277, 276, 274, 273, 271, 270, 269, 267, 266, 265, 264, 263, 262, 261, 261, 259, 257, 256, 255, 254, 253, 252, 250, 249, 247, 245, 244, 243, 241, 241, 239, 237, 237, 235, 234, 233, 232, 231, 230, 230, 229, 227, 227, 226, 225, 223, 222, 220, 218, 217, 215, 214, 213, 211, 209, 207, 204, 204, 202, 201, 197, 196, 195, 194, 192, 191, 190, 189, 188, 187, 186, 185, 185, 184, 183, 182, 181, 180, 177, 175, 171, 168, 166, 165, 165, 162, 161, 160, 160, 158, 157, 157, 154, 154, 153, 151, 149, 148, 145, 144, 143, 142, 142, 141, 138, 137, 136, 136, 134, 134, 131, 130, 128, 127, 126, 126, 124, 124, 121, 120, 119, 117, 117, 115, 114, 112, 110, 108, 108, 106, 104, 104, 103, 103, 101, 100, 99, 98, 97, 96, 96, 94, 92, 92, 91, 89, 89, 87, 85, 84, 83, 82, 79, 78, 77, 75, 72, 72, 70, 69, 67, 66, 65, 63, 62, 61, 60, 59, 56, 55, 55, 55, 53, 52, 51, 50, 49, 48, 46, 46, 44, 43, 42, 39, 38, 36, 33, 30, 28

- *tert*-butoxide **3** ($C_4H_{13}AlSi_{71}O_{144}$, 684 vibrational modes)

3099, 3096, 3094, 3048, 3043, 3033, 2979, 2971, 2966, 1472, 1456, 1445, 1436, 1429, 1413, 1380, 1356, 1352, 1247, 1242, 1236, 1228, 1227, 1225, 1224, 1222, 1220, 1217, 1217, 1216, 1214, 1212, 1211, 1208, 1207, 1206, 1205, 1204, 1202, 1202, 1200, 1198, 1197, 1197, 1195, 1194, 1193, 1191, 1190, 1189, 1188, 1186, 1185, 1184, 1183, 1183, 1182, 1181, 1180, 1179, 1178, 1176, 1175, 1174, 1173, 1172, 1171, 1170, 1169, 1168, 1167, 1165, 1163, 1163, 1161, 1159, 1159, 1157, 1156, 1154, 1153, 1152, 1150, 1148, 1147, 1147, 1144, 1141, 1141, 1140, 1130, 1108, 1102, 1094, 1093, 1092, 1091, 1089, 1089, 1088, 1087, 1086, 1085, 1083, 1081, 1080, 1080, 1080, 1079, 1079, 1078, 1077, 1077, 1076, 1076, 1075, 1075, 1074, 1074, 1073, 1072, 1071, 1071, 1071, 1070, 1069, 1069, 1068, 1068, 1067, 1067, 1066, 1066, 1064, 1063, 1063, 1062, 1061, 1060, 1060, 1059, 1058, 1058, 1057, 1057, 1056, 1055, 1055, 1054, 1054, 1052, 1052, 1051, 1050, 1049, 1048, 1048, 1047, 1047, 1046, 1045, 1045, 1039, 1034, 1020, 1014, 936, 909, 890, 831, 801, 797, 792, 791, 790, 789, 788, 787, 786, 785, 785, 784, 783, 782, 781, 781, 779, 779, 778, 778, 777, 776, 775, 775, 774, 773, 773, 773, 773, 772, 772, 771, 771, 770, 769, 769, 768, 767, 767, 766, 766, 765, 764, 764, 763, 762, 762, 761, 760, 759, 759, 759, 758, 757, 756, 755, 754, 754, 753, 752, 752, 751, 751, 750, 749, 748, 747, 746, 742, 741, 738, 729, 727, 723, 723, 720, 717, 714, 707, 706, 706, 703, 698, 697, 691, 689, 678, 674, 673, 669, 669, 663, 660, 655, 647, 645, 642, 632, 616, 602, 593, 589, 585, 584, 579, 578, 573, 569, 568, 566, 562, 560, 560, 559, 557, 555, 552, 552, 550, 547, 546, 545, 541, 540, 539, 538, 536, 535, 530, 527, 525, 522, 519, 513, 510, 505, 497, 494, 492, 490, 488, 484, 480, 479, 455, 446, 442,

438, 438, 437, 436, 435, 434, 434, 434, 433, 432, 431, 430, 429, 428, 426, 426, 425, 425, 424, 423, 422, 421, 421, 420, 420, 419, 419, 418, 417, 417, 417, 416, 415, 414, 413, 412, 412, 410, 410, 409, 408, 408, 407, 406, 406, 404, 404, 403, 403, 402, 401, 401, 400, 400, 398, 398, 398, 397, 396, 396, 396, 395, 394, 393, 393, 393, 391, 391, 390, 389, 389, 388, 388, 387, 385, 384, 384, 383, 382, 381, 380, 379, 379, 379, 378, 377, 376, 375, 375, 374, 374, 374, 371, 370, 369, 369, 367, 367, 366, 365, 363, 362, 361, 360, 359, 359, 357, 356, 355, 354, 352, 352, 351, 349, 349, 347, 347, 345, 342, 341, 340, 339, 338, 337, 336, 335, 334, 334, 333, 332, 331, 330, 329, 328, 328, 326, 326, 325, 325, 324, 322, 321, 321, 320, 319, 317, 316, 314, 312, 312, 311, 310, 309, 307, 307, 306, 305, 304, 302, 302, 301, 300, 300, 299, 297, 296, 296, 293, 292, 292, 291, 289, 288, 287, 285, 285, 283, 282, 282, 280, 279, 277, 275, 273, 272, 270, 269, 269, 267, 266, 265, 265, 262, 261, 260, 260, 259, 258, 256, 255, 253, 253, 251, 250, 248, 248, 246, 244, 243, 242, 241, 238, 237, 236, 234, 234, 233, 232, 230, 230, 229, 228, 228, 226, 224, 222, 221, 218, 218, 215, 215, 214, 212, 210, 209, 205, 205, 204, 203, 202, 200, 200, 198, 197, 196, 195, 193, 191, 190, 189, 188, 187, 187, 186, 185, 182, 181, 180, 178, 176, 175, 172, 171, 169, 167, 165, 165, 162, 162, 161, 157, 157, 155, 154, 154, 152, 151, 151, 150, 148, 145, 144, 143, 142, 141, 138, 138, 137, 135, 135, 134, 133, 130, 130, 128, 128, 126, 124, 124, 122, 122, 119, 119, 117, 115, 113, 112, 111, 110, 108, 106, 105, 104, 103, 102, 102, 101, 100, 99, 97, 95, 94, 90, 90, 89, 89, 85, 85, 83, 81, 80, 79, 77, 76, 75, 74, 73, 72, 71, 69, 67, 65, 64, 64, 62, 61, 60, 59, 58, 57, 56, 55, 54, 53, 52, 52, 49, 49, 48, 47, 46, 44, 41, 39, 37, 31, 29

- *tert*-butyl carbenium ion **4** ($C_4H_{13}AlSi_{71}O_{144}$, 684 vibrational modes)

  3078, 3069, 3067, 2994, 2976, 2932, 2890, 2862, 2402, 1482, 1449, 1441, 1387, 1371, 1337, 1327, 1299, 1296, 1277, 1245, 1230, 1229, 1226, 1222, 1220, 1219, 1218, 1216, 1215, 1213, 1211, 1210, 1210, 1207, 1205, 1205, 1203, 1203, 1202, 1202, 1200, 1199, 1198, 1198, 1197, 1195, 1194, 1194, 1193, 1192, 1189, 1188, 1186, 1185, 1184, 1183, 1183, 1182, 1181, 1179, 1178, 1176, 1175, 1174, 1172, 1171, 1170, 1169, 1167, 1166, 1165, 1164, 1163, 1162, 1159, 1158, 1156, 1155, 1154, 1153, 1152, 1150, 1148, 1147, 1147, 1145, 1143, 1142, 1140, 1136, 1135, 1115, 1106, 1097, 1093, 1091, 1091, 1090, 1090, 1089, 1087, 1086, 1086, 1083, 1083, 1082, 1081, 1081, 1080, 1080, 1079, 1078, 1078, 1077, 1076, 1074, 1074, 1073, 1073, 1072, 1071, 1071, 1071, 1070, 1070, 1070, 1069, 1067, 1066, 1066, 1064, 1063, 1062, 1062, 1061, 1061, 1061, 1060, 1060, 1059, 1059, 1058, 1058, 1057, 1057, 1056, 1056, 1055, 1055, 1054, 1054, 1054, 1053, 1051, 1051, 1050, 1049, 1047, 1046, 1045, 1039, 1036, 1035, 1033, 1017, 1000, 960, 953, 844, 802, 799, 795, 792, 790, 789, 787, 786, 786, 785, 785, 784, 783, 782, 782, 781, 780, 780, 778, 777, 777, 776, 776, 775, 775, 774, 773, 772, 772, 771, 771, 771, 770, 770, 769, 768, 768, 767, 767, 766, 766, 765, 763, 763, 761, 761, 760, 760, 759, 759, 758, 757, 756, 756, 755, 754, 753, 752, 752, 751, 750, 749, 749, 748, 748, 747, 745, 745, 743, 740, 738, 734, 729, 725, 722, 721, 720, 714, 711, 708, 706, 705, 700, 698, 694, 690, 688, 682, 675, 672, 671,

669, 663, 657, 653, 647, 645, 641, 633, 631, 613, 592, 586, 586, 583, 577, 576, 572, 570, 569, 567, 565, 559, 559, 557, 555, 554, 551, 550, 548, 547, 546, 544, 543, 541, 538, 538, 535, 534, 532, 523, 521, 520, 516, 514, 506, 499, 496, 491, 489, 489, 486, 480, 478, 461, 443, 438, 437, 436, 435, 435, 434, 433, 433, 432, 432, 430, 429, 429, 428, 427, 427, 426, 425, 425, 423, 423, 422, 421, 421, 420, 420, 419, 418, 417, 416, 416, 415, 414, 413, 413, 412, 411, 410, 410, 408, 408, 407, 406, 405, 404, 404, 404, 403, 403, 402, 402, 401, 401, 400, 399, 399, 399, 398, 397, 397, 396, 395, 395, 394, 393, 392, 392, 391, 390, 390, 388, 388, 387, 387, 385, 385, 384, 383, 383, 382, 381, 379, 378, 378, 377, 377, 376, 376, 375, 375, 374, 373, 372, 371, 370, 369, 369, 368, 368, 366, 362, 362, 360, 360, 359, 358, 357, 356, 355, 354, 353, 352, 351, 349, 349, 348, 346, 345, 344, 344, 342, 341, 341, 340, 339, 338, 336, 336, 332, 332, 331, 330, 329, 328, 327, 327, 326, 325, 324, 323, 322, 322, 319, 318, 316, 315, 314, 313, 312, 312, 310, 310, 309, 308, 307, 306, 305, 304, 303, 303, 302, 300, 300, 298, 297, 296, 294, 294, 294, 293, 290, 289, 288, 288, 286, 284, 283, 282, 281, 279, 274, 274, 273, 271, 270, 268, 266, 265, 265, 264, 263, 262, 261, 260, 259, 258, 257, 255, 254, 252, 251, 251, 250, 248, 245, 244, 243, 241, 240, 239, 238, 237, 235, 234, 234, 232, 231, 230, 229, 227, 225, 225, 225, 224, 223, 220, 218, 217, 215, 214, 213, 211, 209, 207, 207, 202, 201, 200, 200, 195, 194, 193, 191, 190, 189, 188, 187, 186, 185, 185, 183, 183, 181, 180, 180, 179, 178, 175, 172, 166, 163, 163, 162, 161, 160, 158, 157, 156, 155, 155, 153, 152, 151, 151, 149, 146, 145, 142, 141, 140, 139, 139, 138, 135, 135, 132, 132, 131, 130, 128, 128, 124, 124, 123, 122, 121, 119, 118, 116, 116, 115, 114, 114, 111, 110, 107, 106, 104, 104, 103, 101, 99, 98, 97, 97, 95, 95, 92, 92, 91, 90, 88, 88, 86, 85, 83, 83, 80, 77, 76, 72, 72, 71, 69, 68, 67, 65, 64, 63, 59, 58, 56, 56, 54, 53, 51, 50, 49, 47, 46, 45, 44, 43, 42, 40, 39, 39, 37, 35, 35, 34, 32, 31, 30, 28, 25, 20, 15, 7

- isobutoxide **5** ($C_4H_{13}AlSi_{71}O_{144}$, 684 vibrational modes)

  3057, 3047, 3044, 3030, 3013, 2993, 2971, 2961, 2941, 1463, 1452, 1446, 1437, 1432, 1383, 1358, 1349, 1336, 1286, 1273, 1244, 1226, 1223, 1219, 1219, 1218, 1217, 1216, 1215, 1214, 1213, 1210, 1209, 1209, 1207, 1206, 1205, 1203, 1202, 1201, 1200, 1200, 1199, 1198, 1197, 1196, 1196, 1194, 1191, 1191, 1190, 1189, 1188, 1187, 1186, 1185, 1184, 1183, 1181, 1180, 1180, 1178, 1178, 1178, 1176, 1175, 1172, 1171, 1170, 1168, 1167, 1166, 1165, 1164, 1162, 1161, 1159, 1157, 1156, 1155, 1155, 1152, 1151, 1150, 1149, 1149, 1147, 1146, 1144, 1142, 1141, 1138, 1122, 1108, 1098, 1094, 1093, 1092, 1091, 1090, 1089, 1088, 1088, 1087, 1087, 1086, 1085, 1084, 1082, 1082, 1081, 1081, 1081, 1078, 1078, 1078, 1077, 1077, 1075, 1074, 1074, 1073, 1073, 1073, 1072, 1072, 1071, 1070, 1069, 1069, 1069, 1068, 1068, 1066, 1065, 1064, 1063, 1063, 1062, 1061, 1061, 1060, 1060, 1059, 1059, 1059, 1057, 1057, 1056, 1056, 1055, 1055, 1054, 1054, 1054, 1053, 1053, 1052, 1051, 1051, 1050, 1049, 1047, 1046, 1043, 1038, 950, 937, 910, 896, 853, 803, 799, 796, 796, 793, 791, 790, 789, 788, 787, 787, 786, 785, 784, 784, 782, 781, 781, 780, 779, 779, 778, 777, 777, 776, 775, 775, 774, 774, 773, 773, 772,

772, 771, 771, 770, 769, 768, 768, 768, 767, 767, 766, 765, 764, 763, 763, 762, 761, 760, 760, 759, 759, 758, 757, 756, 755, 754, 754, 753, 752, 751, 750, 750, 750, 749, 748, 747, 747, 744, 742, 738, 735, 727, 723, 721, 721, 716, 713, 708, 706, 706, 703, 701, 696, 692, 689, 681, 674, 673, 672, 666, 663, 659, 653, 647, 645, 640, 634, 615, 599, 592, 587, 585, 582, 577, 575, 571, 570, 569, 565, 562, 560, 558, 558, 554, 553, 551, 550, 548, 547, 546, 544, 541, 540, 539, 536, 534, 531, 526, 524, 521, 519, 516, 509, 506, 499, 495, 493, 490, 488, 485, 481, 477, 466, 442, 438, 437, 436, 435, 434, 433, 433, 432, 431, 431, 431, 430, 429, 429, 427, 425, 424, 424, 424, 423, 422, 421, 421, 420, 419, 418, 418, 417, 417, 416, 415, 414, 413, 413, 412, 412, 411, 410, 409, 409, 408, 406, 406, 405, 404, 404, 403, 402, 402, 402, 401, 400, 400, 400, 398, 398, 397, 397, 397, 396, 395, 395, 394, 393, 393, 391, 390, 389, 389, 387, 387, 386, 385, 384, 383, 383, 382, 381, 381, 380, 378, 377, 377, 377, 376, 375, 375, 375, 374, 373, 371, 370, 370, 369, 368, 368, 367, 365, 363, 361, 360, 360, 359, 357, 357, 357, 356, 354, 354, 352, 351, 350, 348, 347, 346, 345, 344, 343, 342, 341, 340, 339, 339, 337, 336, 336, 333, 332, 331, 331, 330, 329, 328, 327, 325, 325, 325, 324, 322, 322, 319, 318, 317, 316, 314, 314, 313, 312, 311, 310, 309, 308, 307, 307, 306, 304, 303, 302, 302, 300, 299, 298, 296, 296, 296, 295, 294, 293, 290, 289, 288, 287, 286, 284, 284, 282, 281, 280, 278, 276, 273, 273, 272, 271, 270, 269, 266, 265, 265, 262, 261, 261, 259, 259, 258, 257, 257, 256, 254, 251, 251, 249, 248, 247, 246, 245, 243, 241, 239, 239, 238, 238, 237, 234, 233, 232, 231, 230, 229, 227, 227, 226, 225, 224, 223, 221, 219, 217, 216, 215, 214, 213, 212, 210, 207, 206, 203, 201, 201, 199, 198, 195, 195, 192, 191, 189, 188, 187, 186, 185, 184, 183, 182, 180, 180, 179, 178, 177, 176, 173, 168, 165, 163, 161, 161, 159, 158, 157, 156, 155, 154, 154, 153, 152, 149, 148, 147, 145, 143, 141, 141, 139, 139, 138, 135, 134, 133, 132, 131, 129, 127, 125, 124, 122, 122, 121, 120, 119, 118, 117, 116, 115, 114, 112, 110, 108, 107, 104, 103, 102, 102, 101, 99, 97, 97, 95, 94, 93, 92, 92, 90, 89, 87, 85, 84, 83, 82, 81, 81, 77, 75, 73, 71, 71, 69, 68, 67, 63, 62, 58, 56, 54, 54, 52, 51, 49, 48, 47, 46, 46, 44, 43, 41, 40, 39, 37, 36, 34, 34, 32, 30, 29, 28, 22, 19, 14, 9

Appendix B

FURTHER NUMERICAL DATA

Table B.1: *Link atom bond distances (in pm) for all types of cluster model termination used in this work*

link atom bond	T-atom	bond distance	*comment (footnote)*
H – OT	Al	95.3	*a*
	Si	95.4	*a*
H – T	Al	—	*b*
	Si	145.5	*c*

[a] average value of relaxed TO – H bond distances (employing MP2(ae) and a T(O)DZP basis set described in footnote 18 on page 34) obtained with the 2T cluster model in Fig. 2.11 (without water) having a fixed zeolite framework atom structure (taken from fully relaxed H-SSZ-13 [164])

[b] the $Al[O_{1/2}]_4$ tetrahedron is kept complete in cluster models used for embedding

[c] obtained for $(HO)_3Si-H$ optimised in C_{3v} symmetry (employing MP2(fc) and the TZVPP basis set)

Table B.2: *Core radii r_c (in a_0) of the pseudopotential angular momentum channels. Pseudopotentials of Troullier–Martins (TM) [140], Bachelet–Hamann–Schlüter (BHS) [139], or Vanderbilt (Vdb) [142] type are employed in this work*

atom	l	TM [a]	BHS	Vdb [b]
hydrogen	s	0.70		0.80
carbon	s	1.10		1.10
	p	1.10		1.10
oxygen	s	1.15		1.10
	p	1.15		1.10
aluminium	s	1.60	1.60	1.70 [d]
	p	1.60	1.60	1.70 [d]
	d	1.60 [c]	1.20	1.80 [d]
silicon	s	1.40	1.40	1.60 [f]
	p	1.40	1.40	1.60 [f]
	d	1.40 [e]	1.00	1.60 [f]

[a] pseudopotentials generated by F. Haase, Humboldt-Universität zu Berlin
[b] parameters provided by B. Meyer, Ruhr-Universität Bochum
[c] potential generated in [Ne]$3s^1 3p^{0.75} 3d^{0.25}$ configuration
[d] potential generated in [Ne]$3s^2 3p^{0.5}$ configuration (not used for production work)
[e] potential generated in [Ne]$3s^2 3p^{0.75} 3d^{0.25}$ configuration
[f] potential generated in [Ne]$3s^2 3p^{1.5}$ configuration (not used for production work)

Table B.3: *Selected vibrational frequencies (in cm^{-1}) of the methanol molecule calculated[a] with DFT (PBE functional) and Gaussian basis sets*

basis set	ν(O – H)	ν(C – H)	ν(C – O)
TZVP [b]	3724	3055, 2968, 2926	1021
TZVPP [c]	3741	3054, 2976, 2925	1023
QZVP [d]	3740	3049, 2973, 2925	1023
aug-TZVPP [c,e]	3737	3053, 2985, 2938	1018
aug-QZVP [d,e]	3738	3050, 2969, 2922	1018

[a] structures fully relaxed (grid "m4", Cartesian gradient norm below $1 * 10^{-4}\ E_h/a_0$); $\pm 0.01\ a_0$ atom displacements for numerical differentiation of forces, translational and rotational modes projected from the Hessian matrix (TURBOMOLE)

[b] ref. [156], polarisation functions with exponents 0.8 (C), 0.8 (H), and 1.2 (O)

[c] ref. [156], polarisation functions taken from cc-pVTZ basis sets [155]

[d] ref. [157]

[e] diffuse basis functions taken from corresponding aug-cc-pV*X*Z basis sets [158]

Table B.4: *Single-point RI-MP2(fc) calculations for the 2T zeolite cluster model water binding energy using Ahlrichs' basis sets. Uncorrected and counterpoise corrected results, ΔE and ΔE^{cp}, and corresponding MP2-only values, ΔE_{MP2} and ΔE^{cp}_{MP2}, are given (in kJ/mol)*

H, Al, Si	O	N [a]	ΔE	ΔE^{cp}	ΔE_{MP2}	ΔE^{cp}_{MP2}
TZVP [b]	TZVP [b]	250	68.46	54.41	16.41	6.62
	TZVPP [c]	346	68.15	57.73	19.14	12.27
	QZVP [d]	554	65.44	59.49	19.21	15.16
	aug-TZVP [b,e]	378	65.39	57.03	19.88	12.62
	aug-TZVPP [c,e]	474	64.48	59.22	19.28	15.24
	aug-QZVP [d,e]	754	64.68	61.26	19.70	17.07
TZVPP [c]	TZVPP	448	68.26	58.50	20.64	13.82
	QZVP	656	65.17	60.53	19.52	16.03
	aug-TZVPP	576	64.38	59.94	19.48	15.66
	aug-QZVP	856	64.26	61.63	19.53	17.23
QZVP [d]	QZVP	866	65.40	61.09	20.23	16.70
	aug-QZVP	1066	64.19	61.81	19.76	17.48

[a] total number of contracted spherical basis functions for the adsorption complex
[b] ref. [156], polarisation functions with exponents 0.8 (H), 0.3 (Al), 0.35 (Si), and 1.2 (O)
[c] ref. [156], polarisation functions taken from cc-pVTZ basis sets [155]
[d] ref. [157]
[e] diffuse basis functions taken from corresponding aug-cc-pVXZ basis sets [158]

Table B.5: *H-FER free cluster model DFT (PBE functional) reaction energies*[a] *for the formation of structures* ***2*** *–* ***5*** *(all numbers in kJ/mol)*

	structure			
T-atoms[b]	**2**[c]	**3**	**4**	**5**
2	−14.5 (−14.4)	11.5	103.2	−16.2
3	−8.9 (−9.0)	23.5	102.4	−8.5
4	−14.9 (−14.9)	−7.7	65.3	−21.0
5	−25.1 (−25.2)	−47.1	46.2	−35.1
6	−27.2 (−27.3)	−53.3	10.3	−40.6
7	−37.5 (−37.8)	−61.0	2.8	−47.3
8	−33.3 (−33.6)	−74.5	−16.6	−47.5
9	−33.8 (−34.1)	−86.9	−29.7	−43.9
10	−44.6 (−45.0)	−92.2	−73.5	−58.6
13	−24.3 (−24.0)	−64.7	−43.0	−30.7
16	−19.1 (−18.7)	−62.5	−20.4	−22.9
18	−11.5 (−11.1)	−22.6	43.7	−7.6
20	−17.0 (−16.7)	8.9	48.9	−11.1
22	−15.5 (−15.2)	−22.3	−12.0	−6.9
25	3.4 (3.7)	14.5	16.6	22.1
28	32.3 (32.4)	43.2	25.3	53.8
29	34.9 (35.0)	37.9	20.2	62.7

[a] plane wave basis set (30 Ry kinetic energy cut-off), BHS and Vdb type pseudopotentials

[b] number of T-atoms in the cluster model, *cf.* Fig. 4.4 on page 66

[c] Numbers in parentheses are from TURBOMOLE RI-DFT calculations employing the QZVP basis set [157]. They are not corrected for the BSSE which is expected to be negligible with this basis set. These values demonstrate high numerical reliability of the plane wave basis set results.

Table B.6: *H-FER free cluster model RI-MP2(fc)/TZVP (aug(O)-TZVPP) reaction energies for the formation of structures* ***2*** *–* ***5*** *(all numbers in kJ/mol)*

	structure			
T-atoms [a]	**2**	**3**	**4**	**5**
2	−23.6 (−26.3)	−23.1 (−25.1)	160.0 (146.3)	−50.0 (−47.5)
3	−21.2 (−25.1)	−14.6 (−18.3)	152.6 (139.3)	−47.5 (−46.4)
4	−30.1 (−35.2)	−51.4 (−54.8)	109.8 (97.5)	−66.1 (−65.4)
5	−49.5 (−52.9)	−102.2 (−101.9)	80.4 (71.0)	−87.9 (−85.0)
6	−56.1 (−60.0)	−112.4 (−111.1)	33.7 (27.8)	−97.0 (−93.8)
7	−70.8 (−74.8)	−125.1 (−123.6)	21.3 (15.5)	−108.2 (−104.7)
8	−69.3 (−74.7)	−143.7 (−141.6)	−5.2 (−10.0)	−110.1 (−106.7)
9	−73.0 (−78.7)	−161.0 (−159.2)	−23.0 (−28.1)	−107.1 (−105.3)
10	−89.0 (−94.5)	−169.6 (−168.2)	−78.9 (−80.7)	−127.2 (−124.8)
13	−74.5 (−81.1)	−146.9 (−145.7)	−58.8 (−60.2)	−101.1 (−100.5)
16	−77.3 (−82.7)	−148.4 (−146.6)	−42.4 (−44.4)	−97.0 (−95.9)
18	−73.4 (−79.2)	−109.4 (−108.1)	21.3 (16.6)	−84.4 (−84.5)
20	−82.6 (−87.2)	−81.5 (−78.7)	23.3 (19.6)	−90.4 (−89.3)
22	−82.0 (−86.1)	−111.7 (−108.7)	−38.0 (−40.8)	−85.7 (−84.6)
25	−65.9 (−70.6)	−76.7 (−78.2)	−13.9 (−18.2)	−67.2 (−66.6)
28	−39.3	−47.3	−6.6	−39.6
29	−38.0	−56.1	−14.1	−32.3

[a] number of T-atoms in the cluster model, *cf.* Fig. 4.4 on page 66

Table B.7: *Sets of parameters C_6 (in nm^6Jmol^{-1}) for C, H_a, O, and H_z atoms as well as additive constants, E_{add}, fitted to reproduce differences between cluster model reaction energies obtained with MP2/TZVP (aug(O)-TZVPP) and plane wave DFT*

	C_6				
structure	C	H_a	O	H_z	E_{add}
2	88.8298	−0.14071	2.65186	−2.07543	−9.75561
	(20.2749	0.72182	0.88655	−0.24531	−8.18019)
3	−1.18961	1.03438	19.1003	−0.15988	−6.12368
	(1.10804	0.27246	3.09719	−0.19587	−35.5511)
4	2.37034	0.42948	6.69415	−0.09658	82.2181
	(2.29528	0.26973	7.88467	−1.26700	59.7517)
5	1.90801	1.45225	0.70989	−0.22511	−15.4637
	(7.17935	0.66008	0.92385	−0.25628	−17.0187)

Selbständigkeitserklärung

Hiermit erkläre ich, die vorliegende Arbeit selbständig verfasst und nur die aufgeführte Literatur sowie die angegebenen Hilfsmittel verwendet zu haben.

Christian Tuma

06. September 2006

Danksagung

An erster Stelle danke ich Herrn Prof. Dr. Joachim Sauer für die Themenstellung und die Betreuung meiner Promotionsarbeit. Die vertrauensvolle und ungezwungene Atmosphäre in seiner Arbeitsgruppe habe ich zu schätzen gelernt. Daran haben auch alle ehemaligen und gegenwärtigen Gruppenmitglieder, die mir mit Hilfe, technischer Unterstützung und Diskussionsbereitschaft zur Seite standen, ihren großen Anteil.

Für Rechenzeit auf ihren Systemen danke ich dem Norddeutschen Verbund für Hoch- und Höchstleistungsrechnen sowie dem Konrad-Zuse-Zentrum Berlin. Deren Mitarbeiter haben außerdem wertvolle technische Hilfestellung gegeben.

Der Deutschen Forschungsgemeinschaft danke ich für die finanzielle Unterstützung im Rahmen des Schwerpunktprogrammes 1155 „Molekulare Modellierung und Simulation in der Verfahrenstechnik“.

Ohne die Zusammenarbeit mit Prof. Dr. Christof Hättig, der mir die MPI-Version des TURBOMOLE ricc2-Moduls schon früh zur Verfügung gestellt hat, wären viele RI-MP2 Rechnungen in dieser Arbeit kaum durchführbar gewesen.

Den Gutachtern danke ich für ihre Bereitschaft, die Dissertationsschrift zu bewerten.

Ganz besonderen Dank schulde ich Carolin, die unendlich viel Geduld für mich und diese Arbeit bewiesen hat.